ISOLATING THE ROLE OF GEOMETRICAL STRUCTURE ON

THE MECHANICAL PROPERTIES OF NANOPOROUS METALS

A Dissertation
Presented to
The Academic Faculty

by

Timothy Ibru

In Partial Fulfillment
of the Requirements for the Degree
Doctor of Philosophy in Mechanical Engineering in the
George W. Woodruff School of Mechanical Engineering

Georgia Institute of Technology
August 2020

ISOLATING THE ROLE OF GEOMETRICAL STRUCTURE ON

THE MECHANICAL PROPERTIES OF NANOPOROUS METALS

Approved by:

Dr. Antonia Antoniou, Advisor
School of Mechanical Engineering
Georgia Institute of Technology

Dr. Chloé Arson
School of Civil and Environmental
Engineering
Georgia Institute of Technology

Dr. David McDowell
School of Mechanical Engineering
Georgia Institute of Technology

Dr. Olivier Pierron
School of Mechanical Engineering
Georgia Institute of Technology

Dr. Ting Zhu
School of Mechanical Engineering
Georgia Institute of Technology

Date Approved: July 13, 2020

In honor of my father, who inspired me in more ways than he ever realized

ACKNOWLEDGEMENTS

TABLE OF CONTENTS

LIST OF TABLES

LIST OF FIGURES

LIST OF SYMBOLS AND ABBREVIATIONS

A Projected area in indentation studies

C Fitting constant for scaling relationships

E_f Modulus of porous structure

E_r Reduced modulus calculated during indentation

E_s Modulus of fully dense structure for normalization

FEA   Abbreviation for finite element analysis

FIB   Abbreviation for focused ion beam device

FCC   Abbreviation for face-centered cubic atomic lattice arrangement

G-A   Abbreviation for scaling relationship derived by Gibson and Ashby

GB   Abbreviation for grain boundaries

H   Hardness from indentation experiments

j Symbol denoting junction size

l Symbol denoting ligament length

MD   Abbreviation for molecular dynamics simulations

MD-B   Denoted label for structures generated using MD simulations

n Fitting exponent for scaling relations

NC   Abbreviation for nanocrystalline

P_{max} Maximum applied force during indentation

RF   Denoted label for random lattice structures

SC   Abbreviation for single crystalline

SEM   Abbreviation for scanning electron microscope

t Symbol denoting ligament thickness

TEM	Abbreviation for transmission electron microscope
ε_n	Normal strain along ligaments
ε_{p1}	First principal strain
ε_{p2}	Second principal strain
ε_{xx}	Strain in x-x direction
ε_{xy}	Strain in x-y direction
ε_{yy}	Strain in y-y direction
ρ_f	Density of porous structure
ρ_s	Density of fully dense structure
ρ^*	Relative density ratio of porous structure density to fully dense
$\sigma_{y,f}$	Yield stress of porous structure
$\sigma_{y,s}$	Yield stress of fully dense structure
ν	Poisson ratio
ν^P	Plastic Poisson ratio

SUMMARY

Nanoporous (NP) metals are three-dimensional (3D) structures with characteristic length-scale of its constituents (ligaments, junctions, and pores) in the range from a few to hundreds of nanometers. Such materials are of great interest for many applications, including catalysis, biological material analogues, and the next generation interconnect materials in electronics packaging. Investigations targeting understanding of the mechanical properties of such materials have tried to separate effects of the geometrical arrangement of the 3D network from those due to the nanostructure (abundance of surfaces, presence of grains, and other defects). Traditionally, this has been achieved by assuming that the network is geometrically similar to that of a macroscopic, low-density metal foam.

The goal of this work is to attack the problem using a comprehensive approach that involves isolating the prominent geometry and size scale effects and examining their specific contributions individually for a range of relative densities. Specifically, 3D printed models printed and tested in compression at the macroscale replicate the geometrical arrangement of the nanoporous 3D network independently of any size effects. The relative modulus and relative compressive yield strength for the 3D printed structures with same arrangement as the nanoporous solid exhibit different scalings with density compared to stochastic macroscale foams. The deformation mechanism in stochastic macroscale foams is isolated in the ligaments and switches from bending to compression dominated behavior as the relative density increases. In contrast, due to the presence of enlarged junctions, the deformation mode for the 3D printed nanoporous structures remains bending dominated even at high relative densities. Nanoscale experiments and molecular dynamics (MD)

simulations provide a glimpse into the relative modulus and strength scalings and reveal a more nuanced dependence, with unexpected enhancement in both the relative modulus and relative strength.

Obtaining a clear understanding of the contribution of geometrical structure on the properties of nanoporous metals will significantly advance our understanding of how to tailor NP metal microstructure such as grains, interfaces, and surfaces to enhance the physical properties of the material. Thus, the findings reported here could inform future studies to maximize the versatility and potential of nanoporous metal structures.

CHAPTER 1.   INTRODUCTION AND BACKGROUND

1.1   Background and Goal

Nanoporous (NP) metals are open-cell porous solids, with a feature size range between several to a hundred nanometers. These materials have been proposed as components in battery electrodes, capacitors, sensors, interconnects for power electronics, biological testing platforms, catalysts, [1-8] etc. From a mechanics perspective NP metals pose interesting questions since the individual ligaments themselves are nanosized and when coupled with the high surface area of NP metals may give rise to size effects. To separate size effects stemming from the nanoscale structure, the contribution from the geometrical structure (e.g. porous metal topology) must be known. Considering that they occupy a higher relative density regime than traditional porous solids, the separation of geometrical effects has been a challenge. The main goals of this work are: (1) to uncover the effect of geometrical arrangement in NP metals. To this end, the thesis will explore isolated roles of geometry and size effects with the aid of experiments, macroscale and nanoscale, and atomistic simulations and (2) explore some applications that leverage control of the nanoscale structure.

1.2   Synthesis & Applications

Although several methods have been used to create nanoporous metals (e.g. electrodeposition, template replication, etc. [9, 10]) in this work we consider nanoporous solids fabricated by selective dissolution in an electrolyte through a controlled corrosion process called dealloying [11-13]. In the process, a binary alloy of known composition,

consisting of the metal and a sacrificial component (usually a less noble metal) is used. The sacrificial component is preferentially dissolved in a corrosion process that could either be chemically (free) or electrochemically driven. What is left is a porous structure of the undissolved metal. Controlling parameters could allow for tuning the structure of the foams and ultimately the properties of the resulting structure.

Of the two dealloying processes, electrochemical dealloying is more versatile and can theoretically be applied to any metals with sufficiently different electrode potential values. Electrochemical dealloying is carried out in an electrochemical cell where a potential matching the dissolution potential of one or more of the alloy components is applied to the system, dissolving the less noble component. A schematic of a sample preparation process is outlined in Figure 1. The precursor alloy can be created using a range of alloy deposition technique, but it must satisfy specific composition requirements. Fortunately, several novel deposition techniques permit generation of necessary alloys at appropriate compositions for a variety of nanoporous metals. Thus, under carefully selected conditions, a wide range of complex nanoporous structures can be generated [14]. An even wider range of structures can be developed by taking advantage of the thermodynamics driven processes such as environmental coarsening [15-17] which alters the structure of the nanoporous metals based on the environmental condition.
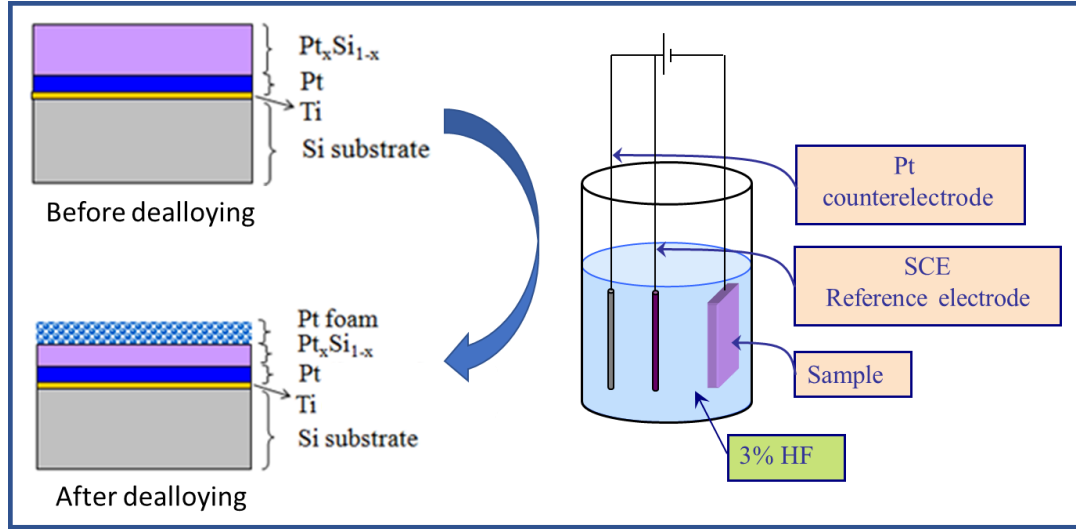
Figure 1: Sample development process for nanoporous metals

1.3 Physical Properties of Porous Solids

Porous solids are a class of air-solid composites. Fueled by their porosity, these materials can demonstrate augmented properties and expand into greater functionalities than their parent materials. Given that nanoporous metals are a subset of porous or cellular materials, attempts to understand and model their mechanics have built on information and approaches already accepted in the broader study of porous solids. These physical properties of the porous solid are dependent on the topology of the underlying structure (number of connections per joint and shape of structural features), the properties of the solid from which the cellular material is generated, and the relative mass fraction or relative density.

Dimensional analysis performed with these factors in consideration have led to scaling relations, that capture the key properties of the porous materials by isolating a representative cell. Such relationships have the form shown in Equation (1) below:

$$porous\ property = C(geometry)^n \times (ligament\ material\ property)$$

$$\Rightarrow Relative\ property = \frac{porous\ property}{ligament\ property} = C(geometry)^n \tag{1}$$

The parameter, C represents a proportionality constant dependent on ligament connectivity while n is a parameter dependent on the dominant ligament deformation mode. The ligament deformation mode can also be impacted by the nodal connectivity. For low-density porous solids, the geometry parameter can be well accounted for by the relative density expression (ρ_f/ρ_s or ρ^* for short) so that expressions for the modulus and strength of a porous material can be estimated following Equations (2) and (3).

$$E_f = C_1 \left({\rho_f}/{\rho_s}\right)^n E_s \tag{2}$$

$$\sigma_{y,f} = C_2 \left({\rho_f}/{\rho_s}\right)^n \sigma_{y,s} \tag{3}$$

Here, the properties E and σ_y represent the modulus and strength respectively with the subscripts f and s indicating porous and fully dense material properties respectively, so that E_f and E_s are the modulus of a porous structure and its matching fully dense version, and $\sigma_{y,f}$ and $\sigma_{y,s}$ are the corresponding values for the yield strength. Values for the parameters C and n can be estimated based on the dominant ligament deformation mode and are unique to the property being examined.

It is possible to use dimensional analysis to find the scaling constants by isolating the dominant deformation mode. For relative densities greater than 1% but less than 30%, where the deformation mode is plastic hinge formation within the ligament, the scalings are derived using beam bending theory as described in [18]. In this manner, expressions such as Equation 2 and 3 can be derived, by relating the ligament deformation to the relative density of the structure. Theoretical exponent values, n, are highly dependent on the mode of ligament deformation. The modulus expression of Equation 2, which for low density structures is derived using beam bending theory on ligaments, has a typical value of $n = 2$ [18, 19]. Strength, as expressed using Equation 3, is driven by the failure of ligaments, which could occur by plastic yielding, buckling, or fracture. As such, depending on the specific failure mode, the value of the parameter n from Equation 3 could range from $n = 1$ to $n = 3/2$. For the most common bending dominated case however, the value can be shown to be $n = 3/2$.

The above analysis can be complicated by factors such as connectivity, and the randomness of the lattice. Relative density can affect the deformation or failure mode if it significantly affects the aspect ratio of ligaments. More slender ligaments for instance, which could be present in structures with very low relative densities, are more prone to fail by buckling whereas structures with higher relative density and shorter ligaments are less likely to be bending dominated. Indeed, it has been hypothesized that at high relative densities, the dominant deformation mode is that of ligament yielding (by stretch or compression). Similarly, the connectivity, or number of ligaments connected to the junction, can affect how the ligament deforms (either by bending or stretching), which in

turns affects overall mechanics. These factors must all be considered when estimating the scaling relations.

The value C is a constant of proportionality that can generally be obtained using more sophisticated modelling or experiments. For instance, the value of C_1 for the modulus is theoretically close to unity since the modulus of the porous structure must approach the modulus of a dense structure as the density approaches a fully dense material. Comparatively, C_2 for the yield strength is approximately $C_2 = 0.3$ based on experiments and numerical computation and could be as low as $C_2 = 0.05$ for buckling-dominated failure or $C_2 = 0.2$ for fracture based failure [18].

1.4 Experimental Techniques

Expansion of the scaling approach to nanoporous metals has relied on experiments on actual samples. However, the relevant testing and characterization approaches are unique from other common materials. This complication arises because of the difficulty of producing and handling large enough test coupons to run conventional mechanical tests. Some researchers have attempted various techniques to circumvent this issue, but each method has its own challenges. The indentation approach has been used to extract core material properties from submicron-scale materials and films. In the indentation process, a tip of known dimensions is impressed on the surface of the material to be tested and a load-displacement curve is extracted and processed for key properties. Factors such as the indent area and max indent depth become most relevant in extracting these material properties; as such, the geometry of the indenter and key qualities of the materials play significant roles. Other factors including the nature of the deformation field under the indenter, which affects

the critical depth for the onset of plastic deformation [20], are also linked to the size and geometry of the indenter tip. Guidelines in this regard have been explored by researchers [20-23]; however, the discussion herein will focus on design considerations unique to nanoporous metals.

Two critical parameters that can be obtained from indentation experiments are the reduced modulus and the hardness of the material being tested. The reduced modulus can be extracted from the indent load-displacement curve: The value is calculated as a function of the initial slope of the unloading curve, and the contact area at the point of max displacement or max applied load [24, 25]. This contact area can be estimated using an area function, which is unique to the indenter tip geometry [24, 26]. With the reduced modulus known, the actual modulus of the tested material can be extracted given that the stiffness properties of the indenter tip and the machine compliance are known [24]. In fact, disparity between the reduced modulus and the sample modulus only exist in the case of non-rigid deformation of the indenter tip along with the sample surface.

The process for extracting the modulus can be applied to nanoporous metals with added consideration for the size of the pores and the compliance of the film. This is especially a concern for lower density porous structures which require a large enough indenter tip diameter to avoid localized deformation that underestimate the modulus. The porosity or size of a porous structure cell must therefore be adequately smaller than the indenter radius [27, 28].

The hardness of a material can be calculated from an indentation test as the max applied force divided by the projected area of contact at the max force ($H = P_{max}/A$).

Once again, an accurate prediction of the hardness is dependent on a carefully derived area function [24, 25]. The yield strength is proportional to this hardness and can be estimated based on the nature of the material and indenter tip used, so that $\sigma_y = C_H H$. For the commonly used Berkovich indenter, this constant of proportionality ranges from $C_H = 1$ to $C_H = 3$ where the lower bound is typically associated with low density porous materials with a plastic Poisson ratio $v^p \sim 0$, while the upper bound is characteristic fully dense solids [29]. The role of this plastic Poisson ratio is explored in greater detail in subsequent chapters. While they are essential in predicting the strength of nanoporous metals, they present a level of uncertainty that warrants further exploration.

Micro-pillar indentation presents an alternate approach that is particularly useful in circumventing some of the uncertainties with conventional indentation experiments, especially as they relate to strength prediction. For this technique, micro-pillars of the material to be tested are prepared using a focused ion beam (FIB) of Gallium ions that mill a portion of the structure leaving enough for compression using a cylindrical flat punch indenter [30]. The technique essentially replicates a conventional compression test at a much smaller case and is thus a convenient alternative to strength measurements by indentation. However, it comes with challenges of its own, and chief of these is the potential impact of the milling procedure on the integrity of the NP metal pillar: ion beam milling could potentially introduce damage to test pillars [31, 32], and in the case of nanoporous metal milling, this ion bombardment could also alter the surface level structure of the nanoporous metal being studied. To prevent this, the micro-pillars used in this study were milled prior to dealloying to avoid compromising the final structure. The micro pillars

are also designed to in aspect ratios that minimize buckling while also maximizing the max load of the indenter.

1.5   Separating material and geometry in nanoporous metals

Armed with these experimental techniques, many researchers have attempted to expand scaling relationships to nanoporous metals. However, NP metals present a two-fold challenge that results from their characteristically high relative densities and the additional uncertainties associated with determining ligament properties: As illustrated in Figure 2, NP metals occupy a parameter regime (yellow shaded region) that exceeds acceptable limits for typical scaling relations to be valid. Hence, any scaling relation applied to NP metals must be verified for the corresponding NP structure. Furthermore, nanoscale effects on ligament deformation, a factor that could also be dependent on the dimensions of individual ligaments [33], create uncertainties in predicting dense/ligament properties, which are necessary for comparison in the structure-property equations.
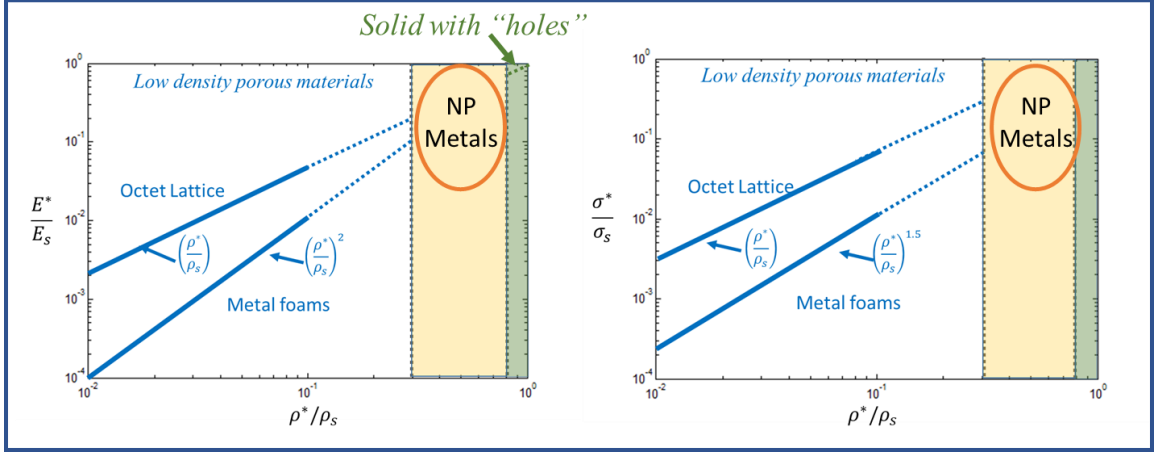
Figure 2: Typical scaling trends for porous solids showing regime occupied by nanoporous metals

The unusual geometry of nanoporous metals also contributes to the complexity in the mechanics. This was best illustrated by K. Hu et al [34] who employ tomographic reconstructions and FEA to demonstrate that geometric parameters such as ligament dimensions alone are insufficient to replicate the Gibson and Ashby scaling values for nanoporous gold. Hence, the Gibson-Ashby laws cannot be directly applied without some correction. Several studies have attempted to understand this geometrical contribution. L. -Z. Liu et al. [35] for instance account for unconnected ligament in relative density estimates, resulting in an effective relative density that could more accurately match with measured scaling values. R. Liu et al. [36] developed modified scaling relationships for the modulus that account for mass agglomeration in junctions.

More unique studies have looked beyond the role of relative density. For instance, Mangipudi et al [37] examined the topological and morphological contribution of the structure by comparing the mechanical response of nanoporous gold to developed spinodal and gyroid structures of equivalent densities. As with K. Hu et al. [34], their report captures

the insufficiency of relative density alone as a predictor of mechanical properties but also highlights new possibilities for creating idealized structures with properties that match with nanoporous metal behavior. Here, and in several other studies, FIB tomography has been used to study the complexities of nanoporous structures for simulation processes. The technique replicates the 3D nanoporous metal structures using compiled images slices taken in a FIB milling process [38]. Ultimately however, the size effects must also be accounted for.

Several studies make efforts to identify size effects at play. Volkert et al. [39] for instance demonstrated that nanoporous Au can have high strength that can only be explained by an increased strength of ligaments. Hodge et al. [40] further employed a Hall-Petch type relationship associated with the size of the ligaments as an added parameter to the property scalings of traditional porous solids since ligaments below a certain size threshold display higher strength than predicted for conventional gold. This enhancement was traced to surface effects in the ligaments, but the exact mechanism of enhancement remained unclear. Other studies such as by R. Liu et al. [33] have demonstrate some of the size effects, using atomistic simulations to show effects of ligament thickness on strength and tension/compression asymmetry. Farkas et al [41] also demonstrated tension/compression asymmetry in ligaments which they account for using modified scaling relations, and Sun et al. [42] used MD simulations to identify some of the distinct size effects tied to the size of ligaments. These studies highlight the importance of accounting both the geometry and size scale effects to fully understand the mechanics of nanoporous metals. However, all the above studies centered on accounting for the size

effects have always assumed that the effect of the nanoporous network on properties is similar to macroscale low density foams.

1.6   Thesis Organization

This thesis is organized into 5 chapters, with most of the work (Chapters 2 through 4) being based on published work or papers pending publication. The core elements of the thesis are presented in Chapters 2 and 3. In line with the overarching goal of better understanding the mechanics of nanoporous metals, these two chapters will explore the two key elements that control the mechanical response: The isolated role of geometry in nanoporous metals will be examined in detail in Chapter 2 with the aid of 3D printing techniques and in plane strain maps. This chapter will examine the specific case of the geometrical structure of nanocrystalline nanoporous platinum, with 5nm sized ligaments, generated using MD simulations, and a randomly generated porous solid at comparable relative densities for comparison. The chapter will examine both macroscopic property scalings and deformation mechanisms in porous solids with similar structure to NP metal but no size effects.

Chapter 3 builds on this with a focus on the local mechanisms and size effects at play for nanoporous metals. The study here, which was aided by extensive simulation experiments and advice by Dr. Garritt Tucker and Dr. Ankit Gupta, along with nanomechanical tests and will explore the dominant size effects at play and their role in the scaling behavior of nanoporous metals.

Chapter 4 will examine a possible application leveraging control of mechanical properties in nanoporous metals, while the final chapter summarizes the key findings and

discusses future work and improvements that can be made to build on the work performed

for this thesis. Supplemental information is included in the Appendix section of a thesis

and referenced where necessary.

CHAPTER 2.   PROPERTY SCALINGS AND DEFORMATION MECHANISMS IN NANOPOROUS SOLIDS IN THE ABSENCE OF SIZE EFFECTS

2.1   Chapter Overview

As highlighted in the introduction, nanoporous metals possess a unique geometry that differentiates them from other classes of cellular solids. One objective of this thesis is to isolate and understand the role of this unique geometry and assess its possible contribution to the atypical mechanics of NP metals. This chapter presents and evaluates an approach to addressing this challenge using 3D printing as a means of replicating and testing NP structures independent of nanoscale effects. The analysis presented aims to capture the primary geometrical contributors and provide a first step towards better mechanical characterization.

The rationale and approach for the study build on the previously highlighted dependence of material properties on relative density. Here, the primary objective is to capture the nature in which the normalized material properties change with altered relative density. To this end, multiple structures of varying density were created and tested, accounting for the fact that any approach should be paired with a means of assessing the relationship between density and deformation mechanics. In line with this, the study presented will involve scaled up structures fabricated at varying densities. Mechanical tests on these structures are aided by strain mapping techniques using digital image correlation, thus capturing the intricacies of density dependence, including the local deformation modes

and failure mechanisms. Furthermore, while the most important structures in this study would be the nanoporous metal (in this case, NP Pt) based structures, matching information on an additional set of structures, with randomized feature orientation is also presented as a basis of comparison to conventional porous solid mechanics.

The chapter is organized as follows: The first two sections elaborate on the methods used in the study, beginning with an overview of the approach used to generate the structures followed by a detailed outline of the experimental testing procedure and approaches. A close examination of the results begins in Section 2.4, starting with an overview of mechanical test results and implications, and followed by a detailed analysis of local behavior in the context of the mechanical test results. The final section summarizes the chapter with the primary conclusions drawn from each portion of the study.

2.2   Preliminary Design and Fabrication of Test Structures

2.2.1   Development Process

Two sets of structures were created for the purpose of this study: The NP Pt structure was developed using molecular dynamics (MD) simulations while the classical (Voronoi based) randomized lattice structures were created using a disordered lattice with 4-nodal connectivity. To aid discussion as related to this chapter of the thesis, the NP Pt structures will be referred to as 3D printed MD-B (MD-Based) NP Pt structures, or MD-B for short, reflecting their method of preparation, while the classical randomized lattice structures will be referred to as 3D printed RF, or RF for short.

2.2.1.1 NP Platinum Structures using Molecular Dynamics

A number of approaches have been proposed and utilized for generating NP metal topologies, with fully-resolved atomistic internal structures [15, 43-45]. The approach taken in the current effort is partly motivated by the underlying interest to allow the system's structural trajectory (e.g., topology, surface, and internal microstructure) to evolve naturally given the imposed thermodynamic conditions. The process is summarized in the schematic of Figure 3 below.
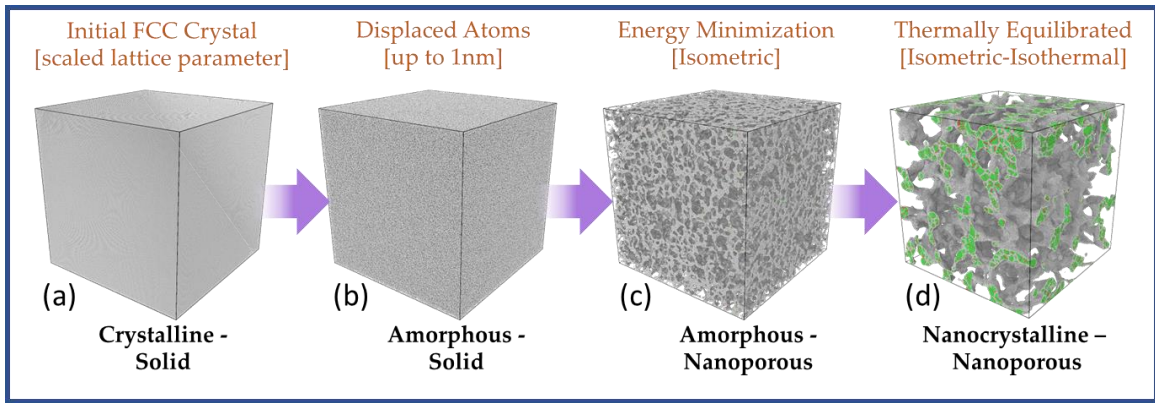
Figure 3: Process of generating NP structures using atomistic simulations

The process follows the procedure detailed by Kolluri et al. [15]: An expanded FCC The process follows the procedure detailed by Kolluri et al. [15]: An expanded FCC simulation cell was initially generated, and the chosen lattice parameter, a_o, was scaled to match the desired target density following complete equilibration. The structures for this work used 3 different target densities of 20%, 30%, and 40% Pt. After the expanded FCC lattice structure was created (Figure 3a), each atom was then randomly displaced by up to 1nm (Figure 3b). Conjugate gradient energy minimization was then employed on the

system to allow the structure to evolve to a lower energy configuration (Figure 3c). Energy minimization is conducted without changing the volume of the simulation cell (i.e., isometric) and usually progresses through a few million steps of the minimization algorithm before the stopping criteria is satisfied. In this work, a stopping energy criteria or tolerance of 1e-16 was set. Following energy minimization, the system was thermally equilibrated to 300K and zero normal pressure in all directions (i.e., isothermal-isobaric ensemble). During thermal equilibration, the seemingly amorphous-nanoporous Pt structure (Figure 3c) evolved to form a nanocrystalline-nanoporous structure (Figure 3d) with the initial target density. The ligaments and junctions following energy minimization coarsen and an internal nanocrystalline microstructure forms.

All atomistic simulations were performed using the LAMMPS software (lammps.sandia.gov) [46], and atomistic structure visualizations were created using OVITO [47].

The resulting structures were scaled for 3D printing; however, to increase the relative size and density of features for mechanical testing, the base MD generated structure was replicated as a unit cell into a hybrid 3X3 unit cell array. Concerns over the impact of this hybridization were addressed by validation mechanical tests conducted on 4 by 4 and 5 by 5 structures. These tests verified that the replicated structure and number of cells used in test samples have limited effect on the overall mechanical response.

2.2.1.2   Randomized lattice structure generation

The base structure for the RF structure was created using a connected lattice with randomized positions to create a 3-dimensional network. The approach follows a similar

17

procedure to that adopted by Makiyama et al. [48] which uses the connected vertices of a Voronoi network as lattice points for an open-cell structure. These lattice points are randomly positioned in 3-D space and the resulting cell edges denote struts/ligaments.

Once this base structure was generated, the relative density was altered by uniformly adding mass to the structure, resulting in a proportional increase in feature size. The resulting structures thus effectively possess consistent connectivity and geometrical orientation so that any observed property changes can be attributed to the impact of feature aspect ratios.

2.2.2 Fabrication by 3D Printing

Once all test structures were developed as outlined above, 3D-printed versions were created for mechanical tests. MD Based structures were scaled up by about 285,000X, while the RF structures were sized to match this dimension range. The resulting 3D printed structures are shown in Figure 4 and Figure 5 along with their original model counterparts to demonstrate the quality of the 3D printing technique, as discussed below.
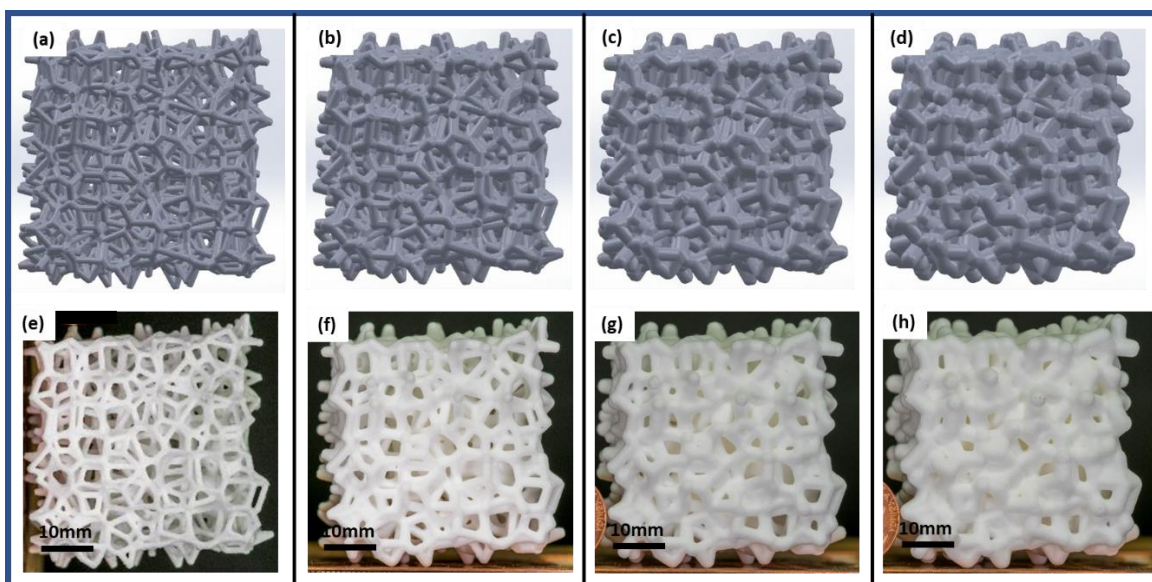
Figure 4: 3D Printed RF structures with original structures as reference, shown from lowest to highest density (left to right)
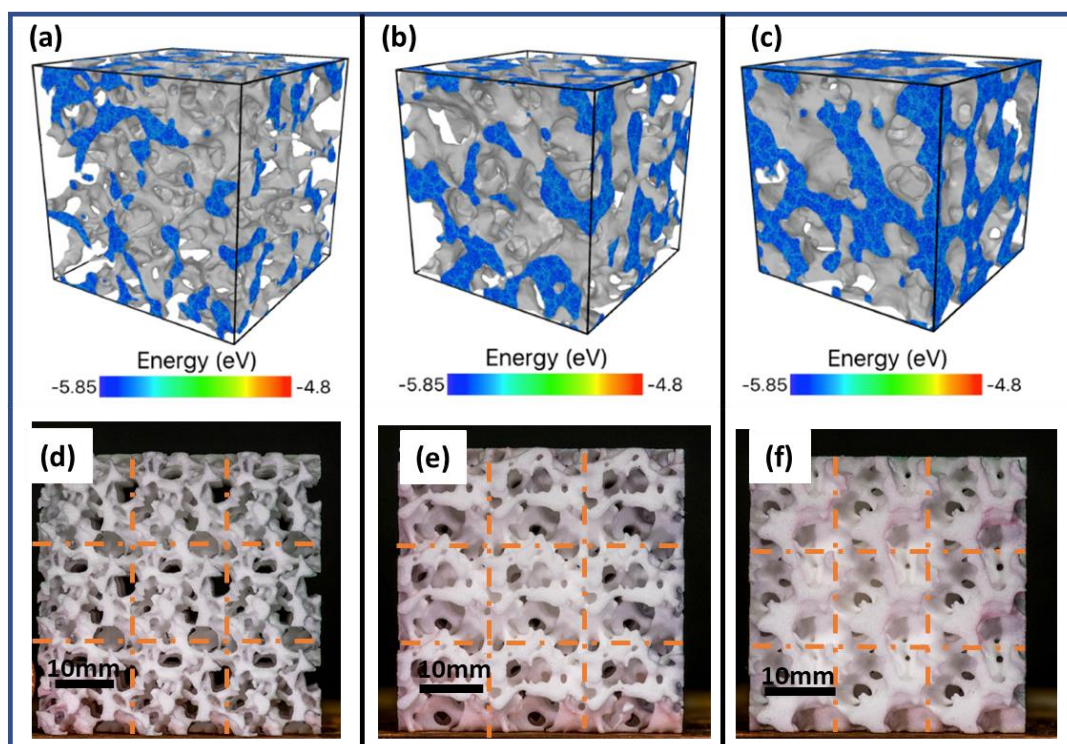
Figure 5: 3D Printed NP Pt structures based on MD simulations from lowest to highest density (left to right)

Given the complexity of the porous solids, several constraints and design criteria factored in to the scaling and prototyping method selection process. Size and technique selection must maximize the applied strain on test samples while preserving necessary complexities. In other words, the test samples needed to be small enough to experience a minimum strain under the available load head, but large enough to not be impacted by the resolution of the printing technique. Ultimately, the selective laser sintering (SLS) rapid prototyping technique proved most viable. This printing was done via the rapid prototyping company, ZoomRP, using a material listed as durable nylon 12.

Company-listed specifications, including the durability and precision of the technique, made this an ideal option for the study: As specified by ZoomRP, the SLS technique, which uses the durable nylon 12 material, yields parts consisting of discrete material layers that are ~0.1mm – 0.15mm thick. Such resolutions made it possible to capture small features of the structures under the selected scaling. Furthermore, while the presence of discrete development layers is unavoidable in many additive prototyping options and may affect the homogeneity of 3D printed solids, the very small layer thickness characteristic of the SLS technique makes the structural effect relatively indistinguishable for our purposes. We confirm this with a simple homogeneity test where solid cube samples of the same dimensions, developed in vertical and horizontal orientations respectively, were tested under compression (see Figure 6). Figure 6 shows that the 3D printing technique yields homogenous solids. This was an especially important factor to consider given the complexity and detail involved in our parts. The results of the compression tests also served as a means of verifying the properties of the 3D printing material which are used when normalizing experimental values.
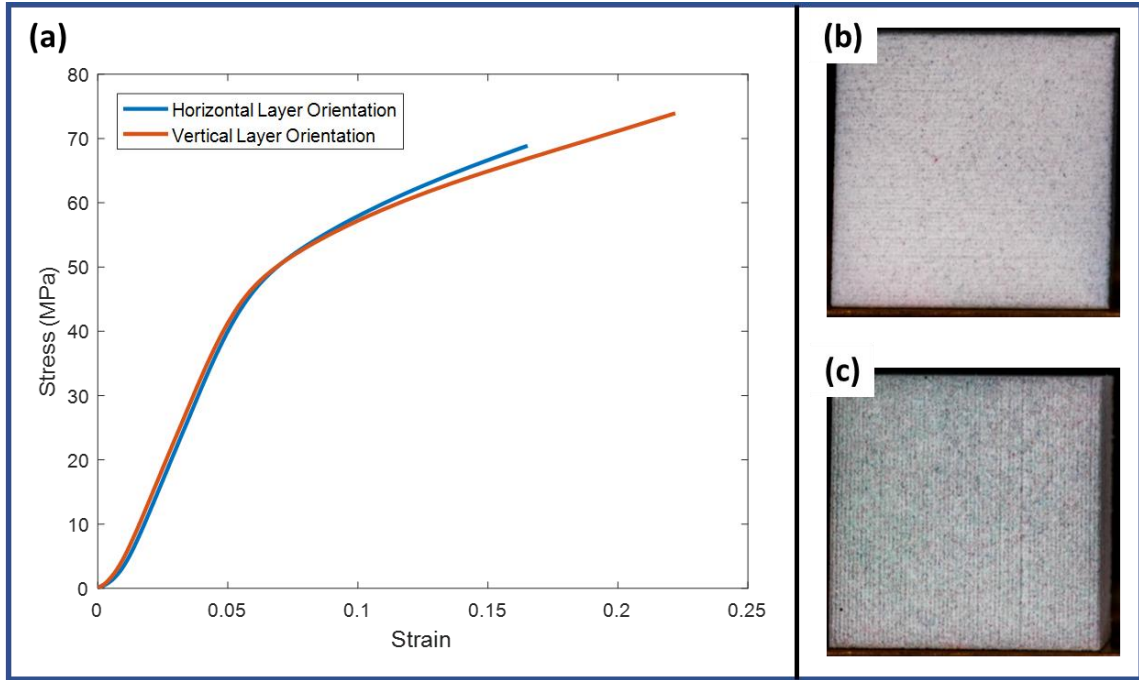
Figure 6: Homogeneity test for printed samples showing (a) stress-strain curve for (b) horizontal and (c) vertical layer orientation

The nylon 12 material used in the SLS technique also presents the added benefit of a paper-like surface, a quality that allowed for the creation of paint speckle patterns on sample surfaces, as was necessary to monitor deformation using digital image correlation (DIC). The final size and quality proved ideal for capturing a large enough deformation under the available load head while preserving necessary structural details and capturing local deformation. Ultimately, the generated structures using the SLS technique addressed the need for homogeneity, detail, and provided an excellent surface for patterning.

2.2.3 *Sample Patterning for Strain Mapping*

Prior to testing, the 3-D printed samples were patterned in accordance with the requirements for strain mapping with DIC: For best results out of a DIC analysis, an imaged specimen must have a unique pattern that can be mapped during image acquisition. This

pattern was created by spray-painting the sample surfaces. The resolution of the DIC strain measurements would depend on the speckle pattern quality, which is dependent on the resolution of the camera and the extent to which the object is in the camera's field of view. Based on the test camera resolution for this study, the speckles had to be between 60 to 100 microns in size to give the best results.

Patterns were generated on samples using airbrush tools, which include an IWATA CM-B custom micron brush, and CREATEX Opaque airbrush colors. The particle size and nature of the speckles was dependent on the compressor pressure, distance between sample and airbrush when spraying, and the paint to illustration base mixing ratio, all of which we controlled to maintain an appropriate and consistent paint pattern distribution. In addition, combining several colors (black, blue, red, yellow, and green), made it possible to increase the grayscale dynamic.

2.3   Experimental Procedure

Following the generation of the 3-D printed samples, key information necessary for the complete evaluation of the structures was extracted. The goal of this section is to explain the processes for characterizing the geometry, summarizing the mechanical response (specifically the modulus and strength), and capturing the local behavior of the structures, while highlighting their implications.

2.3.1   Characterization Process

Prior to any form of physical testing, all test samples were characterized for their relative density and other key geometrical parameters, which include the average ligament

length, average ligament thickness and the average junction diameter. The density was calculated using the sample mass, measured and reported to a precision of .01g, and the overall volume, which was measured using calipers to a precision of .01mm. Table 1 summarizes the results of these measurements. The relative density was obtained by normalizing measured density based on the density of a fully dense 3D printed cube, the same sample used for homogeneity tests. It is important to point out that given the intricate relationship between the density, structural properties and the mechanical response, these parameters were based on entirely on characterization results and not on design requirements. For instances where slight variations from design specifications were observed, these were not ignored so that all results reflect actual structural information.

Table 1: Measured Properties of 3D Printed Samples

	Height (mm)	Mass (g)	Volume (mm^3)	Density (kg/m^3)	Rel. Density
Category 1: Voronoi generated (Random) foams					
RF14	45	11.65	91125	127.8	0.14
RF32	45	27.13	91125	297.7	0.32
RF52	45	43.68	91125	479.3	0.52
RF72	45	60.15	91125	660.1	0.72
Category 2: MD generated foams					
MD20	50	20.35	125000	162.8	0.20
MD30	43.6	22.13	82881.9	267.0	0.30
MD40	39.5	22.79	61629.9	369.8	0.40
Fully dense sample					
Dense	25	14.4	15625	921.6	1

In addition to the relative density, local structural properties were extracted for each sample using a skeletonization process, which was performed on 2-D projected masks of surface level structural features. Figure 7 shows a schematic of the major features (ligament length, l, ligament thickness, t, and junction diameter, j) in a subset of a symbolic porous structure.
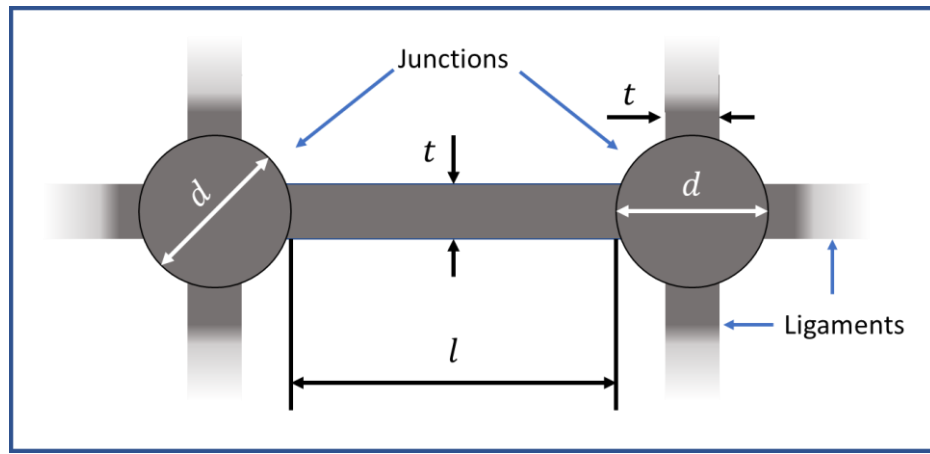
Figure 7: Schematic showing junction and ligaments as described in this work

Figure 8 summarizes the major stages of the skeletonization aided process (more details on the approach included in Appendix B) using a subset of the reference mask for the lowest density RF sample for illustration. The initial skeletonization process reduced the masks to pixel-thick frame works using MATLAB's skeletonization function, as illustrated in Figure 8(a). A MATLAB script was then applied to identify joints (smaller blue circles in Figure 8(a)) and construct circles that fit within the junction (larger red circles). Subtracting these circles thus gave an approximation of the node and ligament masks as shown in Figure 8(b) and Figure 8(c), from which a simple trimming procedure yielded the isolated ligaments of Figure 8d.
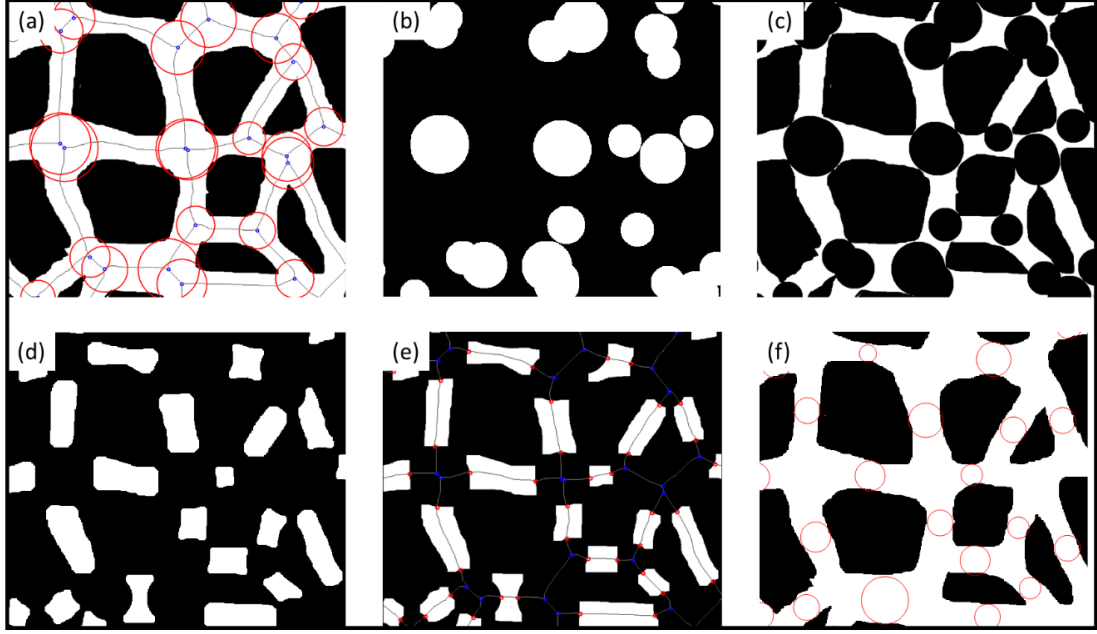
Figure 8: Stages of skeletonization process

Other essential parameters such as junction diameter and ligament characteristics (length, thickness and orientation) were extracted as follows: Node (or junction) properties were obtained based on the area of isolated features in the node mask of Figure 8(a). Ligament length and orientation were estimated using the ligament endpoints, which were identified as the intersection between the skeleton and isolated ligament edges, as illustrated in Figure 8(e). Using these endpoints as reference, an estimated length and orientation was obtained as the distance and orientation of a line connecting the respective endpoints. Finally, the thicknesses of ligaments were estimated by first identifying the center of ligament features and constructing circles that fit within the bounds of the mask, as shown in Figure 8(e). The diameter of each circle was recorded as the thickness of the corresponding ligament.

The obtained structural information, once normalized, is necessary for characterizing porous solid structures based on geometry. Two important normalizations,

which are the ligament aspect ratio, captured as the ratio of ligament thickness to length (t/l), and the junction size ratio, captured as the ratio of node/junction size to ligament thickness (j/l), capture the ligament and junction prominence, respectively. Measurements followed the following guidelines: t/l was measured individually for each ligament, while measurements for j/l followed a similar process except that the ligament length used for the j/l measurement of each junction was the average length of all ligaments connected to the junction. Figure 9 summarizes these measurements for tested samples, showing typical distribution of values for each of the samples used in the study. The often-non-uniform distribution of the parameters complicates attempts at averaging values. As such, overall averages may not be an accurate descriptor and are avoided in the study. Histograms such as shown in Figure 9 are used for comparison in lieu of averaged measurements
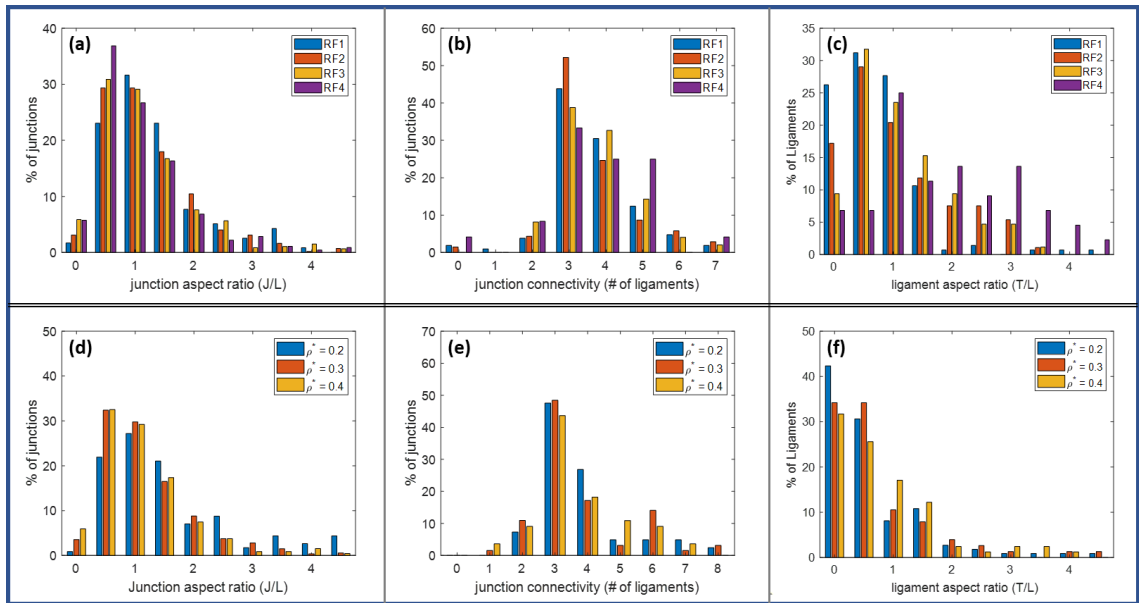
Figure 9: Histograms showing distributions of key structural features for random (a-c) and MD Based (d-f) structures

2.3.2 *Mechanical Testing and Imaging*

Once properly characterized, all structures were tested in compression using a SATEC Systems Inc. testing stage, model number TC-110, with a 100KN max load. This test was performed under displacement-controlled conditions and a constant strain rate of 0.007/s (~0.02mm/s). All samples were tested up to ~15%. The loading was paused at regular intervals to capture the images for DIC analysis. All images from the mechanical testing procedure were captured using an STF-8300M camera manufactured by SBIG with a Canon 18-55mm DX lens in the 35mm zoom stage, to ensure minimal lens distortion. The camera features a Kodak KAF-8300 CCD Sensor with a resolution of 3352×2532 pixels. The aperture was set at 3.5 for a shallow depth of field that minimizes background effects during DIC analysis. Captured images were stored in an SBIG file format, from which we obtain TIFF versions using the SBIG software. The software allowed for the control of image properties, enhancing them solely for improving the DIC analysis process.

From the compression tests, material properties including the elastic and plastic Poisson ratio ν_e and ν_p, the yield stress σ_y, and the modulus E, could be inferred. The modulus was obtained from the linear regime, neglecting the initial non-linear contact development region of the stress-strain curve, while the yield strength was based on the 0.2% offset technique. Similar tests on the fully dense sample yielded equivalent dense material properties and provided information necessary to evaluate the compliance of the testing frame, which was accounted for prior to evaluating the relevant parameters: By comparing the strain-behavior obtained using both strains (device readings and DIC), it was possible to quantify the compliance of the machine and account for this machine

27

compliance in stress-strain data. This additional step ensured the accuracy of the results used for analysis.

The Poisson ratio was estimated using images acquired during mechanical testing. To measure the Plastic Poisson ratio, images acquired after yield were used to estimate the plastic Poisson ratio by measuring the change in vertical and horizontal dimensions at each stage as compared to the original height and width. Figure 10 gives a schematic of a sample Poisson measurement for a sample. For this measurement, images taken after yielding were used to obtain strains associated with the corresponding load-displacement position and the subsequent plastic Poisson ratio was calculated from this. The vertical and horizontal dimensions were measured from the reference images of each sample and compared to the values of the same dimension after yield. From this, we obtain the engineering x and y strain ε_x and ε_y respectively, and with that the plastic Poisson ratio following the relation $v_p = -\varepsilon_x/\varepsilon_y$. Values from several positions after yield were averaged and reported as illustrated in Figure 10.
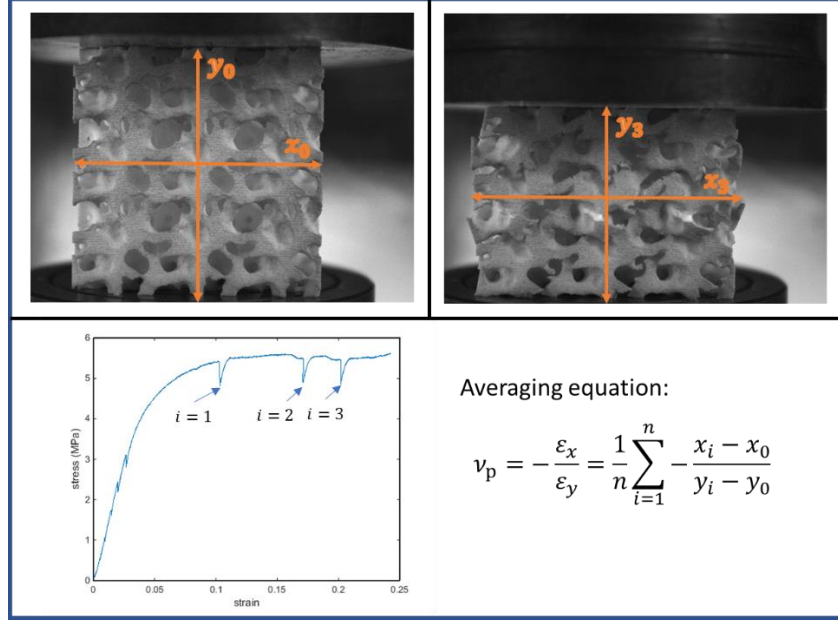
Figure 10: Measurement of Plastic Poisson Ratio

2.3.3 Strain Mapping using Digital Image Correlation

Local characterization was made possible by imaging the patterned sample surfaces while compression tests were in progress. Acquired images were post-processed using digital image correlation (DIC) to obtain in-plane strain maps of sample deformation. This was achieved by comparing images of a sample surface at different stages of a loading test; the changes in surface patterns due to loading can be examined and a map of the strain in the material can be derived [49, 50]. Given the 3-dimensional nature of the structures, in plane strain maps must examine surface level features alone. Accomplishing this required incorporating an imaging mask during post-processing to isolate applicable regions of the structure while overlooking out-of-plane regions. This mask was generated based on the reference image for each sample. The shallow depth of field, which was characteristic of all acquired images, allowed for better focus on the struts closest to the camera. A threshold applied to the images increased the contrast between in-focus and out-of-focus regions.

The resulting images were inverted so dark regions are regions of interest and light regions are neglected regions. The resulting masks (shown in Figure 11) were incorporated into a DIC analysis procedure using the open source image correlation software, NCorr [51]. Results were post-processed for additional information as outlined shortly in Section 2.4.3.
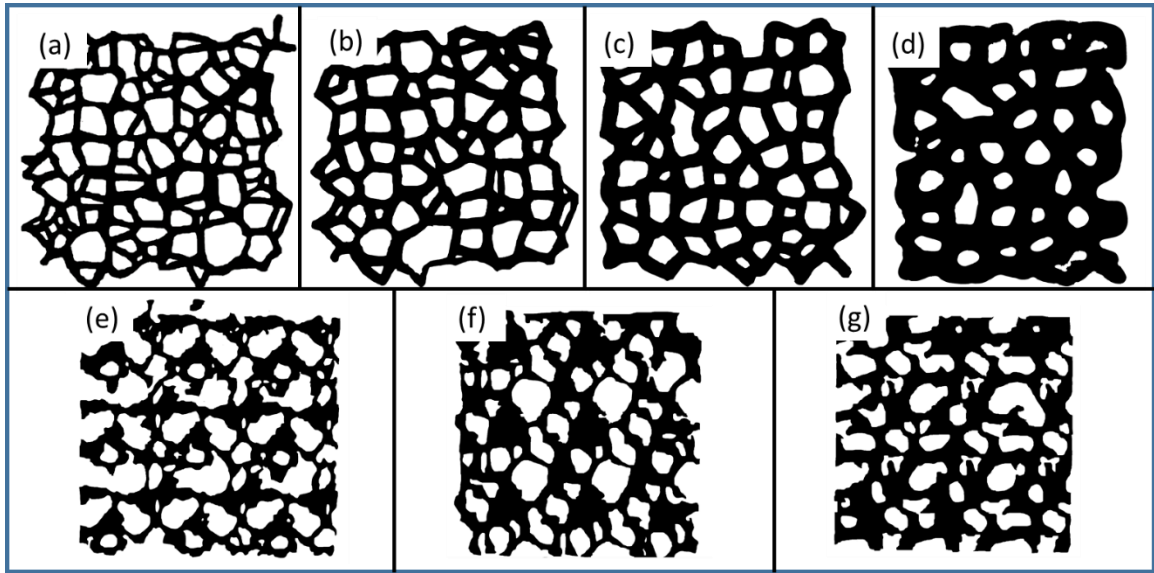
Figure 11: DIC strain masks for RF (a through d) and MD based (e through f) structures

2.4   Results and Evaluation

2.4.1   *Material Properties from Uniaxial Compression Tests*

The resulting stress-strain curves from the mechanical testing portion of this study are shown in Figure 12, with stress in MPa on the y-axis and strain on the x-axis: Figure 12a shows the stress-strain curves for the 3D Printed RF structures while Figure 12b shows trends for the MD-B structures. The stress shown is the engineering stress, calculated based on the initial cross-sectional area while the strain was calculated relative to the original

length from Table 1. The drops in the stress-strain curves are the result of pauses in the compression experiment for DIC image acquisition. The curves for the MD porous solids show two main regions: an initial linear region representative of elastic response, followed by a nearly steady plateau after yield. The slope of the linear elastic region is used to obtain the modulus. The initial lower-slope region characteristic of the RF solids in Figure 12a is likely a result of contact establishment between the platens. This is followed by a second stiffer region and a plateau region like that observed in the MD porous solids.
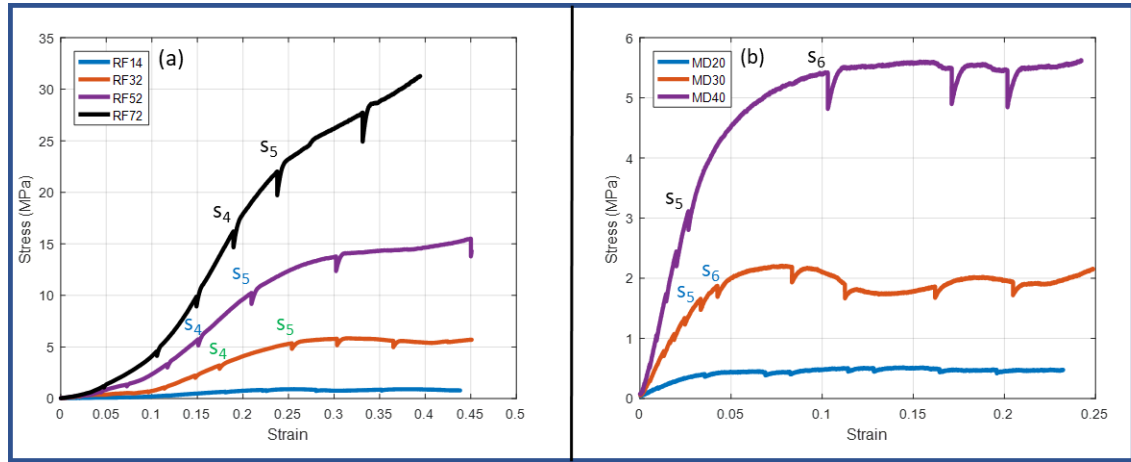
Figure 12: Macroscopic stress-strain curves for (a) RF and (b) MD based structure sets

For a more relevant evaluation of the test results, in line with the scaling relations of Equation 1, the yield strength and modulus were normalized with properties of the fully dense solid to obtain relative modulus (E/E_s) and relative strength ($\sigma_y/\sigma_{y,s}$). The yield point for each curve was obtained by offsetting the linear curve by 0.2%. Figure 13 shows the relative modulus (E/E_s) in Figure 13a and the relative yield stress or strength ($\sigma_y/\sigma_{y,s}$) in Figure 13b, each as a function of relative density (ρ/ρ_s). The red diamonds in Figure

13 represent data points for the 3D Printed MD porous solids while the blue circles correspond to the RF (Voronoi, Random) porous material data.
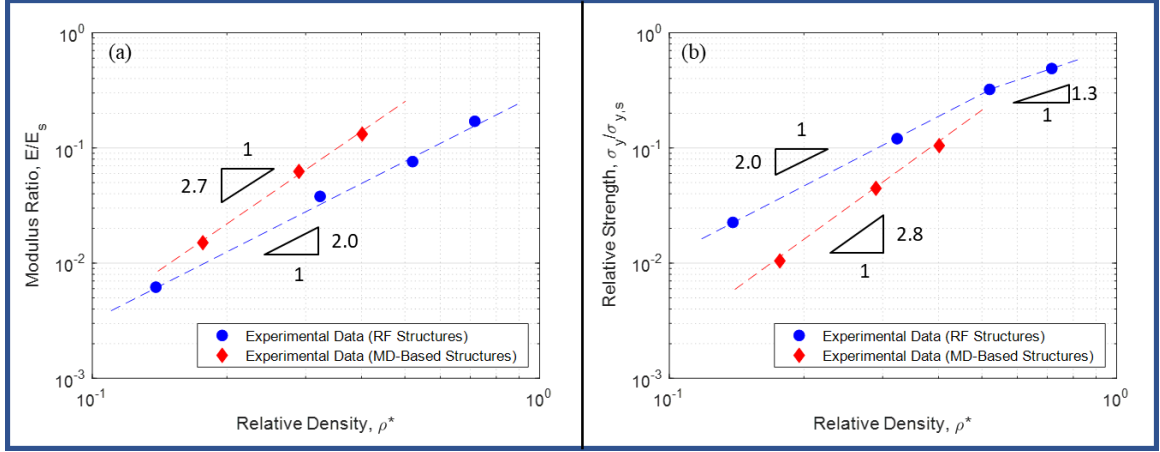
Figure 13: (a) Relative modulus vs. relative density and (b) Relative yield strength vs. relative density for RF and MD based structures showing power law fit to data

In addition to this information, Figure 14 shows the dependence of plastic Poisson ratio on the relative density. All plots use log-normalized axes to aid visualization of trends. The discrepancy highlights the complicated influence of the foam architecture on the relationship between relative density and overall foam properties. Of the mechanically tested porous solids, the MD porous solids show overall higher stiffness (E/E_s) values for similar ρ_f/ρ_s and lower strength, $\sigma_y/\sigma_{y,s}$ values. In addition, the difference in slopes of the distributions, reflected in the value of the n exponent in Equation 1, further suggests an added effect of foam architecture on the sensitivity of foam properties to relative density.
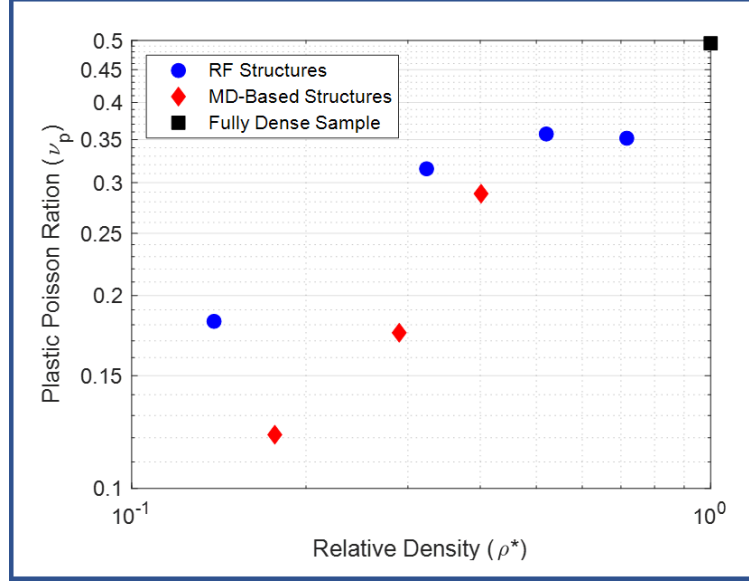
Figure 14: Average plastic Poisson ratio for experimental data as a function of relative density

2.4.2   Strain Mapping Results

As highlighted previously, the unique deformation loads and load configurations within the foam architecture contribute to the overall behavior of the porous solids and complicate the mechanical response. Therefore, to predict mechanical properties, it is necessary to understand the primary modes and loading configurations involved in the structural scale of porous solids. For this reason, the DIC approach was adopted to analyze the architecture mechanics of the 3D printed structures. Greater emphasis was placed on deciphering key mechanisms of the RF structures given that these provide a benchmark for what should be expected.

A complete DIC analysis provided data on the in-plane strains, as outlined previously. This data alone was insufficient to draw conclusions on the mechanics of foam deformation, for which dominant strain and deformation modes are not restricted to the

33

primary axes (x, y and x-y) directions; hence, additional strain transformations were performed to obtain distributions that are more descriptive. The analysis involves several steps, each of which reveals more mechanics information. The remainder of this sub section outlines these steps and resulting behaviors.

The first set of transformations, the maximum principal strains, served to highlight high strain regions in the porous solids, independent of loading orientation. These principal strains were calculated using Equation 4, where ε_{xx}, ε_{yy} and ε_{xy} represent the strains in the x, y and x-y directions respectively, from the DIC analysis. The resulting distributions show the regions of highest strains, and, with the help of yield analysis data discussed shortly, also highlighted the struts or regions primarily responsible for failure of the porous solids.

$$\varepsilon_{p1}, \varepsilon_{p2} = \frac{\varepsilon_{xx} + \varepsilon_{yy}}{2} \pm \sqrt{\left(\frac{\varepsilon_{xx} - \varepsilon_{yy}}{2}\right)^2 + \varepsilon_{xy}^2} \qquad (4)$$

Two DIC analyses were performed on both classes of porous solids using the same set of acquired images. The first analysis, the complete analysis, used an image of the un-deformed foam as the reference image for calculating strains. This provided strain maps for all stages of the compression test relative to the undeformed configuration. The second DIC analysis, the yield analysis highlighted previously, made use of the image captured immediately before yield as the reference image, resulting in strain maps for subsequent load stages. The purpose of the latter analysis was to capture the straining process during yielding and highlight the primary regions responsible, as will be discussed. Figure 15 a

through d show the positions examined for the yield analysis on the respective stress-strain curves. Once again, this yield point was estimated using the 0.2% offset approach, neglecting the initial non-linear regime of the curves. Figure 15 and Figure 16 show these strain maps for both RF and MD structures, analyzed for images taken shortly after yielding.
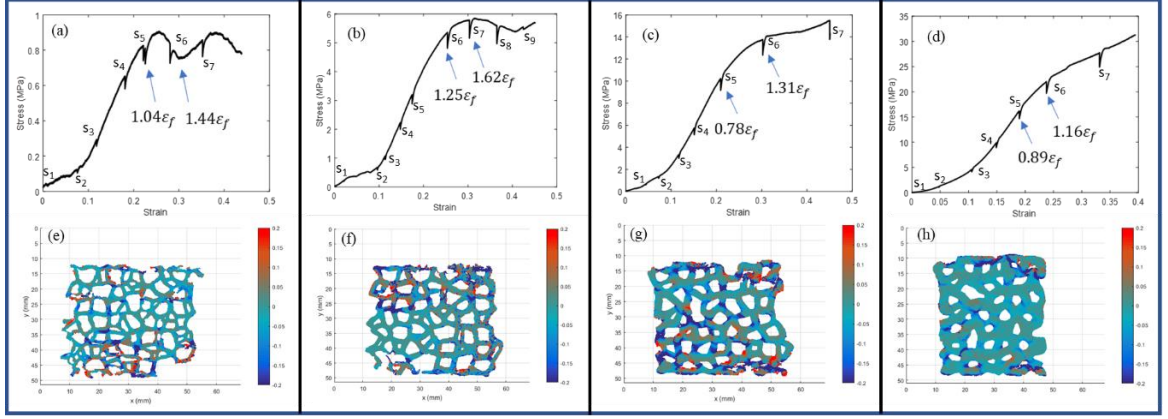
Figure 15: (a-d) Macroscopic stress-strain curves for RF structures. (e-h) In-plane max principal strain distributions accumulated between marked points on stress-strain curves
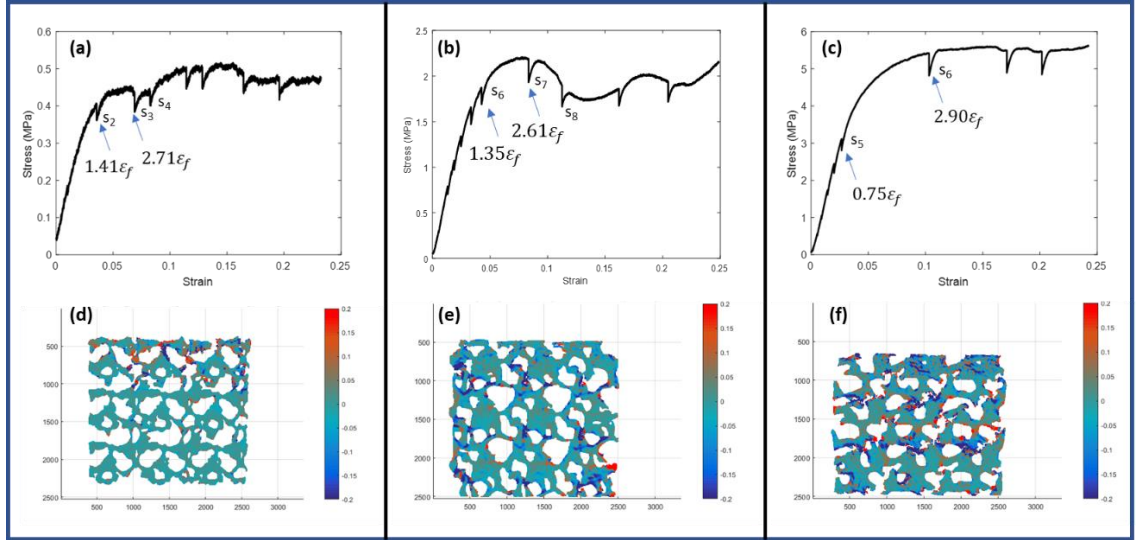
Figure 16: (a-c) Macroscopic stress-strain curves for simulation-based structures. (d-f) In-plane max principal strain distributions accumulated between marked points on stress-strain curves

2.4.3 *Examination of Local Deformation Mechanisms in RF Structures*

The above strain mapping results can be leveraged to interpret key aspects of the local behavior and their dependence on structural features. In an ideal situation, the ligaments of a given structure represent the most critical of these features, often driving

36

overall deformation; For this reason, the analysis below isolates and examines the mechanics of these individual ligaments, and to some extent junctions, in the context of the overall behavior. Ligaments were isolated for this purpose in both data sets; and in the case of the MD-G structures for which a clear definition of features is not immediately apparent, the skeletonization algorithm described in Section 2.3.1 served as an objective means of defining ligaments. The analysis begins with the RF structures, which serve as a benchmark for comparison.

2.4.3.1 Key RF structure mechanics

Following the isolation of struts in each of the RF samples, individual struts were labeled and selected based on their contribution to failure. This selection, which was based on the results of the yield analysis, follows the assumption that at the point of structural yielding, select ligaments and features undergo significant deformation, driving the overall failure. The goal of this analysis, therefore, is to determine the failure mode of these critical ligaments and thus understand the dominant failure mode of porous solids at each relative density.

Once failure ligaments were identified, their strain distributions were examined using histograms. This made it possible to decipher the typical failure mode of the ligaments. The principle behind the approach to interpreting the distributions is illustrated in Figure 17, which anticipates failure by one of two deformation modes, or some possible combinations of them. The bending failure mode of Figure 17b will result in portions of the struts being under compression and portions under tension. Similarly, a strut completely under compression will have all portions under compression, as illustrated in Figure 17c.

To capture this compression vs. tension behavior along the strut, strains were resolved to their normal and tangential components, as illustrated in Figure 17a, using Equations 5 and 6. The more relevant component however will be the normal component.
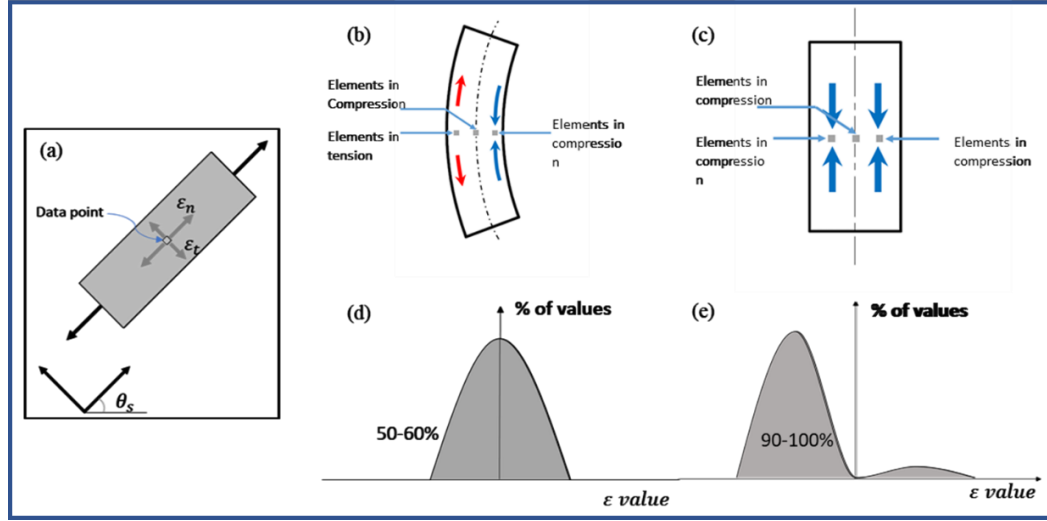
Figure 17: Schematic of a ligament showing normal and tangent strains at a material point, (b-c) schematic depiction of tension and compression dominated deformation of an individual strut, (d-e) schematic of expected histogram distributions.

$$\varepsilon_n = \varepsilon_{xx} \cos^2 \theta_s + \varepsilon_y \sin^2 \theta_s + 2\varepsilon_{xy}\sin \theta_s \cos \theta_s \tag{5}$$

$$\varepsilon_t = \varepsilon_{xx} \cos^2(\theta_s + \frac{\pi}{2}) + \varepsilon_y \sin^2(\theta_s + \frac{\pi}{2}) + 2\varepsilon_{xy}\sin (\theta_s + \frac{\pi}{2}) \cos(\theta_s + \frac{\pi}{2}) \tag{6}$$

Following this approach, the percentage of the normal strain under tension vs. compression can be examined. This was captured using histograms, as illustrated in Figure 17(d) and (e): An ideal bending behavior would yield an even (or normal) histogram distribution, following the principle that an equal proportion of measurement regions from

the DIC analysis capture tensile and compressive strains; compressive behavior on the other hand would yield a skewed histogram that captures primarily compressive strains. Actual histograms can be expected to deviate slightly from these behaviors due to factors such as the bending orientation of the struts and the presence of transition failure modes. However, one can still expect to gain a broad understanding of failure modes by comparing these different sample distributions. Figure 18 displays the results of this analysis. Figure 18 (a-d) shows the normal strain distributions for each of the RF structures in order of increasing density while Figure 18(e) through h show the resulting histograms for these distributions.
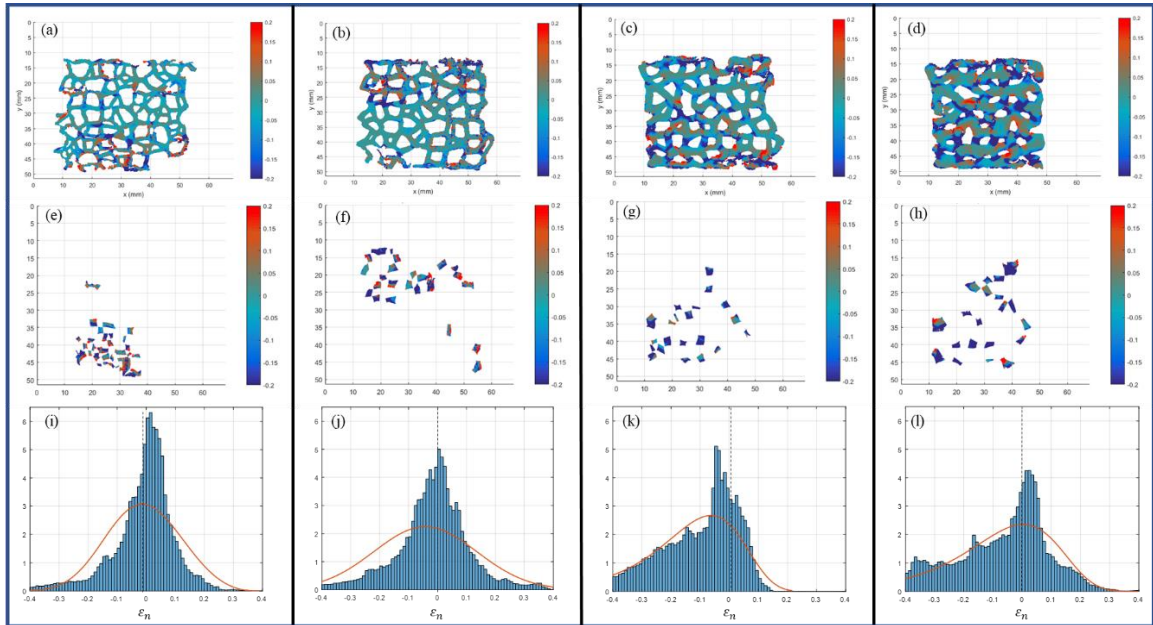
Figure 18: Isolated failure ligaments for RF structures (e-h) with normal strain distributions

The first set of conclusions come from histograms of Figure 18, which show that each of the RF structures has a unique deformation mode associated with them. In this

39

figure, the RF1 and RF2 porous solids appear to be predominantly uniform and centered around zero strain. This suggests a bending dominated behavior where struts are under an even combination of tension and compression loading. The RF3 sample on the other hand shows a larger tail on the negative portion of the strain axis, implying a greater contribution of compressive strains. It can thus be inferred that this random structure undergoes a transition to a compressive dominated behavior. The RF4 structure shows a similar trend, however with an observed increase in density of low tensile strains. One possible explanation for this could be that the deformation becomes analogous to that of a solid with holes; alternatively, a more complex loading mechanism could be involved. For the former situation, stress concentration due to loading around the holes may have led to regions of tension that decrease further away from holes. The latter hypothesis is discussed shortly.

A second noteworthy observation is the nature of failure localization within the ligaments, as can be observed from Figure 18. This localization is further illustrated in the histograms of Figure 19 and the resulting deformation bands are shown in Figure 20. Here, a clear localization of the ligaments driving failure is apparent for the lower density structures (a through h). However, little localization for key failure loads is observed, likely in correlation with the observed trend shift. It can be concluded from these findings that strain localization or deformation bands are more likely to occur for lower density porous solids, where the weaker bending struts are unable to fully distribute applied loads. As the density increases, this localization becomes more diffuse, ultimately becoming completely uniform for higher densities. As a result, in addition to the deformation mode effect, changing localization conditions affect the sensitivity of foam properties to relative density changes.
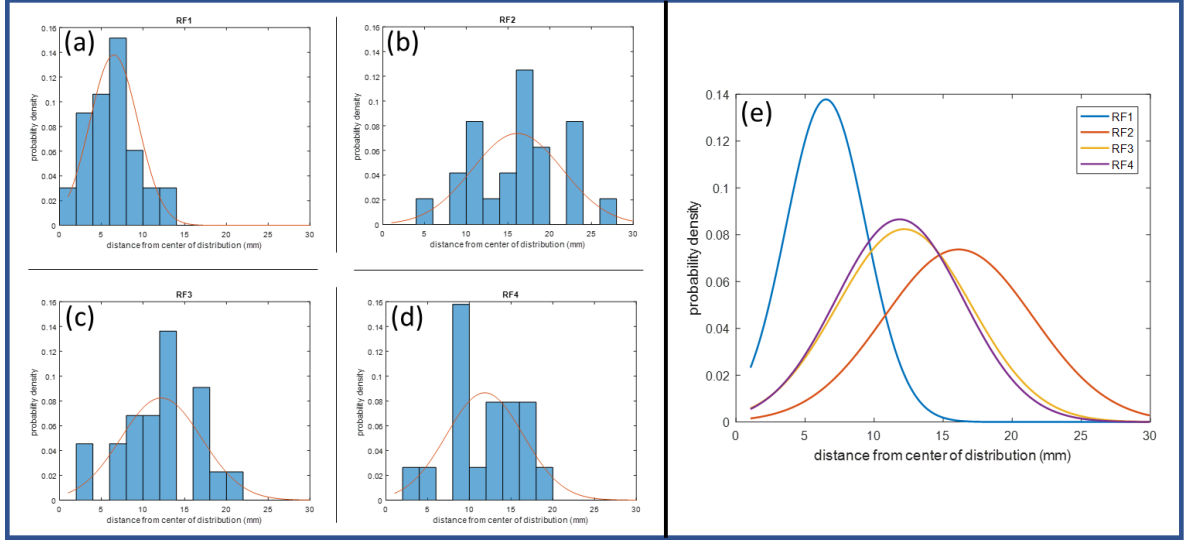
Figure 19: Distribution of struts responsible for failure with estimated normal distribution using mean and standard deviation, (a) – (d) show the distribution of subset of failure struts. (e) superimposes normal distributions in single plot
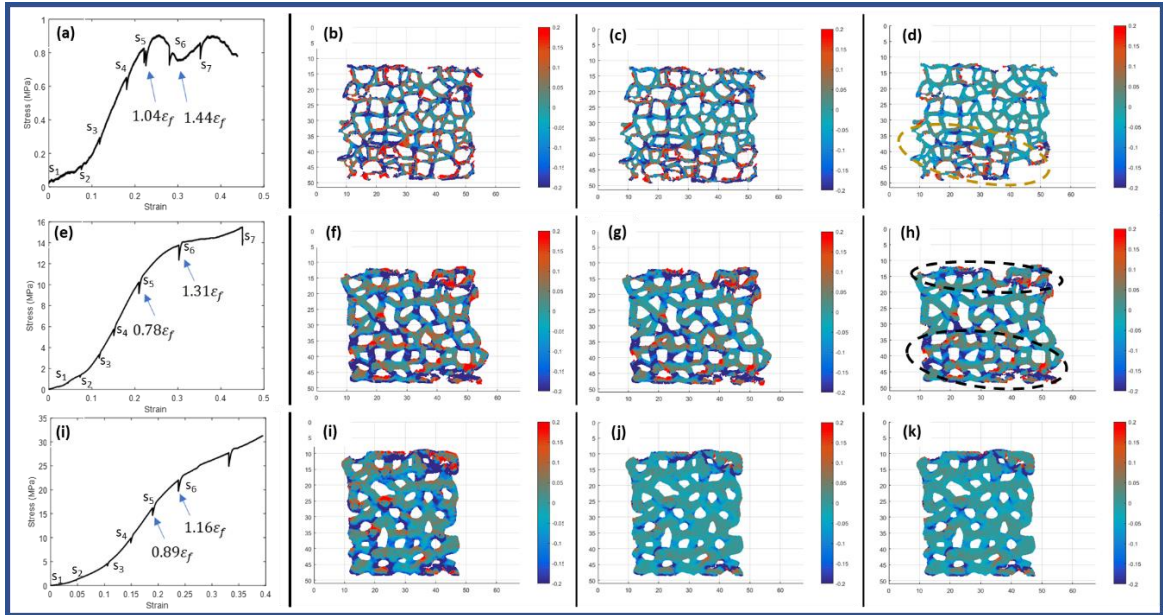
Figure 20: Snapshot of strain distribution for (a-d) RF14, (e-h) RF52 and (i-l) RF72. Strain maps represent strain accumulated from unloaded state to s6 (b, f, and i), between s4 and s6(c, g and j), and between s5 and s6 (d, h, and k).

As a side note, in addition to the bending behavior, a closer look at the histograms also give clues to a mixed mode deformation mode in the structures. This mixed mode

41

behavior is most apparent from the histograms of the lowest and highest density structures, which show a slight shift in the neutral line of the distributions towards the positive, tensile side. Such a shift could be explained by combined loading conditions that causes resolved low-level normal strains along the ligament to be observed. This could point towards higher shear than expected in ligaments or junctions, which could prove significant. The loading scenario may also provide clues to the observed Poisson ratio behavior of Figure 14, however, a closer examination and more detailed study is necessary for any definitive conclusions to be made.

To summarize this discussion so far, the findings show a deformation mode shift that could explain the slope shift in the RF trend of Figure 4. For RF1, with the lowest density, strains are normally distributed about zero strain with minimal spread suggesting prominent bending behavior, as expected based on Figure 17. The RF2 structure shows a similar but much broader distribution along a mean strain shifted to the compressive region of the strain axis, implying a transition to compression dominated behavior. The RF3 foam shows completely compressive dominated behavior, with strains localized in a narrow distribution about a negative strain value while the RF4 with a mean compressive strain value, also shows a broader distribution due to the added tensile strains that result from the solid-with-holes effect. These results suggest that the scaling relationship for a conventional solid at high density is driven, at least in part, by a transforming load accommodation behavior, which transitions ligament deformation from bending dominated to compression dominated. This is already in contrast to the conventional scaling relations for lower density solids, which assume a single type of deformation behavior (typically bending) that dominates at all densities.

While these findings may prove applicable and descriptive of the RF structures, the nanoporous Pt structures of Figure 13 still show scaling differences, meaning the conclusions so far do not perfectly explain the NP Pt mechanics. To understand the source of this discrepancy, a similar analysis of the MD-based structures is in order and discussed next.

2.4.3.2   Comparison to MD-generated structures

Using the RF results as a basis, the structural behavior of the MD-based structures can be assessed for abnormalities. To this end, Figure 21 builds on the method of examination presented earlier, providing information analogous to Figure 18 but for the MD based structures. From this figure, specifically the histograms of Figure 21(g-h), it is apparent that unlike the RF structures which demonstrate a transition in critical ligament deformation modes with increasing density, the ligaments of the MD-based structure appear to maintain a bending dominated behavior at all densities. This implies that although the NP Pt structures have relative densities comparable to the RF solids, the scaling trends are likely independent of the ligament deformation mode, as has been assumed for classical scaling predictions. Furthermore, except for the lowest density structure which experiences some mechanical collapse, the ligaments that drive failure appear to be more evenly distributed at comparative densities to the RF structures.
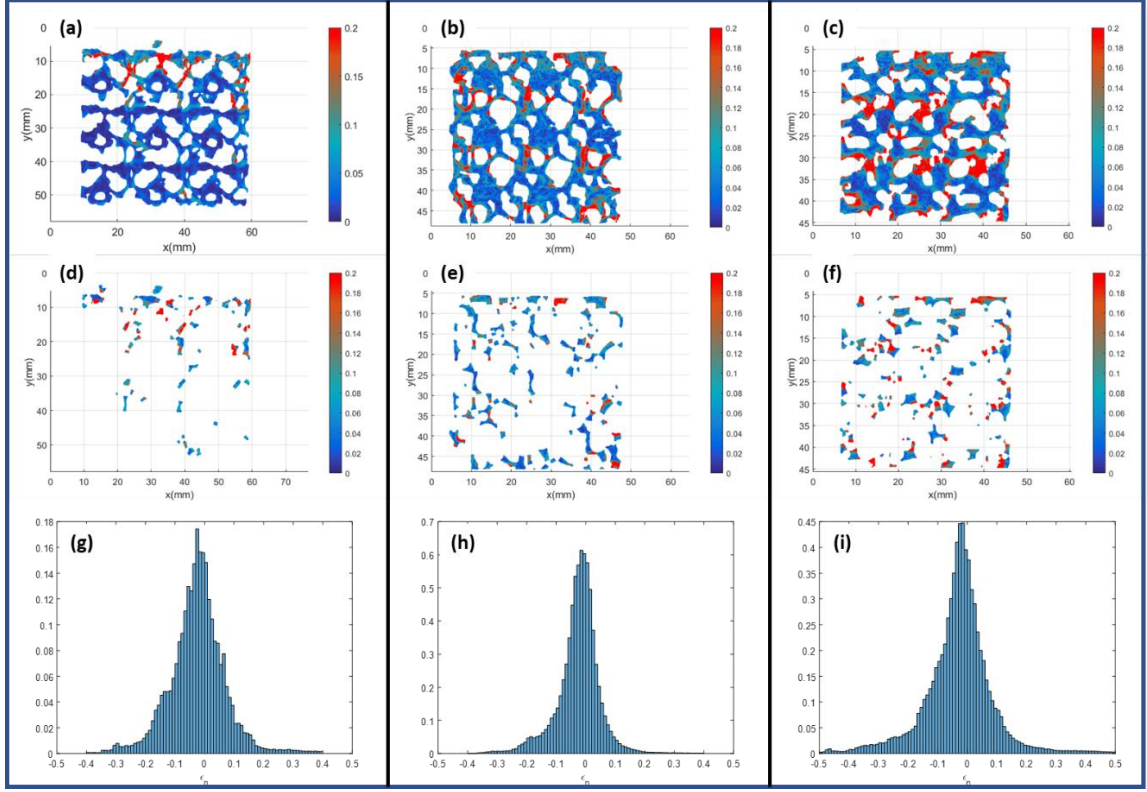
Figure 21: Isolated failure ligaments for MD-Based NP Pt structures (e-h) with normal strain distributions

These observations have several implications. The consistent bending dominated behavior for instance, suggest that despite increasing relative densities, the aspect ratio of the ligaments remain ideal for bending-driven failure. This leaves the junctions as the most likely medium by which significant density increase can be accommodated. In other words, a significant portion of the mass must be agglomerated in junctions.

A closer examination of Figure 18 supports this claim and demonstrates the implications. As is apparent from the figure, much of the strain is localized in high-strain regions, which are primarily associated with ligaments, and the fraction of these load bearing ligaments is comparatively small compared to the junctions. As a result, much of the failure is driven by the ligaments, but the junctions have minimal impact. Given this

observation and the relatively large nodes unique to the MD based solids, it is hypothesized that the nodes play a significant role in failure, altering the apparent density of MD structures but doing little to improve the overall strength. It is also conceivable that this junction role could factor into the modulus differences as well. Hence, given the established similarities in connectivity and ligament aspect ratios for both sets, it is reasonable to rule out other likely structural factors and infer that the enlarged junctions, characteristic of NP Pt based structures are the primary contributor to the structural differences. One could thus expect to eliminate the differences in scaling trends by properly accounting for the role of junction geometries. This is explored next.

2.4.4 Assessing the Unique Aspects of NP Pt Geometry

While establishing an accurate and robust means of properly accounting for the junctions is difficult, close approximations can be made using already developed expressions. For this, an earlier publication [36] is referenced which examines junction effect from an analytical perspective and develops expressions that relate the relative density and relative modulus of a foam with large junctions to one without. These relations follow Equations 7 and 8 respectively.

$$\frac{\rho_j^*}{\rho^*} = 1 + \frac{2(d/l)^2(t/l) + (2/3)(d/l)^3}{(t/l)^2 - (2/3)(t/l)^3} \tag{7}$$

$$\frac{E_j^*}{E^*} = \frac{(1/8)(t/l)^{-4}}{(t/l + d/l)^{-1} + 1/8(t/l)^{-4} - [(t/l)^3 + 3(t/l)^2(d/l) + 3(d/l)^2(t/l) + (d/l)^3](t/l)^{-4}} \tag{8}$$

45

The variables 't', 'd' and 'l' here are defined based on Figure 22, where the j-subscript associates a variable with a porous solid that has enlarged junctions.
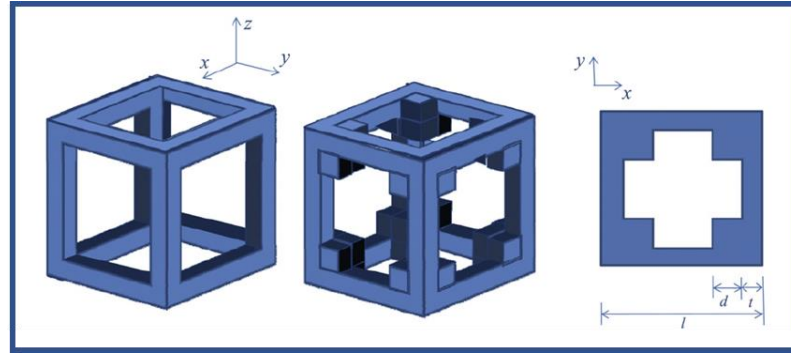
Figure 22: Schematic description of function variables [36]

Using the skeletonization algorithm to obtain the structural variables shown in Figure 22, and incorporating the measured density and modulus values from experiments, the expected density and modulus for a comparative porous solid without enlarged junctions can be extracted using Equations 7 and 8. Figure 23 shows the result of these calculations for the actual sample structure with large junctions, and the corrected equivalent in the absence of enlarged junctions. The result shows a much better correlation between the scalings of both structures, which although not exact, gives weight to the junction hypothesis.
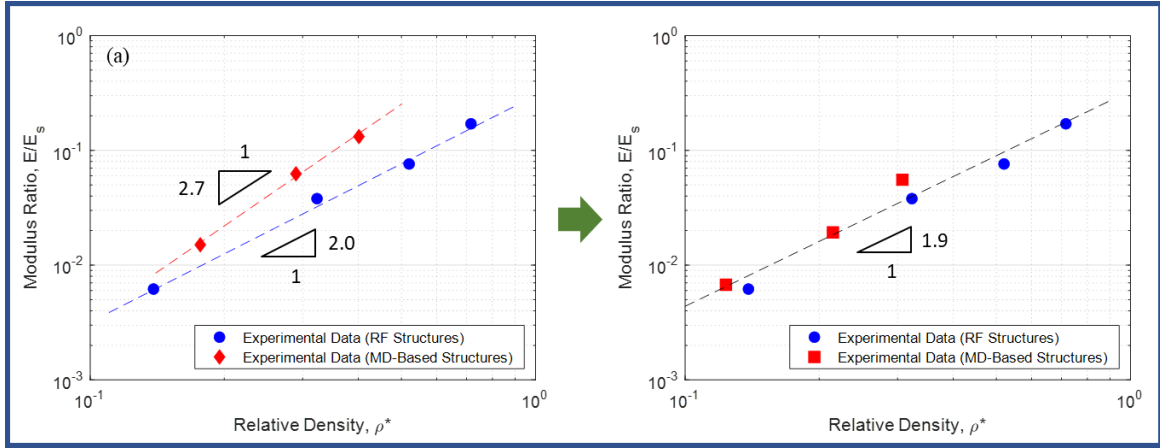
Figure 23: Original and adjusted relative modulus using outlined approach

While the source paper for equations 7 and 8 does not provide a similar expression for the strength, one may assume that strength differences in porous solids with or without large junctions are negligible. This is a logical assumption given that failure in cellular materials often follow a weakest-link mechanism, whereby the lowest load-bearing component, which is likely in the ligaments or a finite region of the junction-ligament interface (independent of junction size), often controls the failure of the entire structure. Hence, added junction mass should have limited impact on the overall strength given the features driving failure are unchanged. This logic is applied to the results shown in Figure 24, which use the adjusted density of Equation 7 to correct for relative strength.
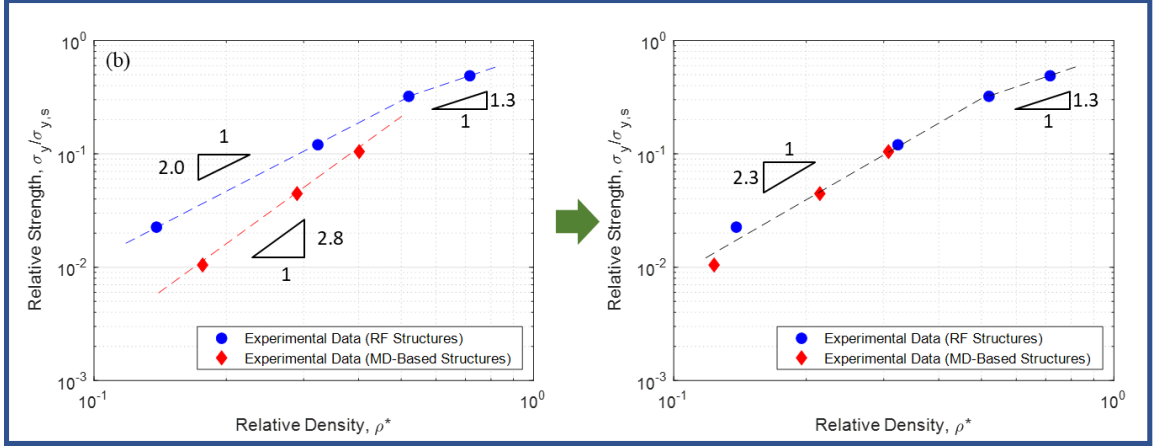
Figure 24: Original and adjusted relative strength using outlined correction approach

Figure 23 and Figure 24 show a clear improvement in the correlation between the 3D printed samples. The new combined fit for the adjusted modulus uses constants $C = 0.3$ and $n = 1.9$. The values for the strength, also segmented into two regions, follow fits of 1.5 and 0.76 respectively for C and $n = 2.3$ and 1.3. These results support the hypothesis that properly accounting for enlarged junctions could aid in proper characterization of NP metal mechanics.

2.5 Summary of Chapter Findings and Results

In this study, the effect of porous solid structure on mechanical response was studied by 3D printing porous solids and running mechanical tests accompanied by digital image correlation (DIC) to examine the mechanisms involved in mechanical deformation. Two sets of porous solids were explored: the first, the random (RF) porous solids, were created from a randomized lattice structure, while the second, the 3D printed MD porous solids, were created from molecular dynamics simulation of nanoporous porous solids. The latter explores the mechanical behavior of nanoporous solids by observing trends in

mechanical response independent of nanoscale effects, while the former explores the effect of density on the mechanics of a basic foam structure with consistent connectivity. The results, which are centered on data presented in Figure 8, provide details on the major factors that define the mechanics of porous solids. These results can be summarized as follows:

1. Both classes of porous media examined follow trends that deviate from the conventional octet and metal foam relative property fits.

2. NP Metals, independent of expected nanoscale effects, demonstrate unique mechanical properties (lower strength but higher stiffness within explored range) and increased sensitivity to density compared to a regular foam based on a disordered lattice.

3. RF structures, which were created from a disordered lattice structure to assess porous structures in an intermediate density regime, also exhibit a shift in behavior, with strength becoming even less sensitive to density changes beyond relative densities of ~0.5.

4. The structure specific behavior of the randomized RF structure can be explained using DIC analysis and serve as a foundation for exploring the mechanics of NP metals. In general, these behaviors are the result of an interplay between deformation localization, which is more prominent for lower density porous solids, and a shift from bending dominated deformation behavior to compression dominated behavior, culminating in a deformation behavior for highest density samples possibly analogous to that of a solid with holes.

5. Although the simulation-based NP Pt structures occupy a similar density regime, they respond differently from RF. It is inferred here that unique structural aspects of NP metals contribute at least in part to the complicated mechanics that drive this discrepancy. Specifically, mass accumulation in nodes appears to account for some of the discrepancies in modulus and strength trends between the MD-B and RF groups of samples.

6. In this chapter, a demonstrated approach to correcting for these junctions appear to effectively correct for scaling discrepancies for strength and modulus, supporting the junction hypothesis.

Much more can be said from the results obtained; however, these conclusions provide a sufficient context to describe the isolated contribution of geometry. The additional role of size effects must also be examined to gain full context on NP Pt behavior. This component is addressed in the next chapter.

CHAPTER 3.   SIZE EFFECTS ON THE MECHANICS OF NANOPOROUS PLATINUM

3.1   Introduction and Overview

This chapter tackles the size scale effects affecting NP metal modulus and strength as it depends on relative density. Specifically, it builds on the information presented in the previous chapter and examines the driving factors for altered mechanics in nanostructured nanoporous platinum with 5nm sized grains and ligament thickness. MD simulations play an even greater role here: Whereas the previous study on geometrical contributions employed the simulations to create a representative structure, simulations here are also used to obtain mechanical response information from an atomistic perspective. They also provide information on the nanoscale effects driving local mechanical response, which when compared to the detailed analysis of Chapter 2, could provide a clearer understanding of core mechanics. Actual experiments are also incorporated into this study to verify the reasonableness of simulation results. However, experiments are limited in the range of densities that can be developed.

The chapter is summarized as follows: Following this brief introduction, details on the experimental methods used are presented. These experiments consist of simulation and indentation work from which properties of NP Pt are extracted and used to fit scaling relations discussed in the introductory chapter. Following these experiments, the results are summarized in Section 3.3, followed by a discussion of the implications.

3.2   Study Methods

Given that this study aims to consolidate the relevant findings regarding the interplay of structure and geometry in the mechanics of NP Pt, the experimental portion of this study involves three primary elements: The first, which is related to the geometrical contribution, has already been explored in Chapter 2, but key findings will be revisited and compared to findings from the remaining elements, which are MD simulations and physical experiments on actual NP Pt. The methodology used is outlined below.

3.2.1   Simulation Methodology

Atomic structures of NP Pt of different relative densities are created and loaded under uniaxial compression using MD simulations. Interactions between Pt atoms are modeled via an embedded-atom-method (EAM) style interatomic potential [52]. MD simulations are performed in LAMMPS [46]. All atomic visualization were done in OVITO [47]. Structures have periodic boundaries in each direction. A MD timestep of 1 fs is used in all simulations.

3.2.1.1   Mechanical Test Simulation Process

The process used to create the original structures is the same as outlined in the previous chapter (see Section 2.2.1.1). Mechanical test simulations on the generated structures aimed to replicate atomic and nano-scale phenomena, as would be expected in actual NP Pt. These tests involved isothermal-isobaric loading at a constant strain rate of $10^8/s$. The resulting global pressure tensor of the system was used to calculate stress, while the engineering strain was calculated based on the deformation of the bounding box that

contained the simulation structure. The resulting stress-strain curves were processed for relevant properties, including moduli and strength. Localized mechanical behavior was also extracted from simulation results: The atomic strain tensor was approximated from the continuum strain field of the atoms, as defined by the change in the local neighborhood of each atom.

3.2.2   NP Pt synthesis, characterization, and testing

The NP Platinum used in this study were synthesized as follows: first, an amorphous platinum silicide alloy (Pt_xSi_{1-x}, $x = 0.1 - 0.35$) was deposited on a silicon substrate (100) using sputter deposition. The initial alloy deposition parameters were tuned to produce amorphous thin films with varying levels of residual compressive stress [33]. The alloy was subsequently electrochemically dealloyed in dilute hydrofluoric acid (3% in D.I. water) under an externally applied potential in the range 0.3 - 0.9 V [53]. Each NP Pt sample was examined with a Scanning Electron Microscope (SEM) under plan and tilt views. The resulting SEM images were used to obtain statistical information of the structure including relative density, junction size, ligament thickness and length using a method described in [33]. A select number of samples were examined using Transmission Electron Microscopy (TEM) [33, 53].

Mechanical testing of these NP Pt samples was done using nanoindentation or micropillar compression, following the principles outlined in Section 1.4. Berkovich nanoindentation was performed on all samples using an indenter with a tip radius of ~150 nm. The tip area function was calibrated right before any experiments were performed and was used to extract the reduced modulus, E_r and hardness, H using the procedure outlined

by Oliver and Pharr [24]. Specifically, the reduced modulus was obtained from the unloading portion of the indentation curve and the hardness was obtained by normalizing the maximum indentation force with the contact area. At least 20 indentation tests were performed on each sample at varying indent depths and the reduced modulus and hardness values were averaged over indent depths that are greater than the grain size (for nanocrystalline Pt) or cell size for NP Pt. Furthermore, to minimize substrate effects, indentation measurements beyond 30% of the film thickness were not included in the average calculation of hardness of reduced modulus. Nanoindentation modulus and hardness for NP Pt were reported in prior work [33, 36] but in this work we isolate samples that were also tested under micropillar compression.

In addition to the Berkovich indentation tests, a second set of experiments were performed on micro-pillars, created using an FEI Nova Nanolab focused ion beam (FIB) device. In this case, the pillars were milled prior to the dealloying process to avoid modification of the NP Pt structure by the FIB. Figure 25 illustrates notable aspects of the pillar generation process. Two primary considerations inform the milling process: First, a large enough clearance is necessary to allow for the indenter tip to compress the pillar uninterrupted. Second, given that the FIB milling is a time-consuming process that also creates damage under higher, accelerated milling currents, the milling procedure was performed in steps, producing successive trenches, ultimately leading to a free-standing pillar that was refined at the highest current setting over a smaller region.
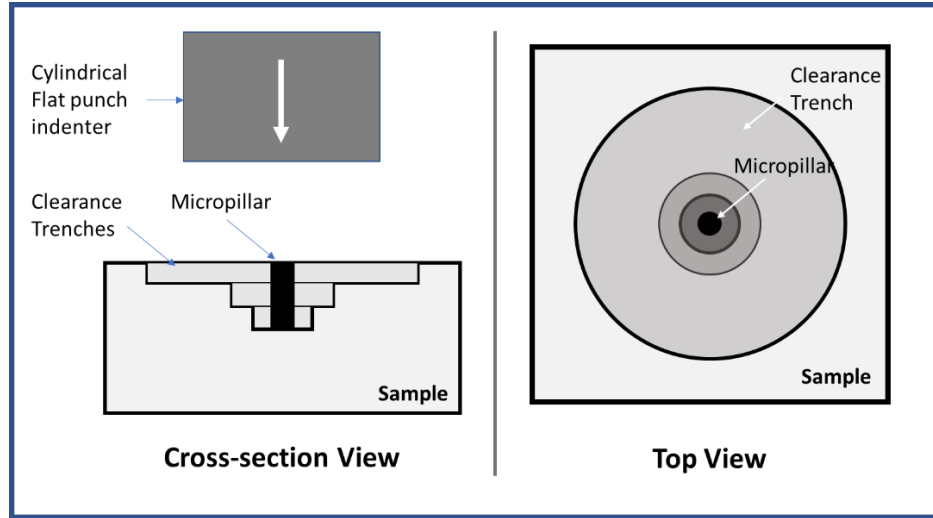
Figure 25: Schematic of pillar generation process for micropillar compression tests

Compression tests for the pillars were also performed using a Hysitron Triboindenter, but with a cylindrical flat punch tip, as illustrated in Figure 25. Figure 26 provides a physical context for the micropillar compression experiments. Figure 26(a) shows the top view of the final pillar, highlighting the larger clearance region created to ensure the indenter tip compresses just the pillar. The resulting pillars appear similar to Figure 26 (b) and (c), with a deformed version shown in Figure 26(d). The free-standing nature of the pillars meant that indentation results emulate conventional uniaxial compression tests, as shown in Figure 26(e). From such a curve, modulus and strength can be extracted using the familiar slope and 0.2% offset techniques. Recorded values were normalized using test results of dense nanocrystalline (NC) Pt with grain sizes of ~20nm.
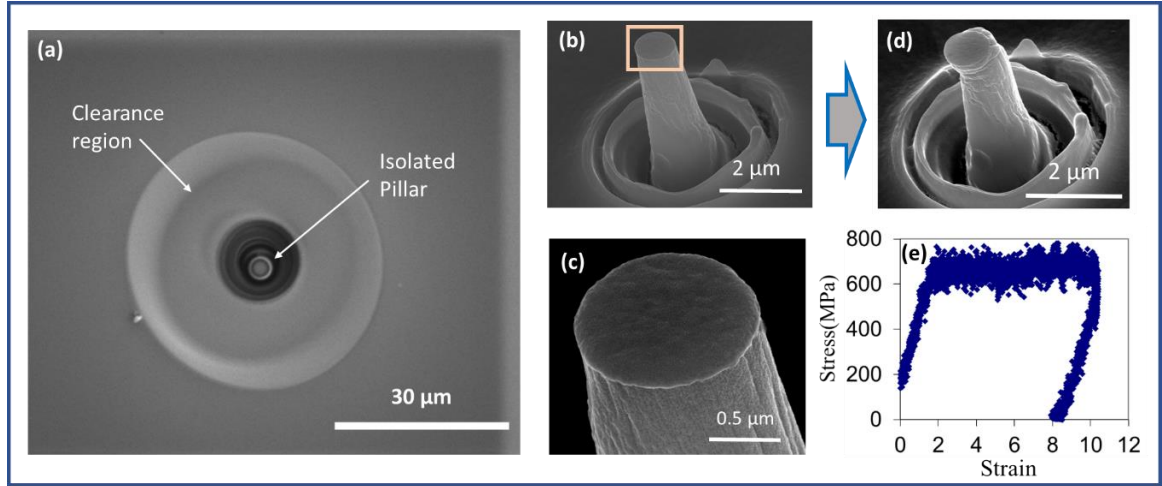
Figure 26: Summarizing elements of micropillar compression tests

3.3 Key Findings and Discussion

3.3.1 Structural Comparisons

The analysis of the results will begin with an assessment of the geometry to justify the overall approach. In line with the discussions of section 1.3 and in the absence of size effects, it is expected that given proper normalization of the properties explored (modulus and strength), the mechanics of the studied NP metals should primarily be driven by the nature of the structure. As a result, structures with identical geometry can be expected to display identical normalized behavior, regardless of size or material makeup. This is the logic applied to Equation 1, which is normalized by properties of an appropriate fully dense material, and it also implies that the scaled 3D-printed samples studied in Chapter 2 should behave identically to simulation and experimental NP Pt sets discussed here. It follows that any discrepancies observed can be attributed to size effects.

56

A simple visual comparison can qualitatively demonstrate that geometries of 3D-printed and MD simulation sets are identical to each other (see Figure 27(a) and (d)). However, to verify that these geometries are identical to actual NP Pt (shown in Figure 27(g)), the distributions of key structural parameters were compared (Figure 27(h-j)). These parameters, which are based on the connectivity and aspect ratio of features, are closely related to a structure's overall mechanical response and are thus an excellent quantitative tool for characterizing and comparing porous structures [18, 54]. More information on the skeletonization process is presented in Appendix B, including details of the results for the NP Pt sample.

The results from this comparison, as shown in Figure 27(h-j), clearly demonstrate that all three sets of data have very similar structural makeup, with the possible exception of the t/l statistics for the simulation set. This prominent tail is likely a consequence of the 3D skeletonization approach used for the simulation set, which differs from the 2D approach adopted for the 3D Printed MD-Based structures and the physical NP Pt. Note that the basic structure of the 3D printed sample is based on the simulation results, so that we can confirm the structures are similar and confidently assume that the highlighted discrepancy in the t/l measurements must be associated with the 3D technique. Nevertheless, the overall distribution appears to follow a similar shape, and the 3D printed and actual NP Pt sets, which are characterized using the same algorithm, show a strong enough similarity to establish confidence in the method.
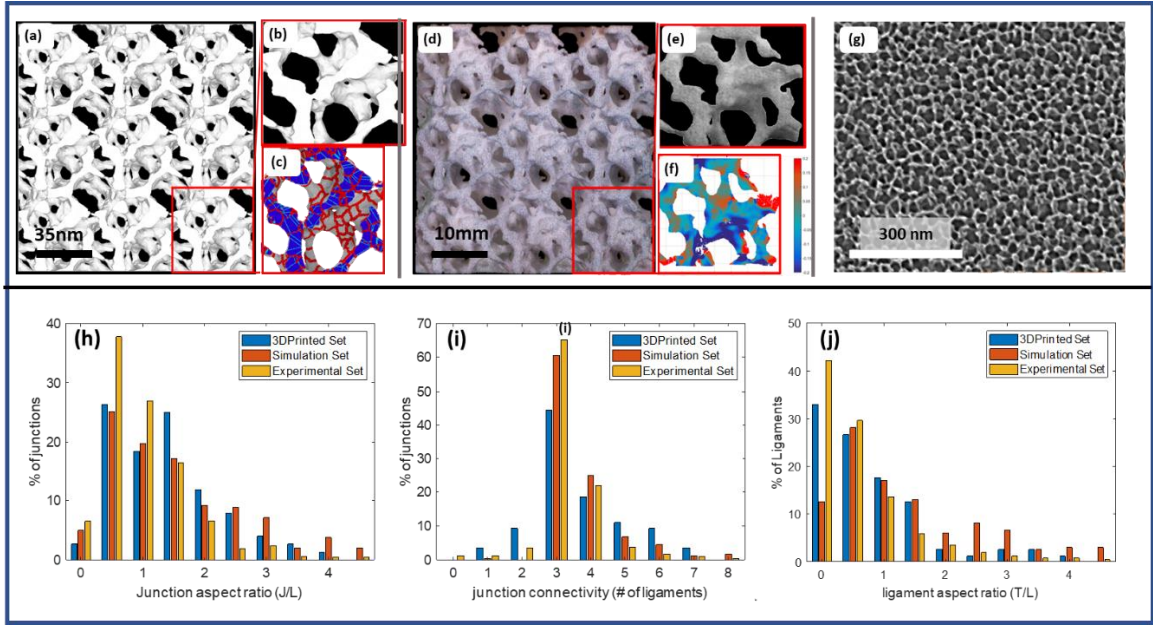
Figure 27: Comparison of the MD based structures and actual nanoporous metals

3.3.2 *Property scalings with relative density*

With structural similarity established, the three test sets can be compared using Equation 1 to fit the progression of relative properties with density. One of two outcomes can be expected from this fit: Either the 3D printed and simulation results yield identical fits, in which case one can conclude that any unusual trends observed for NP Pt are solely a result of its unique structure, or the fits are different, implying with certainty that nanoscale effects are relevant, and that geometry may or may not be an added factor. Note that in both cases, the experimental results of actual NP Pt are still expected to match reasonably well with MD simulation results confirming that simulations are an accurate predictor of the behavior. Figure 28 confirms this match, as experimental results match the order of magnitude predicted by simulations, but the results also show the latter expected outcome is clearly the case: Nanoscale effects are at play and geometry could potentially also be significant.
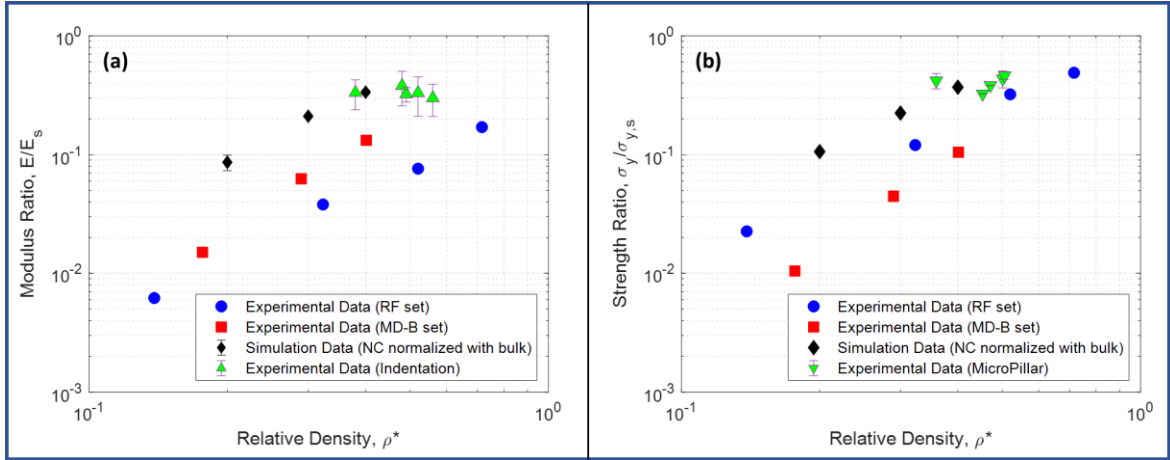
Figure 28: Property comparison of porous solids normalized with dense counterparts with simulation results included

Table 2: Summary of scaling fits for Figure 28 experimental data

	Relative Modulus Scalings			Relative Strength Scalings		
	RF-Set	MD-B Set	NC MD	RF-Set	MD-B Set	NC MD
C	0.3	1.6	2.1	1.2	1.4	1.9
n	1.97	2.67	1.98	2.01	2.82	1.8

The geometrical contribution has already been evaluated and confirmed in Chapter 2, but key findings will be summarized here to support the current discussion. Recall that one outcome of that study was the establishment of scaling behavior for NP Pt structures independent of nanoscale effects. Here, those findings are applied to assess the contribution of size effects alone.

Recall from CHAPTER 1 that the well-established Gibson-Ashby studies on cellular solids the expected scaling behavior for structures similar to those studied here.

Those structures, whose dominant ligament deformation mode is plastic hinge formation due to bending, show a typical scaling behavior of $E/E_s \propto (\rho^*)^2$ and $\sigma_y/\sigma_{y,s} \propto (\rho^*)^{1.5}$ for relative densities less than 15%, and additional modifications can be applied as necessary to extend such scalings up to 30% relative density. These scalings differ from those of NP Pt, based on the results in Figure 28 (table); however, given that some of these differences may be over-exaggerated by factors such as randomness and density limitations, the randomized RF structures examined prior were expected to serve as a more reasonable comparison, as they are most descriptive of a conventional porous solid with similar connectivity and relative density. In essence, these structures were representative to scalings of random porous solids in the intermediate relative density regime and established a definitive reference for comparison to 'classical' porous solid behavior.

The relative modulus scalings for the RF structures (blue data points) were similar to the classical G-A relationships but the normalized strength scalings have a more dominant dependence with relative density, similar to the work of Hakamada et. al. [55] obtained for porous solids formed by compacted copper powders in the similar density range.

Comparing the results of this RF structure to that of the scaled NP Pt structure (3D Printed MD-B) showed that the normalized modulus dependence (red squares of Figure 28) is a factor of 4 greater than the random lattice (blue circles) indicating unequivocally that the geometrical structure of the nanoporous solid has substantial variation from classical random lattices that contributes to enhancing the overall porous solid stiffness. On the other hand, the normalized strength for the 3D printed MD-B structures is a factor

of 2-3 lower than the random lattice indicating a weakened geometrical contribution of the geometrical structure on the properties of nanoporous solids.

Ultimately, simulations of actual NP Pt and geometrical replicas 3D printed to eliminate size effects have shown properties unique from each other and from conventional porous solid behavior (as predicted using the RF data set). This has led to the first set of conclusions, in line with the conclusions of Chapter 2: The above results altogether indicate that the NP metal geometry, unaffected by nanoscale effects, has a profound influence on the property scalings, giving at once a factor of 4 enhancement in the relative modulus and up to a factor of 3 decrease in the relative strength scalings with relative density (see Section 2.5 for me details on this conclusion). However, it is also apparent that size effects play an equally significant role in altering the mechanical behavior, as indicated by the dramatic enhancement (almost an order of magnitude) in both the relative modulus and strength of simulation based NP Pt, compared to their geometrical replicas.

3.4   Summary and Concluding Remarks

The combined findings of this chapter and Chapter 2 can be summarized as follows. The previous chapter's results demonstrate that the unique geometry of nanoporous metals contributes to their abnormal scaling behavior compared to the conventional porous solids depicted by the RF structures. This modification is further driven by two prominent nanoscale effects: surface effects but also additional nanoscale effects can lead to both an enhancement in ligament strength not easily captured by surface effect corrections.

CHAPTER 4.   PRACTICAL APPLICATIONS

4.1   Introduction

A primary benefit of understanding the dependence of mechanics on NP metal structure is the eventual ability to predict material properties based on the structure. The structure in turn can be controlled by the adopted synthesis techniques, leading to better control and prediction, as would be necessary for most practical applications. In this chapter, a study was conducted to demonstrate this potential for controlling properties via the synthesis technique. Here, a NP Cu system was adopted to allow for better synthesis control.

4.2   Dentin Inspired Nanoporous Copper

4.2.1   *Background and Motivation*

Biological materials have evolved over time to play highly specialized functions in nature. Recognizing this potential, scientists have often taken cues from nature that allow them to use unusual shortcuts that replicate the specialized nature of natural materials. These efforts are limited mainly by the complicated manufacturing techniques required to replicate nature's complexity, however, this study demonstrates that one such natural material, dentin, could be replicated using a nanoporous metal.

Dentin is a natural porous material found in teeth. Encased in enamel, the dentinal tissue [56] has a hierarchical structure with characteristic scale sizes spanning micro to nanoscales (see Figure 29). At the microscale, dentin consists of hollow cylinders called

tubules, which traverse the entire height of the dentin from the pulp to the enamel and are filled with a plasma-like fluid. The orientation, diameter and density of the tubules changes across the entire perimeter of the tooth [57]. At the nanoscale, dentin consists of collagen fibrils (CF) and hydroxyapatite crystals (HA) [57]. Dentin's mechanical properties, like other natural materials, range between those of dense metals and polymers, overlapping with NP metal properties. Dentin has relatively high fracture toughness ($1-3 \, MPa\sqrt{m}$) [58, 59] and moderate stiffness ($7-20 \, GPa$) [60] that strongly depends on tubule distribution and hydration. Dentin also possesses excellent fatigue life and has distinct and complementary properties compared to enamel, the exterior hard tissue of the tooth, so that cracks initiating from the brittle enamel surface may be arrested at the interface with dentin [52].
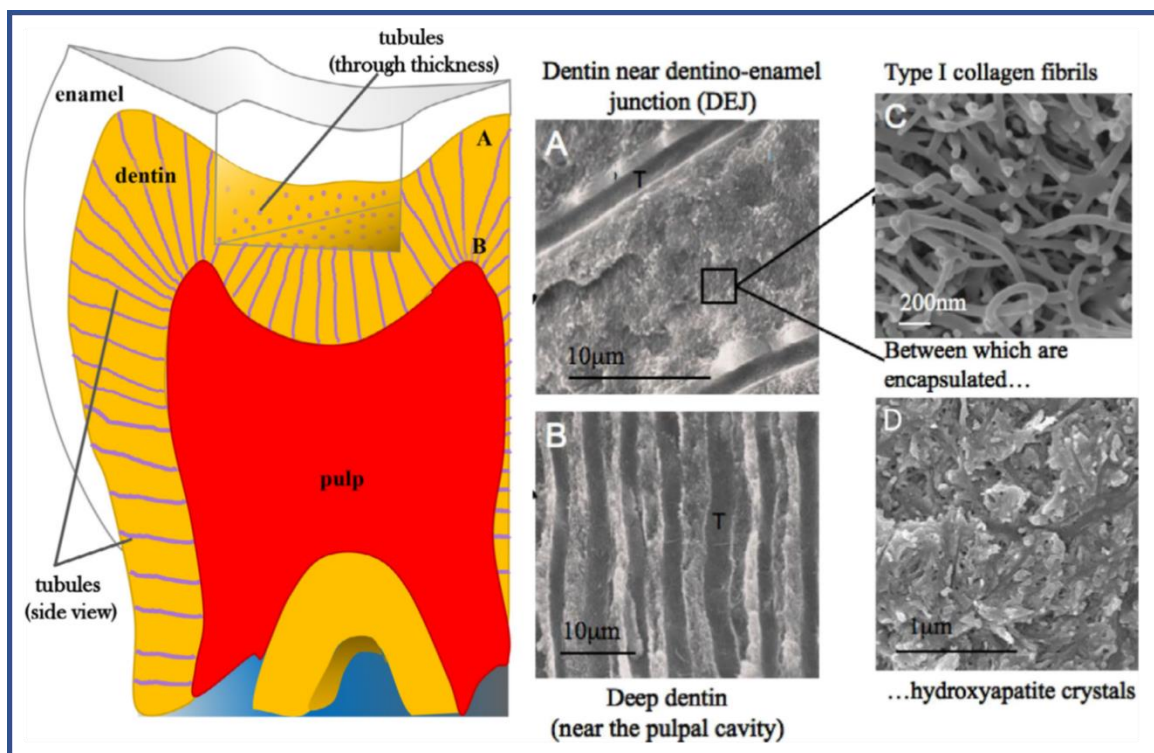
Figure 29: Schematic and SEM images depicting the main components of a tooth. SEM images show that tubules (T) closer to the enamel (A) are smaller in diameter and more sparsely distributed compared with tubules closer to the pulp (B). Dentin itself has a hierarchical structure consisting of (C) collagen fibers and (D) hydroxyapatite crystals.

The remarkable similarity in the nanoscale structure and mechanical properties between NP metals and dentin is the primary motivation for this study. This section will demonstrate that the nanoscale and microscale porosity of dentin can be replicated in NP metals, yielding a structure morphologically identical to dentin. Such structures are of great interest for several reasons. First, NP metals could potentially be used as part of tooth restoration treatments, or even as dentin analogs, to study infiltration of resins into dentin. Typical tooth restoration procedures require that dentin be demineralized and infiltrated with a resin composite. The hybrid layer at the interface between resin and healthy dentin is the main cause of failure of tooth restorations [61, 62] and the optimization of its

properties is highly desirable. At the same time, biological samples are unique, non-reproducible, environmentally sensitive, and require sophisticated testing protocols [63], leading to substantial uncertainty in the experiments. An "equivalent" system, such as NP Copper, with physical properties close to those of dentin that can be fabricated relatively easily and reproducibly, could help design adaptable resin-based tooth restorations thus having a significant impact on public health [64]. It is also notable that other NP metal systems e.g., NP Silver or NP Copper Oxide, possess antimicrobial properties [65, 66]. Incorporation of such oxide nanoparticles into dental resins has recently been suggested [67].

More generally, replicating dentin's hierarchical porosity may substantially aid liquid or gas reactant transport through the 3D structure of NP metals. The dentin porous network is naturally optimized for fluid and biological signal transmission through odontoblastic processes [68]. This natural optimization may inform the design of highly efficient 3D electrodes and catalysts [69], which could maintain mechanical integrity under cyclic thermomechanical loads, similarly to how dentin plays a key role in maintaining mechanical integrity of teeth under cyclic loads. In such applications, the key issue, irrespective of the type of fluid, is whether accessibility of active sites through the volume is possible.

4.2.2   *Experimental Methods*

4.2.2.1   Nanoporous Metal Preparation

The nanoporous metals used in this study follow the general development process outlined in Section 1.2 whereby the structures were controllably fabricated in a three-step

process involving synthesis of a precursor alloy that is then preferentially etched leaving a three-dimensional network of nanoporous metal. Using this process, both NP metal foils and bars can be fabricated. The precursor alloy type, the composition of the precursor, as well as the etchant type and the dealloying rate impact the eventual nanoporous metal structure [70-74], allowing for relatively varied structures, as will be discussed. More specifics are as discussed in the previous section. The resulting nanocrystalline NP metals [33, 75] that were synthesized originate from dealloying amorphous ribbons [33, 53, 75-78] .

Nanoporous Copper (NP Cu) here was fabricated after controlled etching of Copper Silicide amorphous alloy thin film. Two precursor alloys were used: $Cu_{0.25}Si_{0.75}$ and $Cu_{0.41}Si_{0.59}$ (atom%) as characterized by X-ray photoelectron spectroscopy (XPS). These were sputter deposited onto a silicon wafer under 100 V bias. The precursor alloys were etched in 3% HF in deionized water under an applied potential of $V = -0.3\ V$ with respect to a standard calomel electrode (SCE). The potential was applied for 100s, after which the samples were rinsed in deionized water and air-dried. The composition after dealloying, the residual stress state of the $Cu_{0.41}Si_{0.59}$ (atom%) precursor alloy and the presence of nanocrystallites within the ligaments are described in a prior publication [75]. Some of the NP Copper samples were exposed in the electrolyte up to 60 min to increase the thickness of the ligaments.

4.2.2.2   Imaging and Ion Milling

After etching, the samples were imaged using the FEI NovaNanolab 200 FIB/Scanning Electron Microscope (SEM), from which top views and through thickness

views were obtained. The SEM images were also used to obtain the film thickness, ligament dimensions and relative density (solid mass fraction) using ImageJ [79]. Dentin from a third molar was cut in a plane perpendicular to the tubules, in the coronal part of the tooth. The sectioned dentin was subsequently progressively polished up to a micron size finish using a 1 μm diamond suspension. The sample was then dehydrated by exposing it in an ethanol solution of increasing concentration and placed on a brass holder using silver paste to limit charging during imaging. The obtained sample was then imaged using an SEM (Helios 660, Zeiss) at 2 kV and 0.2 nA at a working distance of 2.3 mm using back-scattered electron imaging. Different magnifications of the tubules were obtained. Demineralized dentin was obtained by removal of the HA using a protocol described in Ref. [80]. The demineralized dentin was imaged in SEM using a similar protocol.

Tubules were also formed in some of the precursor alloy samples using a FEI NovaNanolab 200 FIB/SEM where a beam of Gallium ions is used to etch away features on the sample surface. As seen from the schematic of Figure 29 (a) and the SEM images of Figure 29 (b) the tubules have a circular cross-section perpendicular to the tooth perimeter; they are long elongated cylinders in the plane connecting the enamel and tooth root. The tubules created with the FIB on nanoporous copper reflect the exact pattern from the SEM images of the dentin sample. To achieve this, a mask was created by thresholding SEM images of dentin to capture the tubules' spacing and size. Using "xT microscope control", the user interface for the Nova 200 NanoLab-DualBeamTM-SEM/FIB, the tubules were etched on NP Copper to mimic the actual dentin tubule spacing and size. The ion beam milling was performed at 30 kV with a beam current of 0.5 nA.

4.2.2.3 Structural Characterization

The structure of the dentin samples (healthy and demineralized) as well as the NP Copper sample were compared by thresholding the SEM images using a triangle algorithm [81] implemented in ImageJ [79]. Any noise in the images was reduced using a median filter with a 10–16-pixel radius depending on magnification. The resulting binarized images for all samples were used to calculate a two-point correlation function defined using Equation 9, where I denotes the image intensity at location x , and $\langle ... \rangle$ denotes averaging over all locations x.

$$C(r) = \langle\, I\,(x\,)I\,(\,x\,+\,r\,)\rangle \tag{9}$$

The features in the images were isotropic in the statistical sense so the correlation function has only a dependence on the radial distance $r\,=\,|\,r\,|$ [82, 83]. The correlation function was calculated at two different magnifications to highlight the nanoscale structure of the dentin and NP Copper as well as the micron sized scale structure, with the presence of tubules.

4.2.2.4 Mechanical Characterization

Mechanical properties of NP copper were obtained using Berkovich nanoindentation [75]. For a small subset of samples, frustum indentation was also performed [84]. The samples used in the mechanical tests were synthesized under the same exact conditions as those with the fabricated FIB tubules. Berkovich nanoindentation with a ~150 μm sized tip was performed using a Hysitron nanoindenter. Tip area calibrations were performed using standard protocols: properties of known materials (e.g., aluminum)

were verified using the standard Oliver and Pharr method [85] prior to testing of NP Copper. For each sample, 25 indents 40μm apart were performed up to 2000μN. Measurements obtained with indentation depths higher than a single pore (> 30–50 nm) and smaller than 30% of the film thickness were averaged to obtain a single value for the hardness, H , where $H = F_{max} /A_{contact}$, is the peak indent force divided by the contact area. In addition, the reduced modulus, E_r, was obtained from the unloading indentation curve. The reduced modulus and hardness values were plotted as a function of ligament thickness for each sample. A 3-point moving average was calculated for the modulus and hardness measurements as a function of ligament thickness.

4.2.3   Results and Discussion

Scanning Electron Microscopy (SEM) images of healthy dentin tubules are shown in Figure 30(a) and (b). Figure 30(c) and (d) shows the tubule spacing and size as replicated in NP Copper using a Focused Ion Beam (FIB). The NP Copper sample has ∼35 nm sized ligament thickness and was obtained by controlled dealloying of $Cu_{0.41}Si_{0.59}$ (atom%) in Hydrofluoric acid (HF). The tubules were fabricated according to the protocol described in Section 4.2.2.2 and the SEM images were taken at the same magnification as the dentin images. As the figure shows, the exact same tubule arrangement can be easily replicated in the NP Copper sample. In appearance, NP Copper has open porosity similar to demineralized dentin. Healthy dentin on the other hand, consists of intermixed collagen and hydroxyapatite crystals (HA) [57, 86] (Figure 29).
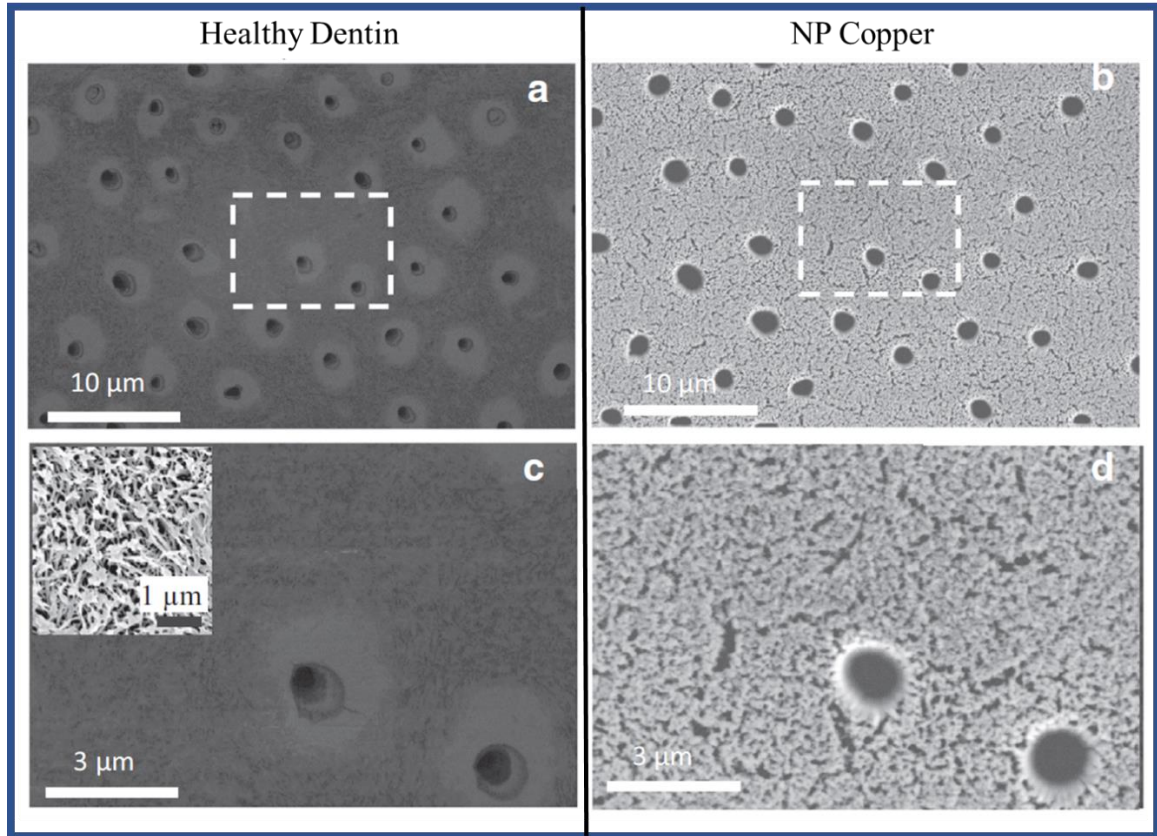
Figure 30: SEM plan view of (a) dentin tubules with (b) the corresponding tubule arrangement and spacing replicated in NP Copper. A close-up region around the tubules in (c) healthy dentin and the (d) replicated ones in NP Copper.

The correlation function is shown with radial distance in Figure 31(a) at the microscale and in Figure 31(b) at the nanoscale. The correlation function is obtained by thresholding the SEM images of Figure 30 for dentin (healthy and demineralized) and NP Copper. From Figure 31(a), the probability of finding identical features at the microscale decreases with increasing radial distance in the same manner for healthy dentin and NP Cu. This of course makes sense since the tubule network size and spacing in the dentin sample was designed and precisely replicated in the NP Cu sample.
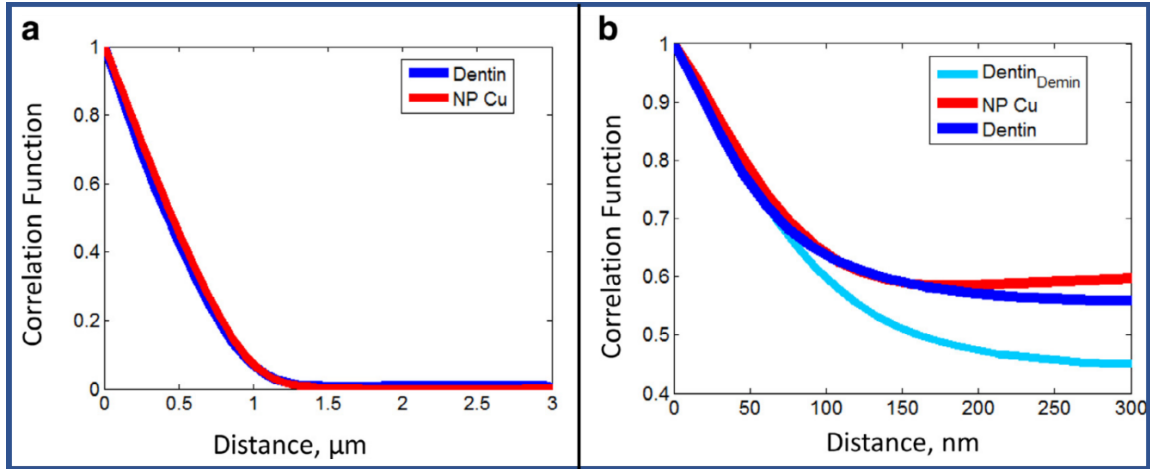
Figure 31: Two-point correlation functions of pores (a) at the micron scale and (b) at the nanoscale for both healthy dentin and NP Copper. The structure of demineralized dentin is also included in (b) the nanoscale.

Figure 31 (b) shows the dependence of the correlation function on the radial distance at the nanoscale for NP Copper, healthy and demineralized dentin. The correlation function for NP Copper decreases with radial distance and reaches a plateau that corresponds to the relative mass fraction of this NP Copper sample (~60%). The characteristic scale for NP Copper from Figure 31(b) is found to be 45.8 nm. The characteristic scale is defined as the radial distance at a correlation coefficient of ~0.8 which is between the plateau value (0.6) and peak (1). In a similar fashion the plateau for healthy dentin is found to be 56% and the characteristic scale is found to be 45.2 nm. The plateau for demineralized dentin, from thresholding Figure 30 (c), corresponds to a solid mass fraction of 46% and a characteristic scale of 60 nm. The dentin SEM images were obtained using backscattered electrons and have the advantage of being sensitive to the atomic mass. For instance, in healthy dentin made of collagen fibrils and hydroxyapatite (HA), the heavier HA crystals will appear brighter than the collagen fibrils. When healthy dentin images are thresholded, they can reveal the structure of the HA component. The

71

correlation function plateau corresponds to the relative area of the HA component (bright field) for healthy dentin. On the other hand, since the demineralization step etches out HA, the plateau for the demineralized dentin mostly corresponds to collagen. It should be noted that the etching process can cause shrinkage of the collagen network, which may slightly overestimate the collagen area fraction by a few percent [87]. From the plateau values of Figure 31 (b), the relative area of healthy and demineralized dentin are dual to each other since the former corresponds to the HA component area fraction and the latter to mainly collagen. The characteristic scale for demineralized dentin found from this analysis is ∼60 nm which is consistent with the characteristic scale of collagen measured from small-angle x-ray scattering [88].

Figure 32 shows the average hardness, H and the reduced modulus Er as functions of ligament thickness for NP Copper generated from two different initial alloy compositions, $Cu_{0.25}Si_{0.75}$, (black symbols) and $Cu_{0.41}Si_{0.59}$ (red symbols). The blue dotted lines on both inserts show the average healthy dentin modulus with Figure 32(a) showing the modulus variation depending on location and hydration level [60, 89] in light blue. For demineralized dentin, the modulus is in the range of 0.2−7GPa, depending on hydration level [60, 90]. The hardness of demineralized dentin (cyan dotted line) is also shown in Figure 32(b) [60, 89]. NP Copper in the range of 30−50nm from $Cu_{0.25}Si_{0.75}$ has closer values to healthy dentin, but it is possible to fabricate samples with features more similar to demineralized dentin.
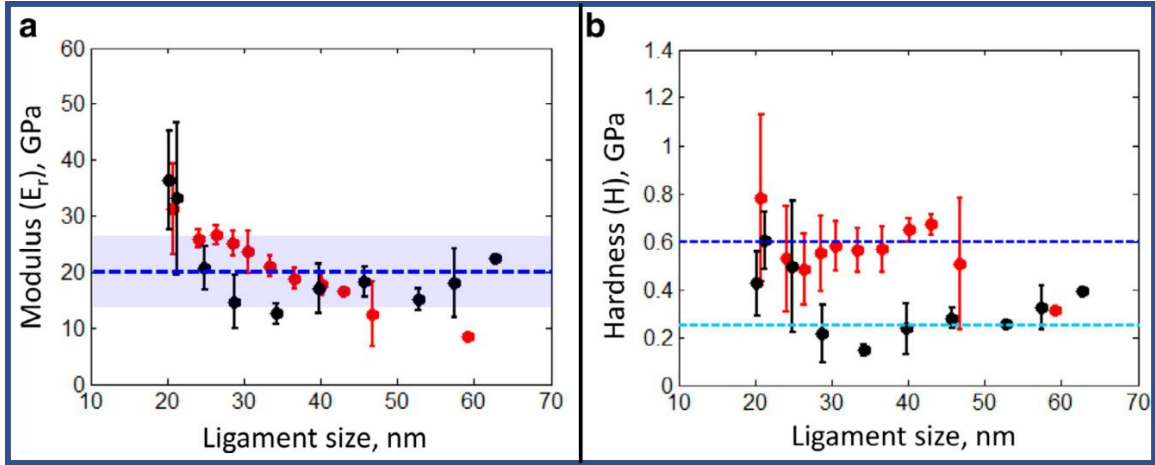
Figure 32: (a) Reduced modulus and (b) Hardness as a function of NP Copper ligament size, as assessed from Berkovich nanoindentation.

Other physical properties of NP Copper also have an overlap with dentin and are summarized in Table 1. For example, the plastic Poisson's ratio, a measure of lateral dimensional changes in a material beyond yielding, is a crucial parameter when describing the pressure sensitivity of the yield surface of a porous medium [91].

Table 3: Comparison of feature sizes and mechanical properties of dentin (healthy and demineralized) and NP Copper

Geometrical and Mechanical Properties	Dentin (D)	Demineralized dentin (DD)	NP Copper
Total porosity (%)	1–10 [56, 69, 92]	70–90 [71]	40–60% (tunable)
Average ligament size (nm)	5–50 (HA platelet size)	~100 (collagen fibril diameter)	18–80 (tunable)
Second order pore size (nm)	-	~100 [56]	30–100
First order pore size (tubule diameter) (µm)	1 (varies with location)	3 (corresponds to enlarged tubules and varies with location)	Can be fabricated with various techniques
Young's Modulus, E (GPa)	18–30 [92] ~20 (ITD) ~30 (PTD)	0.25 [59, 74] - -	10–50 (tunable)
Plastic Poisson Ratio, ν^P	0.3	-	0.2–0.3 [79]

Dense solids have a plastic Poisson's ratio of 0.5; low density porous media have a plastic Poisson's ratio of ~0. The plastic Poisson's ratio of dentin was measured to be ~0.3 [89]. NP metals have been reported to have a plastic Poisson's ratio of 0.2–0.3 [84, 93]. The design of NP metals with nanoscale structure and mechanical properties similar to dentin, may allow for calibration of numerical models formulated to examine the mechanical response of dentin. For example, dentin stiffness models based on the homogenization scheme of Hashin [94], in which the volume distribution of peri–tubular dentin around the tubules, that is stiffer than inter-tubular dentin that is away from the tubules, is assigned a non-uniform distribution, determined from image analysis [95], may

benefit from additional information coming from the mechanical response of NP Copper with FIB generated tubules.

4.2.4   *Summarizing remarks*

In summary, NP Copper was engineered to have similar Young's modulus, hardness, and plastic Poisson's ratio with dentin. Imparting the microscale tubule network on NP Copper via micro/ nanofabrication methods in a controllable and repeatable fashion may make NP Copper an ideal model system to study properties of dentin infiltration with resin composites, which in turn may enable numerical model calibration and advance resin-based tooth restoration. Intriguingly, fabricating NP metals with a hierarchical porosity inspired by dentin may provide a path towards stable 3D catalysts with enhanced bimodal porosity, enabling enhanced transport of the reactant fluid through the structure. This may help overcome the well-known limitation that the interior surface area of NP metals is not readily accessible for traditional structures [96]. While there are several proposed methods for introducing a bimodal porosity for catalysis applications [97, 98] including fractal inspired structures [92], dentin-inspired bimodal porosity may help maintain mechanical properties while enhancing transport.

CHAPTER 5.   SCIENTIFIC CONTRIBUTIONS AND FUTURE DIRECTIONS

This chapter will discuss key implications of this work, as well as the areas of study that can be explored by building, in part or in whole, on the work presented herein. Relevant scientific contributions are discussed first, with subsections detailing specific areas of contribution. This is followed by a discussion of future work, as it relates to the research work conducted in this thesis. The chapter concludes with a brief discussion of broader impacts that could come from this work.

5.1   Scientific contributions of this work

5.1.1   Novel methodology

This work uses a combined experimental and numerical approach that is novel and can be applied to future systems. Additive manufacturing as a tool allows for the generation of complex structures and could be used to replicate the complex nature of porous structures in general. In the context of this work, the method has also been shown to effectively capture key geometry of complex structures. Strain mapping, another tool that could be adopted in other experimental studies, complements this additive manufacturing tool, allowing researchers to obtain more detailed information. This work has shown the effectiveness and potential of strain mapping via digital correlation to obtain significant level of mechanics detail from physical experiments. In particular, we note the separation of the maximum in-plane strains to identify dominant deformation mechanisms in the structures. These strain maps and their accompanying statistics could prove essential in

identifying mechanisms in stochastic materials. Ultimately, these two elements, when combined in the manner demonstrated in this work, can be applied to identify mechanisms in other systems, discover new systems, and much more. In the specific context shown here, it can also be used in answering many of the elusive questions associated with complex nanoscale structures. This approach demonstrated the ability to identify nanoscale geometrical mechanisms in the absence of size effects and can be used in the study of other nanostructured systems and alloys. The possibility of 3D printing different materials and varying their density can also open the parameter space for replicating some of the favorable nanostructural attributes to the macroscale.

This work also demonstrates the effectiveness of MD simulations in these efforts, specifically in developing a structure that replicates nanoscale experimental structures and testing these structures with the relevant size effects at play. Furthermore, although not shown here, these MD simulations can be used to perform closer examinations of local effects and mechanisms, providing information analogous to the detailed data from strain mapping on additive manufactured samples. Particularly notable is the fact that this work demonstrated that MD simulations can be used to quantitatively assess the overall behavior of the material with results that are in good agreement with experimentally obtained measurements. This opens the possibility of using MD and nanoscale experiments to provide side-by-side quantitative evaluations.

5.1.2   Key contribution to the field of nanocrystalline nanoporous metals

At the most focused level, this work has helped to demystify the complexities associated with identifying the effect of geometrical structure on the mechanical properties

77

of nanocrystalline nanoporous metals. Specifically, as summarized in previous chapters, we demonstrate the complex contribution of geometry and size effects, clarifying the specifics and nature of the geometrical contribution while also highlighting key considerations and contributors to porous solid mechanics at the nanoscale. This is the first time these size effects, separated from geometry, have been demonstrated and a clear distinction between origins of the mechanical behavior of nanograined vs. single crystalline NP metals is shown. It is hoped that this work will inform more accurate models for nanoporous metals that could accelerate the design and incorporation of these nanoporous metals into tangible designs. For instance, the relevance of the relative density as a tool for characterizing the geometry relationship to mechanical properties has been emphasized. It is clearly demonstrated that corrections must be made to improve its effectiveness.

From a fabrication perspective, this work could aid efforts to increase the versatility of design and mechanics through synthesis protocols. Numerous compositions and development paths exist for nanoporous metals, and a solid theoretical understanding already exists regarding the nature of structural evolution under processing conditions. Coupling this information with the context provided here could inform the direction of efforts and minimize the number of experiments/simulations required to develop a comprehensive picture for the relationship between fabrication protocol and mechanical properties. For instance, some effort has been put into coarsening as a tool of altering/improving the mechanical properties of a structure [16, 99, 100]. However, given the nature of evolution of a nanoporous structure, which often leads to mass accumulation in the junctions, this could have the negative effect of compromising material property based on the Chapter 2 discussion on geometry impacts. Such considerations minimize

design iterations and provides clarity to researchers regarding the most logical directions for improvement.

5.1.3 Broader contributions

On a wider scale, as it relates to the study of porous solids, this work has helped clarify the nature of modulus and yield strength dependence on relative density at an intermediate density regime (up to ~70%), specifically for the generic geometry captured by the RF structures. Furthermore, it provides a context for the nature of this dependence as it relates to the key deformation modes involved. Such information could inform design and applications involving higher density porous solid designs, which although uncommon given the prevalent drive for weight minimization, still need to be understood for when applications arise. This is the first demonstration of how the deformation mechanisms in the ligaments changes from bending to stretch dominated behavior as a function of density whilst connectivity remains the same.

In addition, from an application perspective, the dentin-related example provided helps demonstrate the versatility and relevance of this work as it relates to the push for bio-inspired applications. Given that porous materials in general have much potential in biomimetic applications, one could expect that the context provided here could also be expanded to other forms of porous mediums in bio-inspired design. Ultimately, a key hope and anticipated outcome is that this work encourages a closer examination of nanoporous metals as an effective candidate to satisfy a wide range of material needs. Here, demonstration and clarification of fundamental behaviors have been leveraged as the key tools to accomplish this. And while the primary objectives have been addressed, there is

much more than can be done towards this overarching goal. Some considerations for next steps are discussed next.

5.2   Future work

5.2.1   Assessing other material properties

The modulus and strength have been the priority of this thesis; however, the underlying results from various tests, including strain mapping distributions and simulation results, possess much more information pending interpretation. Key information on the post-yield behavior for instance warrants more exploration and can be examined with techniques and methods already used. As explained in Section 3.2.1, the MD simulations have been carefully set up to capture invaluable atomistic information including strain accommodation, localized strain concentrations, and much more. Such information can be expanded to beyond the yield point to track the evolution of plasticity inducing defects in the context of nanoporous metals.

Similarly, the potential of 3D printing coupled with strain maps has already been demonstrated, the information needs only be interpreted further to uncover additional details. Other mechanical effects such as the possible mixed-mode loading behavior in ligaments or likely shear in junctions and how this affects properties such as the plastic Poisson ratio can be further explored.

In addition to mechanical properties, work can also be done on other material properties such as thermal or electrical. Given that most modern application require materials that satisfy multiple functionalities, it may prove beneficial to understand what

complementing benefits nanoporous metals may possess beyond their specific mechanics. This could mean exploring scattering effect of surfaces on nanoporous metal conductivity, or perhaps assessing the ease of diffusion through the porous network. Such work will likely be unique to required applications so developing new potential applications to motivate the efforts could be the first step.

5.2.2   New systems

This path needs not be limited to the structures discussed here, such an expanded study can be conducted for other NP metal systems. It is reasonable to expect that most of the findings discussed, as well as future findings for this system, are also applicable to other nanoporous metals, however such claims can be verified using comparable studies conducted on other systems. These comparative studies can answer important questions regarding the versatility of presented findings. For instance, the impact of the grain size and average ligament thickness likely changes as the size of the features change. The conclusions of this thesis may therefore be inapplicable to these systems, but details on which kinds of systems do qualify remain elusive. Eventually, a clear distinction between general nanoporous metal behavior and system exclusive mechanisms is desirable.

In addition, it could be useful, with the context of the results presented, to explore other design approaches for nanoporous metals, specifically those that eliminate some of the most prominent mechanics contributors (enlarged junctions for instance). Perhaps, by leveraging the information provided here, potential limitations could be reserved and optimal systems for future applications can be developed.

5.3 Expanding experimental applications

5.3.1 Improving fabrication control

One future endeavor, from a fabrication point of view, is to establish greater control on the properties. The importance of structure has already been emphasized here and the experiments on NP Cu demonstrate the possibility of leveraging this quality. However, such structural versatility and the resulting property flexibility has not been fully perfected. Systematic studies relating the synthesis approach and the resulting structures have already been explored (e.g., [12, 53, 101, 102]), but these must be expanded to extend the working range of nanoporous metals. Such work would likely be in parallel with the earlier suggestion for expanding the applicability of this thesis' techniques.

One approach that could potentially accelerate this effort would be to characterize the effects of coarsening. Several studies have already shown that post-dealloying treatment of nanoporous metals could lead to altered structures and densities (see for instance [17, 99]). Details on the nature of this evolution are not fully understood, but such information could prove invaluable in developing novel applications.

5.3.2 Exploring novel applications

Exhaustive information on fabrication techniques and property implications would be irrelevant if no tangible implementations exist. The dentin application demonstrated in Chapter 4 highlights the possibility for unconventional implementations of nanoporous metals, the innovation in this regard is limited only by the creativity and level of understanding of the material capabilities. Numerous potential applications have already

been suggested, but with some of these come the added challenge of streamlining fabrication or incorporating the nanoporous metals in a reliable manner. These explorations can take advantage of the information presented herein to better predict expected mechanics, but some questions will likely be unique to the specific application and will require unique studies.

APPENDIX A. PARAMETRIC STUDY ON NC NP PT

MECHANICAL BEHAVIOR

A.1   Overview

A parametric study that uses simple FEA simulations to examine the junction contribution phenomenon referenced in Chapter 3 is presented below. The primary motivation for this study was to better understand the source of enhancement in NC NP Pt by considering the combined role of size effects and inhomogeneity. The approach builds on the knowledge that for porous structures, properties like modulus and strength are directly affected by the bending stiffness and strength of individual ligaments since they experience the most deformation. It follows that observed modifications in overall properties independent of geometrical modifications must be a result of changes in these ligament mechanics; however, it is also possible that changes in properties of both joints and ligaments could affect overall mechanics.

Such modifications likely do not result from homogenous enhancement in properties: A commensurate change in the properties of both the junctions and the ligaments should not affect effective properties since the normalization should adjust for this material effects. However, if either the ligaments or joints have experienced isolated property changes, their interactions could be altered, modifying overall properties. This is a possibility given that size effects may affect nodes and ligaments differently due to their size differences. Normalizations will not capture this since they assume properties are homogenous throughout the entire structure. In this study, the most obvious sources of

inhomogeneity in these nanoscale structures are examined in a simplified and systematic manner.

A.2   Test structure and key objectives

The configuration for the structure used in this study is shown in the Figure 33 below:
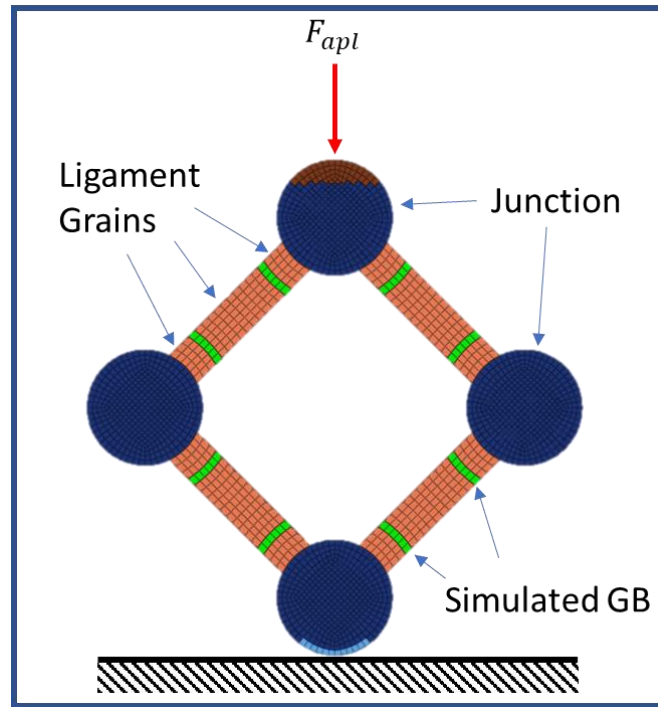
Figure 33: Setup for parametric study showing key features and load

The key benefit of this structure, compared to classical models used in similar studies, is the representation of orientation and inhomogeneities. In line with the original objective of observing the effect of inhomogeneities, the structure was designed to capture the inhomogeneities that come not only from differences in properties of junctions versus ligaments, but also from grain boundaries present within the ligaments. The structure also factors in orientation, which is essential since rather than the simplified bending behavior,

ligaments are more likely to experience a mixed mode loading that could affect how they deform. Once again, the guiding hypothesis claims that enhancement of one or more subcomponents of the structure is causing an overall enhancement to the entire structure. Thus, tests conducted will address two primary questions with a focus on the effect on modulus:

1. How does the presence of grain boundaries affect typical bending modes and overall stiffness?

2. What additional effect do the properties of these components have on overall stiffness?

To answer these questions and minimize the number of simulations necessary to arrive at a coherent solution, the moduli were parameterized following the Table 4 below.

Table 4: Overview of property ratios for study

$Er = 104800$ Case	All units in MPa					
	El	Ej	Egb	El/Er	Ej/Er	Egb/Er
1	104800	1048	104800	1	0.01	1
2	104800	10480	104800	1	0.1	1
3	104800	104800	104800	1	1	1
4	104800	1048000	104800	1	10	1
5	104800	10480000	104800	1	100	1
6	1048	104800	104800	0.01	1	1
7	10480	104800	104800	0.1	1	1
8	104800	104800	104800	1	1	1
9	1048000	104800	104800	10	1	1
10	10480000	104800	104800	100	1	1
11	104800	104800	1048	1	1	0.01
12	104800	104800	10480	1	1	0.1
13	104800	104800	104800	1	1	1
14	104800	104800	1048000	1	1	10
15	104800	104800	10480000	1	1	100

The set explores the effect on modulus for three separate components: the junction (Ej), ligament (El) and simulated grain boundary (Egb). Each value is normalized based on a modulus Er, the value of which is based on the dense property definition of NC Pt. This provides an estimate for the order of enhancement a component will need to experience, relative to what is known, for it to show the observed level of enhancement. For each component, the ratio of its property to that of the reference is varied by orders of magnitude while keeping other properties constant and equal to the reference. The result is three sets of 5 cases for a total of 15 cases. Also observe that for each set, a condition of homogeneity exists where all properties are equal. This case serves as a control condition.

A.3   Summary of Results

The results of the study are summarized in Figure 34 below where Ex represents the feature modulus in question, as indicated by the legend. The message from this figure is clear: as far as enhancement goes, the modulus of junctions or grain boundaries, as the features are demonstrated in Figure 33, have negligible effect on the overall relative stiffness. This implies that given the established constraints, modulus enhancement in a structure could potentially be the result of an enhancement in the ligaments, regardless of enhancement in other features. The figure also shows that lowering the stiffness of any feature in a structure will undoubtedly lead to a reduction in overall properties, unless if an offsetting factor counteracts the effect.
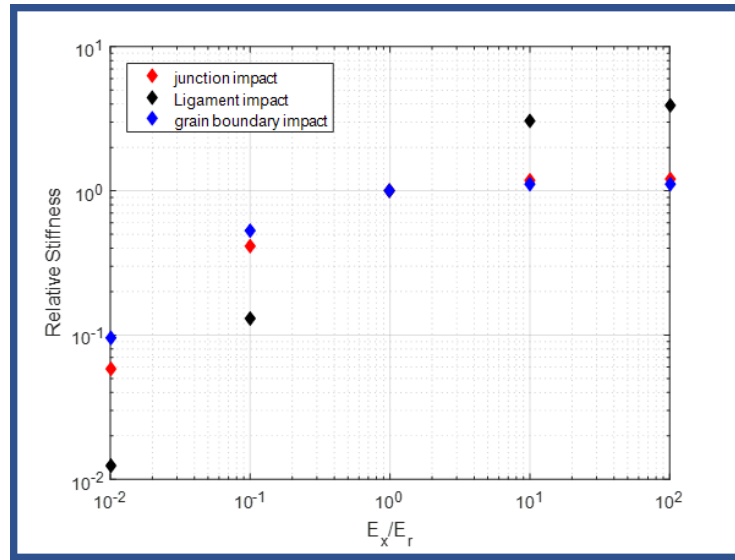
Figure 34: Summary of study showing effects of property change on overall relative stiffness

At this stage, these results only provide a conceptual view of a likely scenario where modulus enhancement may occur; however, to verify with certainty that this scenario is

most critical, a logical means of identifying the phenomenon in actual simulations is necessary. To address this, several considerations must be made. First, it is already apparent that the introduction of crystallinity likely reduces the properties of any material since they compromise the atomic lattice integrity and serve as defects where deformation can localize. Therefore, for a NC porous structure compared to a SC alternative, one would expect the NC version to be weaker. On the contrary, an enhancement is observed. In addition, while other nanoscale effects could very well be the source, each of these factors can be expected to have the overarching effect of either enhancing a portion of the structure or all of it. The former is ruled out since it is not observed in dense control tests, the latter is precisely what is addressed here.

A.4   Interpreting Findings and Expanding to Experiments

A follow-up test proposed uses an approach involving the strain accommodation for individual features. This process, which captures the fraction of the total strain experienced by individual members, can be readily applied to the robust simulation experiments, and potentially capture uneven property distributions. Here, the viability of the approach is examined by applying it to the results of the parametric study and identifying any correlations.

For the test, three cases of interest were selected: Cases 6, 8, and 10 from Table 4. The sixth and tenth case explore the situation where overall properties change due to ligament change alone, while case 8 is a control case that examines the homogeneous case. The resulting strain accommodation within the linear-elastic regime is shown in Figure 35. It is clear from this figure that when the stiffness of the ligament is much lower than other

regions, the deformation of the ligaments account for almost all the structural strain. This behavior transitions as the properties shift and in the single property case, ligaments still represent most of the strain but there is a more prominent role of junctions. Ultimately, at the stiffest ligament scenario, minimal deformation occurs in the ligaments while the junction and grain boundary accounts for most of the deformation.
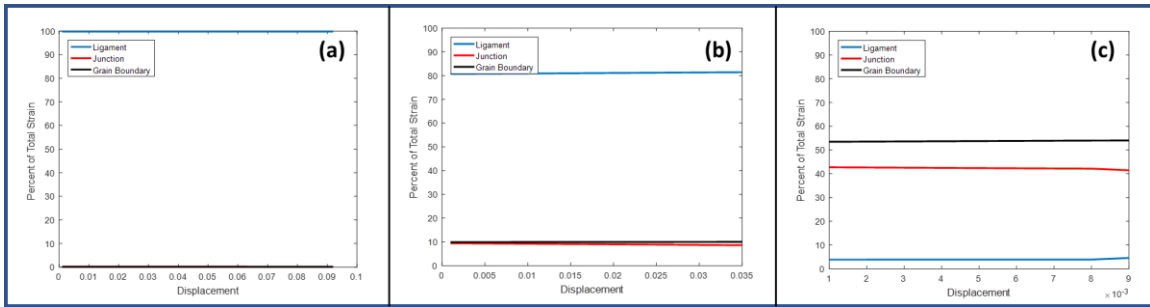
Figure 35: Junction accommodation for (a) Case 6, (b) Case 8, and (c) Case 10

This observation can be summarized by superimposing results on Figure 34 (shown again in Figure 36a). To do this, the fraction of the strain accommodated in the junctions was normalize using the strain accommodated in junctions of the control case. Figure 36b showed this superimposed result and clearly demonstrates the strong correlation between the junction accommodation and relative stiffness of junctions compared to ligaments and other features.
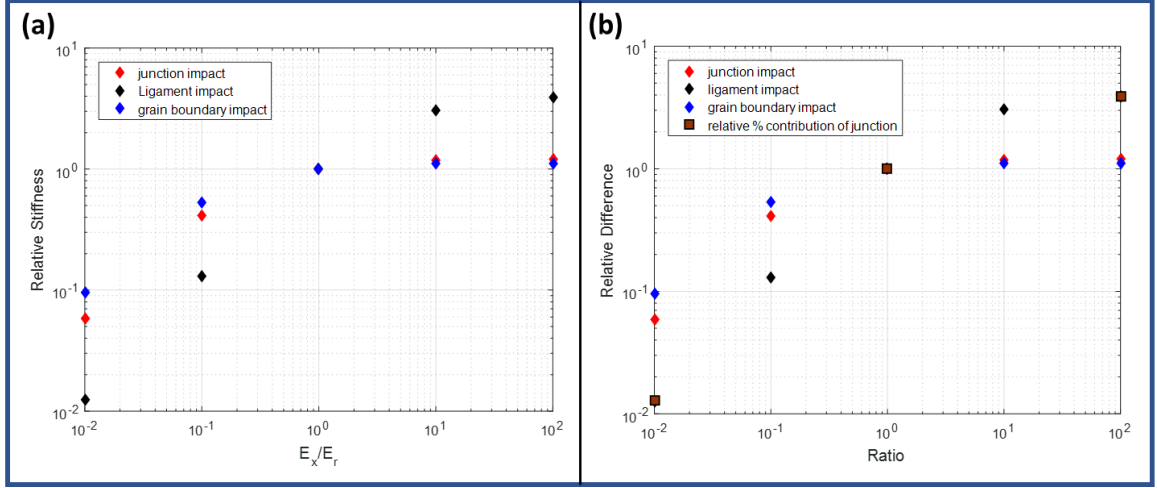
Figure 36: Comparison between property inhomogeneity impact on relative stiffness versus relative junction strain accommodation

A.5 Summary and Conclusions

In conclusion, this simple study suggests that the uncaptured source of structural enhancement despite proper normalizations may be tied to enhanced properties of the ligaments. Furthermore, this phenomenon can be captured by comparing the region (ligament or junction) specific strain accommodation for the NC structure to that of the SC structure. Increased accommodation in junctions is thus a likely indicator of unusually enhanced ligament stiffness.

Further study would be necessary to draw even more defining conclusions, especially as they relate to the strength of the structure. However, several reasonable conclusions are apparent from the study so far:

1.   The stiffness of ligaments is far more relevant in predicting structural enhancement than junctions, even though junctions play a significant role.

2.   It is possible to assess if enhancement in ligament stiffness compared to junctions by measuring the strain accommodation in the junctions.

APPENDIX B. SKELETONIZATION ANALYSIS FOR FEATURE

ASPECT RATIOS

B.1 Introduction

B.1.1 Overview

Structure property relationships for low density porous solids employed dimensional analysis to isolate behavior of individual components and relate it to the overall behavior of the porous solid. In the case of mechanical response, the deformation of unconnected ligaments (ligaments as defined in Figure 7) was identified as the key feature controlling overall behavior. Therefore, much of the classical literature relies on identifying metrics for these unconnected ligaments (e.g. their aspect ratio, connectivity, etc.). While this may be an easy task for ordered, low density porous solids, it is not as trivial in more stochastic or high solid mass fraction porous solids. In the current work, an automated process was developed using image registration algorithms to address this need. This Appendix chapter provides some clarification for the approach by outlining key details and considerations associated with the method as it has been adopted in this work. The key results of the approach are presented in Chapters 2 and 3.

B.1.2 Motivation and Limitations in Current Techniques

Studies of nanoporous metals that have required an understanding of underlying structure basic feature dimensions and size have adopted a range of approaches to obtain relevant information. For instance, in the study outlined in Chapter 4, a correlation function was sufficient given the primary objective was a broad comparison. Correlation functions are statistical descriptors of structure, that capture the probability or proportion of one

medium to another. More information on such approaches can be found in reference [103]. These methods however do not capture the intricacies and details of shape and dimensions and are therefore insufficient for the applications discussed in Chapters 2 and 3, which assert the relevance of feature aspect ratios as a driver for deformation mechanisms.

For studies where such information has been desired by researchers, the most common approach has been to manually measure these feature dimensions and calculate an average. However, this is often a tedious process that is prone to human error and measurement bias in cases where features are not easily identifiable. Therefore, to ensure consistency and relative accuracy, a large dataset must be obtained, further increasing the difficulty of the process. Homogeneity must also be ensured in test samples to increase confidence in averaging.

B.1.3   Summary of approach

Most of the approaches were found to be insufficient for the purposes of our studies, hence the approach outlined here of using the underlying skeletal framework was developed. It is stressed that this technique is no way intended to serve as an absolute and perfectly accurate means of evaluating material properties: The randomness and often complex geometry associated with these structures complicates any effort to characterize or obtain averaged results. Instead, this approach intends to qualitatively assess these key parameters, primarily as a means of comparing structures to predict similarities in mechanical response. Although in certain situations, the results of this analysis can be used to delineate ligament features for strain mapping or provide reasonable estimates for averages, these results are not ideal and are often used for illustrative purposes and not as detailed predictors. This is reflected in the chapters above, as no definitive conclusions

were based on estimated results. To summarize once again, the skeletonization script serves the following purposes:

1. Provides a means of objectively deciphering ligaments and junctions for measuring feature aspect ratios

2. Provides a convenient method of obtaining a large dataset in order to more accurately capture the distribution of features

3. Provides a means of comparing NP metal structures to assess similarities

More details on the approach, including the basic methodology and the way it utilized, is outlined below.

B.2 Adopted Approach

B.2.1 Skeletonization

Morphological operations in general have been widely adopted as a means of simplifying image data by eliminating irrelevancies while preserving essential shape characteristics. Skeletonization is an example of these morphological operations that can be used to obtain the underlying framework for a 2D image. These resulting frameworks can subsequently be analyzed in a vast number of ways depending on the desired application. This versatility with image analysis that builds of the derived skeleton has made the method attractive in a variety of applications that have required some form of pattern recognition. This could range from biological applications, such as the numerous cases in medical imaging, to other more conventional computer vision applications such as motion tracking and animation [104-107]. (ref. [108] provides a useful review of some of the broader applications)

Several approaches have been developed to extract skeletons from 2D or 3D images. The idealness of a specific skeletonization approach is difficult to quantify given the ambiguity of a basis for comparison. However, several qualities have generally been adopted in assessing a skeleton. These may include topology preservation, thinness, the centered nature in geometry, and robustness, to name a few. The broadness of these criteria means that no single approach can be regarded as ideal; instead, each method displays strengths and weakness that must be assessed in the context of the desired application. Several studies, such as by A. Sobiecki et al. [104] haveconducted comparisons of different skeletonization algorithms and methods on a variety of images. These all reinforce the conclusion that the effectiveness of a method will be dependent on the application. In order to select a skeletonization method, the limitations must be understood and as many applicable scenarios as possible must be evaluated qualitatively.

For our study, the most critical qualities are the abilities to preserve topology, to consistently produce a pixel thin skeleton that is centered in the geometry, and to preserve fine scale details. Under these criteria, the thinning algorithms proved most ideal. This algorithm extracts the skeleton by iteratively thinning the binarized feature using a structural element until the feature is reduced to a pixel-thick skeleton. Additional details on the algorithm, including details on how transformation operations and structural elements are modified to preserve the topology of original features, can be found in ref [105].

Once the skeleton is obtained, it can be interpreted much more easily than would a more complex feature. Figure 37 [106] helps illustrates this. The binary pixel-thick features mean that information such as endpoints, intersection points can be extracted based on the

96

connectivity of an active pixel (active pixel here refers to white pixels with a value of 1, as opposed to black pixels that have a value of zero) to other active pixels. For instance, endpoints in the skeleton of Figure 37 can be ascertained by identifying active pixels that are connected to a single other active pixel. Similarly, intersection points can be identified as pixels connected to three or more other active pixels.
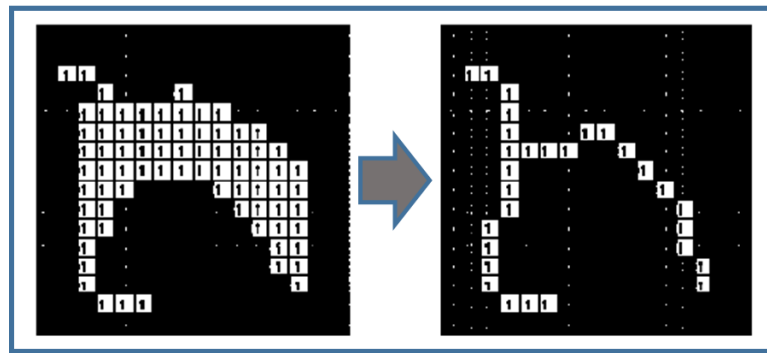
Figure 37: Illustrating the skeletonization process

Interpretations such as these require a robust definition of pixel connectivity arrangements, in the form of structural elements, as they correspond to various positions on a skeleton. Once defined, the structural elements can be used to identify regions that match the arrangements and their coordinates are recorded.

B.2.2   *Adapting the skeletonization method*

Once the underlying skeleton was obtained using the skeletonization algorithm, additional code must be generated to obtain desired information and outputs in line with our analysis requirements of examining feature aspect ratios. The basic principle we use in this work is to take advantage of the underlying skeletal framework to identify junction centers from which junction size can be estimated and ligaments isolated upon removal of

junctions. For the studies conducted in this work, an algorithm was developed, centered around the function, which is based on an iterative thinning algorithm described in ref [105]. MATLAB's bwmorph 'skel' function was used to extract the underlying skeleton, after which additional operations were carried out to obtain necessary parameters. The key steps of the process are summarized in the figure below. The initial skeleton served primarily to capture the underlying network of the structure being examined, however it represented only a small fraction of the overall algorithm; the rest of the algorithm, although lengthy and complex, simply served to extract the relevant information in an automated manner, while addressing any observed issues in the accuracy of results.

The skeletal processing portion of the algorithm began by identifying the centers of junctions, which were recognized as the intersection points of the skeleton (see smaller blue circles in Figure 38(a), reproduced from Chapter 2). Once identified, the size of the junctions associated with those centers was estimated by iteratively expanding circles, centered at those intersection points. Once the circumference of these circles reached the edge of the junction, the iteration was halted and the area within the circles isolated. The resulting isolated region provided a good estimate of the junction dimensions, and the 'regionprops' function in MATLAB was called to estimate the area of the regions.
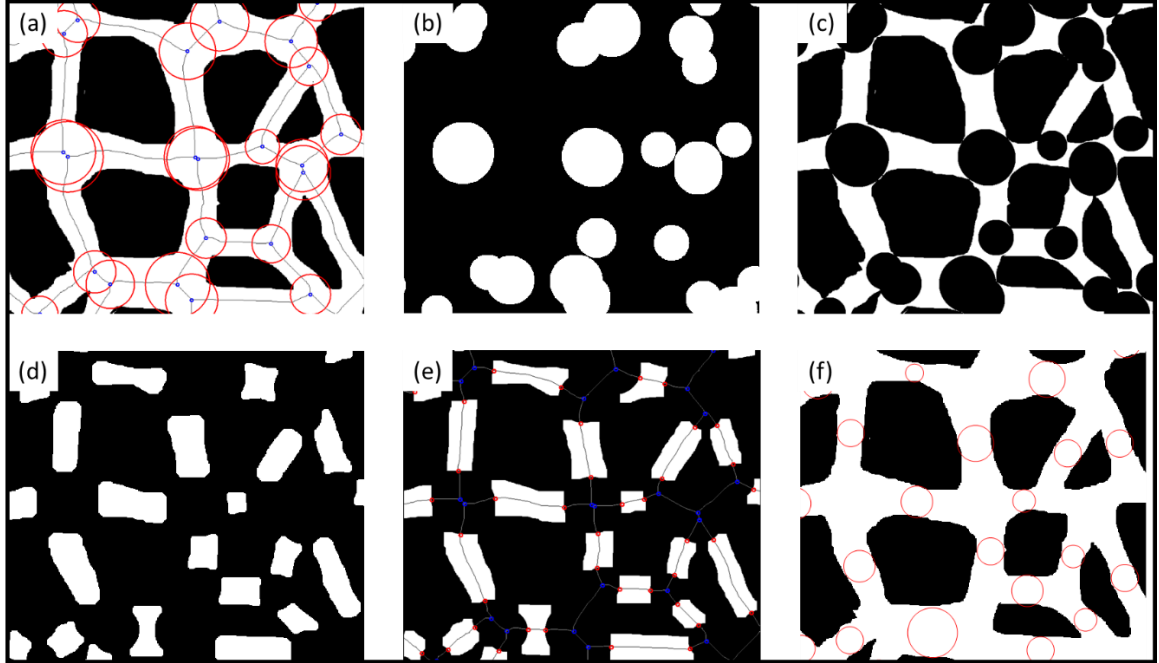
Figure 38: Summary of skeletonization procedure

With junctions isolated, the skeletal framework was once again incorporated in predicting ligament information. This process began by superimposing the skeleton on the junction-free structure, to identify the intersection points of the skeleton and junction edges. These points are the endpoints of the ligaments and the distance between the points served to capture the length of individual ligaments. Finally, to estimate the ligament width, the 'regionprops' command was called once again, here to identify the centroid of ligaments. Once this centroid was obtained, a circle was constructed around the center with its diameter iteratively increased until the circumference intersected the surface of the ligament (see Figure 38(f)). The diameter of the final circle was recorded as the width of the ligament.

B.2.2   Implementation

The skeletonization algorithm was applied to three sets of samples: The 3D printed RF structures, the 3D printed MD-Based AM structures, and actual SEM images of NP Pt. Each set presented unique challenges; however, effort was made to maintain consistency in the approach, so as to avoid measurement bias. In each case, the skeleton analysis must begin with a binary mask representative of the structure. Given that such a mask must be 2-dimensional in nature, effort must be made to ensure that the 2D version of the mask accurately represents the underlying 3D structure. Some considerations in this regard are addressed shortly.

B.2.2.1   3D Printed RF structures

The skeletonization process was applied to the RF structure mainly as a means of evaluating the approach by identifying ligaments using both manual selection and the skeletonization algorithm. The RF structures have the initial benefit of possessing clearly defined features, allowing us to easily verify that predicted feature dimensions for a randomized structure reflected actual feature proportions. Furthermore, the relatively small size of the structure (the 2D projected image captures about 100 features or even less compared to actual nanoporous platinum samples that could capture several hundred features, depending on the size scale of the image) meant that it was easier to manually verify measurements. These benefits made the RF structures an excellent set for assessing the effectiveness of the approach on a random lattice structure.

The first step of the process involves identifying surface level features to be analyzed. This was done manually but aided by the shallow depth of field of the camera

during imaging. Image processing steps helped highlight in-focus regions which could be manually differentiated from other regions. While not ideal, this process was most effective in obtaining the structure. An example conversion for the lowest density structure is shown in Figure 39 below.
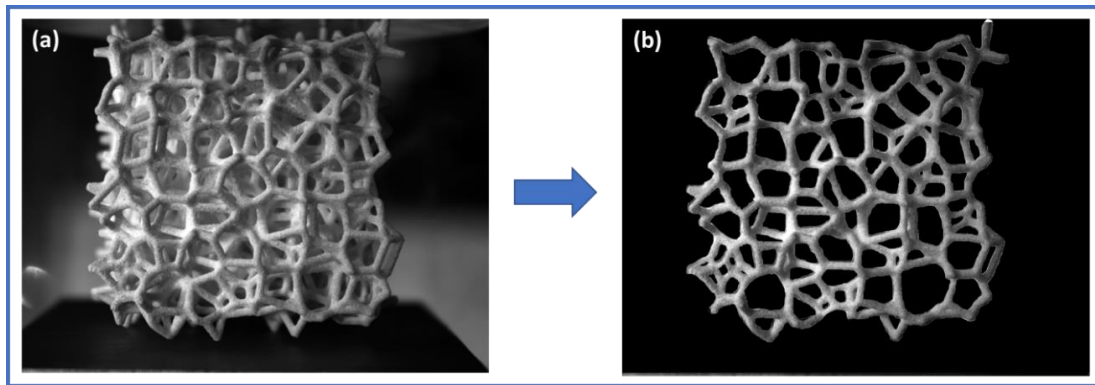
Figure 39: Sample feature isolation performed on lowest density RF structure

Once completed, the image was binarized to create a mask that was applied primarily for strain analysis, but also for the skeletonization process. The resulting masks are shown in Figure 40 in order of increasing density from left to right, where blue regions represent ligaments and orange regions are junctions.
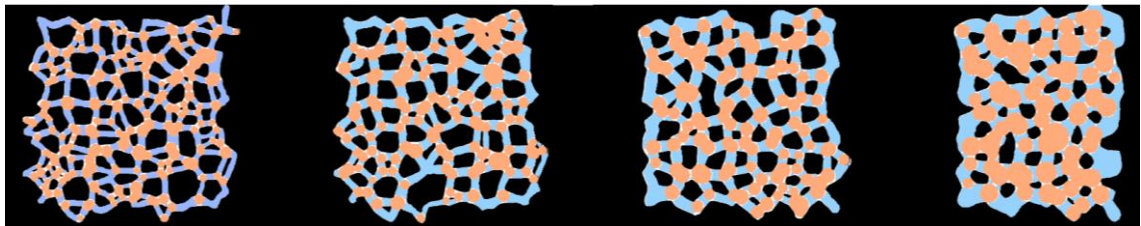
Figure 40: Processed RF masks showing ligament versus junction delineation

For the MD-Based structures, the skeletonization approach was also applied to assess the potential impact of geometry on mechanics. The complicated nature of these structures made manual characterization difficult, hence greater emphasis was placed on consistency in characterization approach. The overall approach follows the same steps as adopted for the RF structures to obtain a relevant mask. The irregular shape of the junctions presented minor challenges when fitting circles to define junctions, but slight modifications to the code to trim ligament feature edges helped address these issues.

The resulting masks used in the analysis are shown in Figure 41 below. Once again, the blue regions represent ligaments, while orange regions indicate junctions.
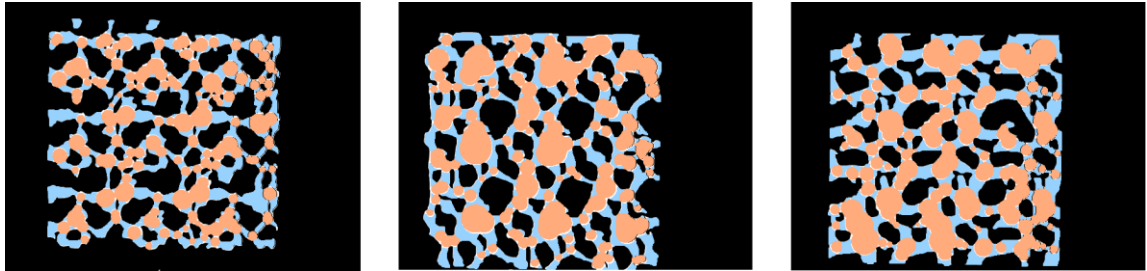
Figure 41: Processed MD-Based masks showing delineated junctions and ligaments

B.2.2.3   Physical NP Pt Structures

Characterization work done on physical NP Pt made use of SEM images, which provide 2D projections of the porous structure. As with other sample sets, a mask was necessary for implementing the skeletonization algorithm. This mask was created by binarizing thresholded SEM images as illustrated in the example process of Figure 42 (a-

b) (this process was not possible for 3D printed samples due to lighting and background effects). The bandpass filter maximized the definition of surface level features, as dictated by setting an appropriate bandwidth. This simplified the binarization procedure, so that once masks were created, the skeletonization process captured the features shown in Figure 42
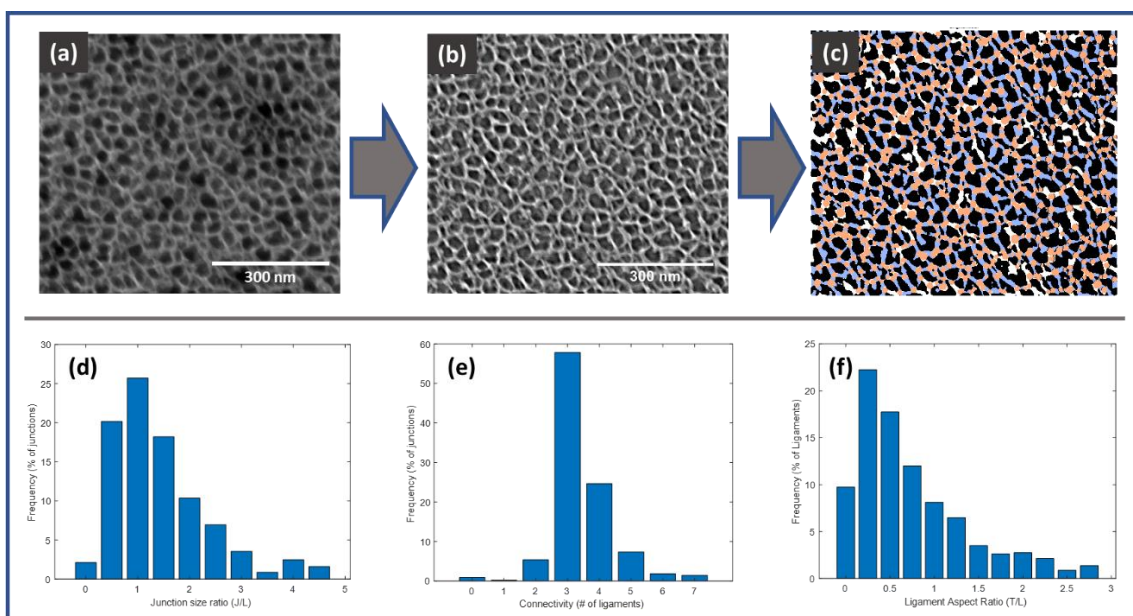
Figure 42: Sample processing path for physical NP Pt samples

It should be noted that given the typical size of images used in characterizing actual NP Pt, a larger sample set can be obtained, which is beneficial for statistical averaging. However, working at this scale also risks eliminating some of the detail associated with the structure. For instance, some smaller ligaments or features may be indistinguishable from each other when in close proximity. Thus, the images shown may not possess as much detail as the MD-Based set. Fortunately, however, the lack of detail does not compromise

information on parameter aspect ratios; nevertheless, careful consideration must be made when imaging large samples for future analyses.

B.2.3   Assessment and Limitations

The effectiveness of the skeletonization algorithm can be assessed in a number of ways. Here, some of these are outlined to help build confidence in the outlined procedure. Once again, it is important that the reader recognizes that this methodology is largely qualitative, with the benefit of minimizing bias in conclusions. Details on this are provided below.

B.2.3.1   Evaluating the skeletonization approach

Recall from the introductory section of this Appendix section that the skeletonization algorithm served three primary purposes in this work. They are:

1. Provides a means of objectively deciphering ligaments and junctions for measuring feature aspect ratios

2. Provides a convenient method of obtaining a large dataset in order to more accurately capture the distribution of features

3. Provides a means of comparing NP metal structures to assess similarities

The primary means of addressing these objectives involved the use of histograms. This method was adopted over bulk averages because, although more qualitative, it provides much more information on the structure of a random NP metal and significant detail can be inferred from the distributions, as opposed to averaging. In light of this, we assess the technique with two questions in mind.

1. Is it possible to qualitatively interpret the key attributes of structure using histogram distributions?

2. How effective is the approach in differentiating a structure from contrasting structures with significant geometrical differences?

To answer these questions, we test the method on structurally different sample images and ascertain the unique details that can be interpreted from each image. The sample images used are shown in Figure 43. The first image shown, Figure 43(a), is an SEM image of a NP Pt sample, which is the primary system used in this work. The remaining images were taken from the literature: Figure 43(b) is of NP Cu, as reported by ref [107], while Figure 43(c) is of NP Au, as reported by ref [108]. These images were selected solely for their quality and serve only to demonstrate the skeletonization algorithm.
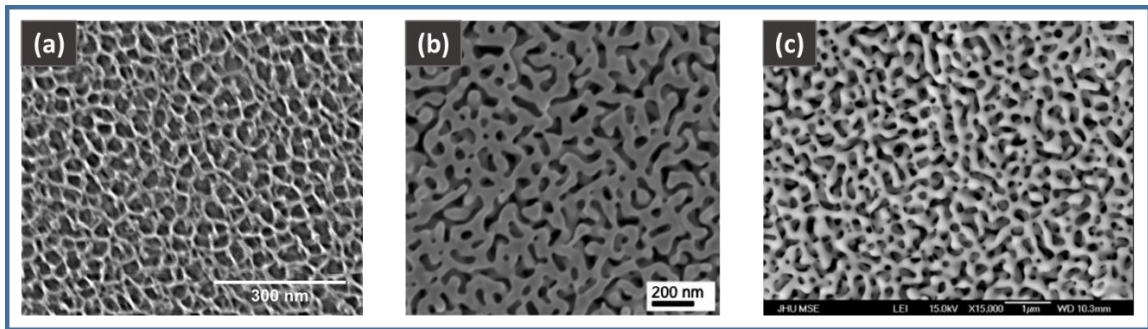
Figure 43: Sample NP metal images of skeletonization comparison

Before applying the approach, we can first examine the figure and assess the main attributes. Based on the images provided, few things are noteworthy. First, the structures are clearly different from each other. They appear to possess thicker ligaments and larger

junctions that are similar in size to the ligaments. We can now examine how much of this can be discerned from the skeletonization algorithm.

The key results of the skeletonization algorithm are shown in Figure 44 below. We can unpack much from these figures and apply the results to address the first question. Here we examine the distributions for the ligament and junction aspect ratios.
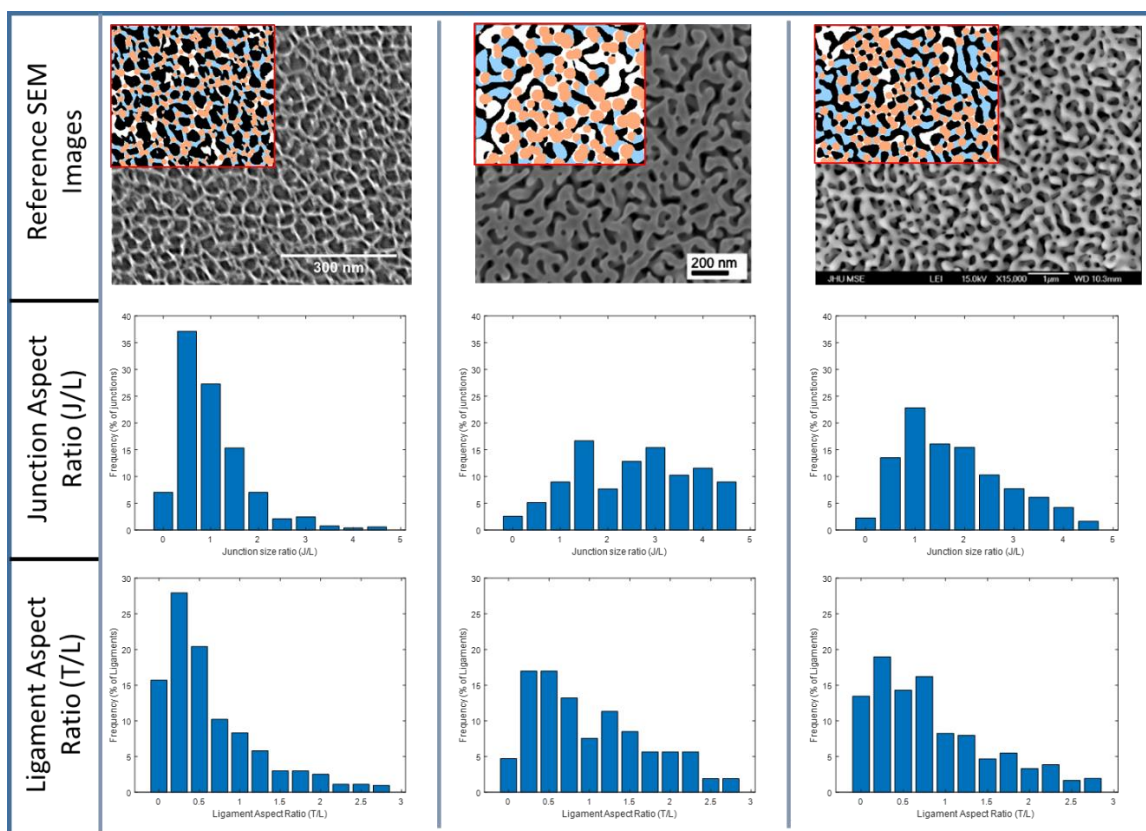
Figure 44: Skeletonization summary for examined NP metals

The junction aspect ratio compares the size of a junction to the length of the ligaments to which it is attached. We observe very clear differences for each image: For the NP Pt image, there is a high proportion of junctions with low aspect ratio, reflecting

the longer slender ligaments, clearly apparent in the NP Pt image. In contrast, junctions are larger in the NP Cu and NP Au structures, but not significantly so when compared to the ligaments. There is greater homogeneity, which is reflected in the broader distribution, localized on high values that capture smaller ligament lengths.

Furthermore, the ligament aspect ratio, which captures the ratio of the ligaments thickness to its length, or the slenderness of the ligament, is also varied for each structure, as would be expected. The NP Pt structures shown here have slender ligaments, which is reflected in the smaller localized values in the histograms, whereas for the NP Cu image, junctions are wider and shorter, resulting in a broader distribution of values. The NP Au shows a similar behavior to NP Cu, but with a few notable ligaments that are long and slender, hence the prominence of the first data bar in its T/L plot.

These are just some of the deductions that can be made from analyzing histograms from the skeletonization process; much of this information is lost when an average value is used since the distributions are not necessarily normal, despite the size of the data. Nevertheless, given the effort required to draw reliable conclusions from the histograms, emphasis in this work is not placed on interpreting the structures using the distributions alone; rather, we adopt the distributions primarily as a means of comparing structures, with the understanding that significantly similar structures will display similar trends, which can be linked to their mechanics. (Note that this method of qualitative comparison is much more effective than the 2-point correlation method highlighted in Chapter 4 as that method did not account for impact of feature geometry). This brings us to the second question, which relates to the effectiveness in comparing different structures. Here, we seek to verify that discernible differences can be utilized to effectively differentiate between structures

of different makeup. These differences were already apparent from Figure 44, but the idea is further demonstrated in Figure 45 below.
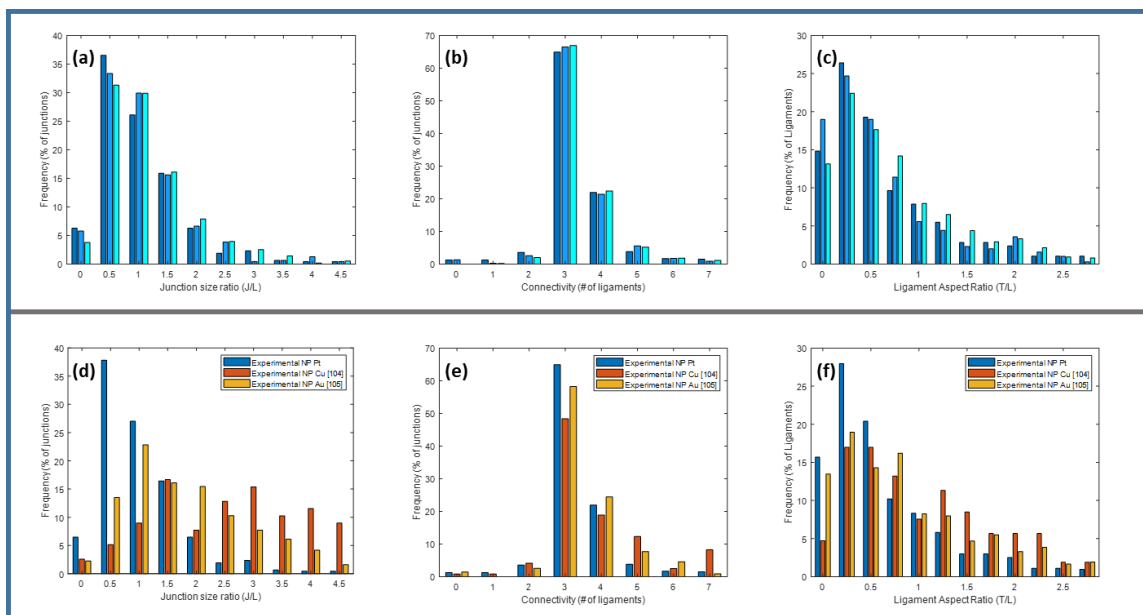
Figure 45: Variation in distribution for NP metals

Here, the histograms are superimposed for comparison: On the top row, three NP Pt samples are compared, while on the bottom row, the three structures from Figure 43 are compared. The main takeaway from this figure is the similarity in the distributions when the same type of NP metal is compared, versus when fundamentally different types are compared as in Figure 45 (d through f). This figure illustrates the effectiveness of the histograms shown in Chapter 3 as a qualitative yet reliable tool of comparing structures more effectively than with lumped averages.

B.2.3.2 Additional considerations in approach

Several other considerations must be made when applying the skeletonization algorithm. Some of these can be inferred through proper examination of histograms and resulting junction-ligament allocations. For instance, a common issue for structures with very short ligaments and very large junctions, is a scenario where the circles defining junctions overlap with adjacent junctions, eliminating the connecting ligament and giving the impression of an oversized but distorted junction. Such phenomena can be tracked using the level of connectivity, since such hybrid junctions will be connected to ligaments for both junctions, thus doubling its connectivity. For example, the NP Cu image used in Figure 44 displayed this phenomenon, and it was reflected in the connectivity histogram of Figure 45 where we see a spike in junctions with connectivity of 7 or above.

Furthermore, the viability of the aspect ratio distribution as a means of assessing mechanics may only be valid below a certain relative density, and this threshold needs to be understood. For instance, consider the RF structures examined in detail in Chapter 2. We observe a transition from bending dominated behavior to compression dominated behavior. This is likely linked to the ligament aspect ratio but as Figure 46 below shows, identifying junctions and ligaments becomes more difficult at higher relative densities and information becomes more difficult to interpret. Overall, scenarios such as these must be carefully monitored and accounted for when exploring structures with higher densities.
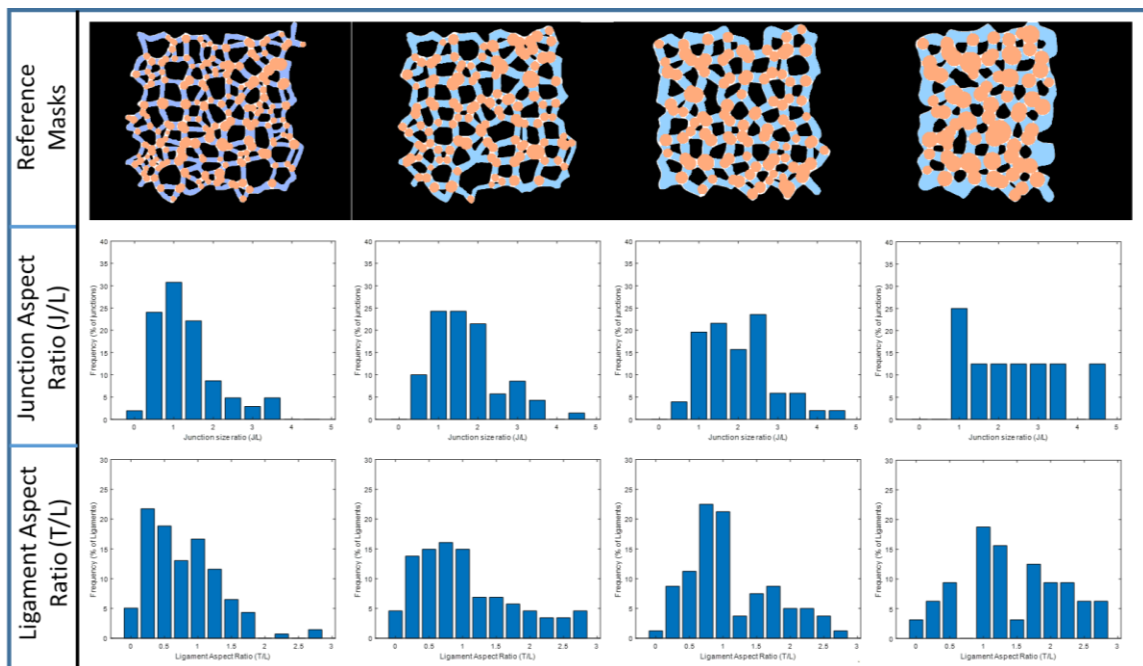
Figure 46: Histogram distributions for RF structures

Another critical observation that can be drawn from this effort to explore the impact of relative density is the minimization in sample size. As already highlighted, junction expansion in higher density structures could lead to smaller ligaments being absorbed, creating super junctions that are much larger in size but connected to fewer ligaments. In a scenario, such as shown in Figure 46, where resolution remains consistent, this leads to an overall reduction in sample size, which is reflected in the more arbitrary nature of the distributions (see for instance, J/L distribution for highest density sample). This poses a significant issue that both compromises the ability to interpret distributions, but also minimizes the effectiveness of the average as a way of capturing the characteristic geometry of the structure. To address this issue, more work must be done to determine the critical relative density beyond which this approach may no longer be valid.

110

B.2.3.3   Additional considerations in algorithm

The outlined process, on the most fundamental level, proved effective for characterization. However, depending on the structures being evaluated, certain challenges may arise. Therefore, to generalize the approach and ensure its accuracy under any scenario, multiple tests were conducted to assess the effectiveness under various circumstances with improvements made to the algorithm over time. Assessment was made possible by tracking the progress of all analyses in detail. For instance, the plotting of circles shown in Figure 38 was incorporated to every analysis and helps the user confirm that the right features are being measured. Overall, a conservative approach was applied to the algorithm, neglecting data points that could compromise the averaged values or distributions.

Modifications to the code aimed to minimize error in prediction, the most critical of these is associated with the elimination of free-standing ligaments and omitted data: Branches in skeletons are an unwanted artefact that is created by noisy ligament definition or free-standing edge ligaments. The algorithm eliminates these branches, which may sometimes lead to omission of the junctions to which they are connected to. This impact has been ignored as it has minimal effect on overall statistics: The average connectivity is estimated directly using the skeleton, meaning that the average is unaffected, but omitting few ligaments and junction merely entailed fewer statistical data points, which is a negligible effect when the situation only applies to a fraction of ligaments. Overly deformed ligaments are also ignored in the algorithm because these can often be confused with junctions having two-ligament connectivity. Once again, to avoid erroneous

information, these are excluded altogether. The effects of these omissions can be observed in Figure 42 for instance, where some white regions are undefined

B.2.3.4 Assessing out-of-plane impact

Effectiveness of the approach to identify features has already been addressed in prior sections, but other practical estimates of error can be quantified in a case dependent manner. For the key parameters, (the junction aspect ratio, ligament aspect ratio, and connectivity), which proved most critical in Chapter 3 as a means of assessing the similarities of structures, an expected error arises due to the 2D approximation and its comparison to a 3D structure. Specifically, some error is expected to arise with the assumption that ligaments are oriented parallel to the viewing plane, primarily for the ligament aspect ratio. To understand the source of this error, consider the schematic shown in Figure 47 for two cases of ligament orientation. The first case is the assumed orientation for 2D skeletonization, however Case 2 is more realistic, and reflects the random orientation of ligaments in 3D space, often off from the viewing plane. The error in length measurement (L_{meas}) is therefore affected by the angle of orientation and the true length.
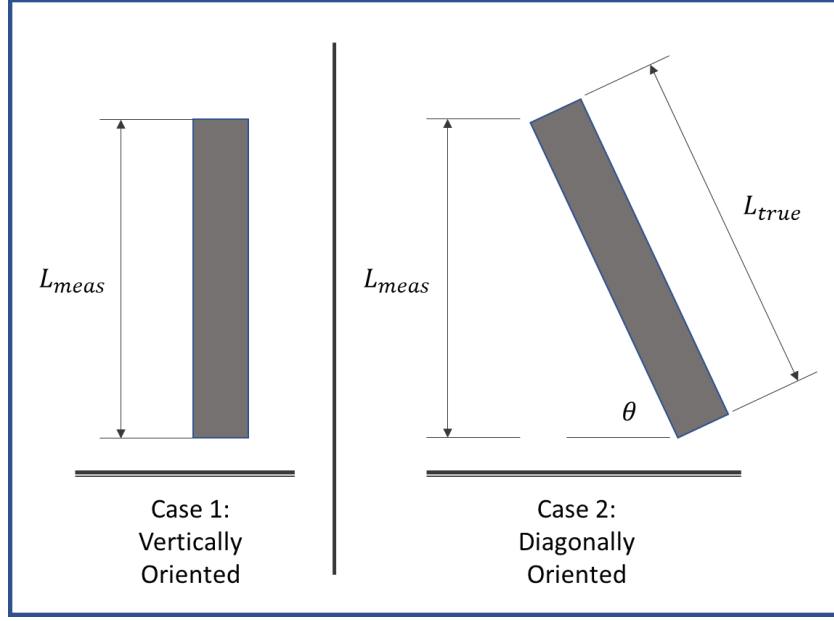
Figure 47: Schematic illustration for error approximation associated with 2D analysis

We can quantify this error using simple geometrical considerations. The true length can be related to the measured length as $L_{meas} = L_{true} \sin \theta$. Therefore, following some simple calculations and assuming thickness measurements are independent of orientation, we can assume a correction factor for the ligament aspect ratio (T/L) as $(1 - \sin \theta)/\sin \theta$. As is clear from the expression, an angular orientation of 90 degrees, which is the vertically oriented approximation, will imply that no error correction is needed, but as the angle approaches zero, the level error increases dramatically.

For the discussions of this thesis, Case 1 has been assumed for simplicity since orientations are expected to be minimally diagonal, but a more accurate measurement will require confirming this angle and the level of error.

B.3 Summary and Conclusion

In this appendix, we have developed and demonstrated an approach to assessing the topological features of a porous structure. The method involves extensive morphological operations on binarized versions of structures, with an emphasis on the skeleton as a tool for delineating essential features (joints and ligaments). Furthermore, the effectiveness of the approach, both from a methodological and an interpretation point of view, have been examined extensively. The accuracy of the method was evaluated with a discussion of potential sources of error, both those specific to our work and those characteristic of morphological operations in general, and our efforts to address and quantify them. Similarly, the effectiveness of the overall approach to interpreting and comparing structures has been demonstrated using case studies.

Overall, we find this approach to be effective in compensating for some of the limitations in the relative density that were made apparent in Chapter 2. In that chapter, we concluded that the relative density is insufficient as the sole descriptor of geometry since it does not capture the contribution, or lack thereof, of the agglomerated mass in junctions to the normalized properties (modulus and yield strength). The skeletonization method presented herein provides an effective means of assessing this mass accumulation in the junction using the familiar aspect ratios (J/L and T/L) that are commonly adopted in classical studies of scaling relations. Specifically, we have been able to obtain a large enough amount of data per sample to accurately and objectively assess the distribution of these key aspect ratios, providing better context for the geometrical contribution as well as the error and variation in averaged values. We show here that such distributions can be used to better interpret fundamental differences in structures.

In addition, despite the recognized inadequacy in using lumped averages over the robust information available through distributions, we found from Chapter 2 that applying averaged values (obtained using the presented skeleton-based method) to classical relationships still provide a fairly accurate means of correcting for the junction contribution. This is an especially encouraging discovery as it holds promise for a more accurate and quantifiable means of capturing the geometrical impact on mechanical properties. This effectiveness is no doubt aided by the large sample set that can be obtained using our skeleton based approach.

Further work must be done to better assess the limitations of the approach, and such efforts can build on the context available through our skeletonization approach. Limitations highlighted, such as the impact of relative density on discernable features and the resulting reduction in sample size must also be addressed. Specifically, the threshold density beyond which identified ligaments no longer provide a characteristic view of the structure must be ascertained. Such efforts can increase the versatility of the approach and help to better quantify the error in adopting classical scaling corrections, as they are specific to various conditions.

Finally, it is important to recognize that efforts to develop a more effective means of quantifying geometry need not be based on the classical aspect ratios (J/L and T/L). While these are most easily recognized from classical studies, we demonstrate here that the ability to delineate junctions from ligaments can be used directly and perhaps more effectively to capture corrected values of relative density that better relate to overall mechanics. Such an approach could circumvent the error accumulation associated with using lumped averages of factors such as J/L. The effectiveness of this method is apparent

from the sample examination of Figure 48 which shows the resulting scaling relationship when the junctions (grey regions in masks) of the MD-Based structures are removed and the relative density adjusted accordingly. Although not perfect, this method clearly holds promise in addressing the impact of junction on properties. And while the approach will rely more on experimental quantification, a fact that could make it less attractive in scenarios such as where predictions must be made in the absence of actual samples, it remains a viable option that can be explored. Furthermore, improvements can be made by incorporating strain mapping analyses, as used in Chapter 2, to assess how much of the junction truly holds no contribution so that a better estimate of how much of the junctions to remove can be established.
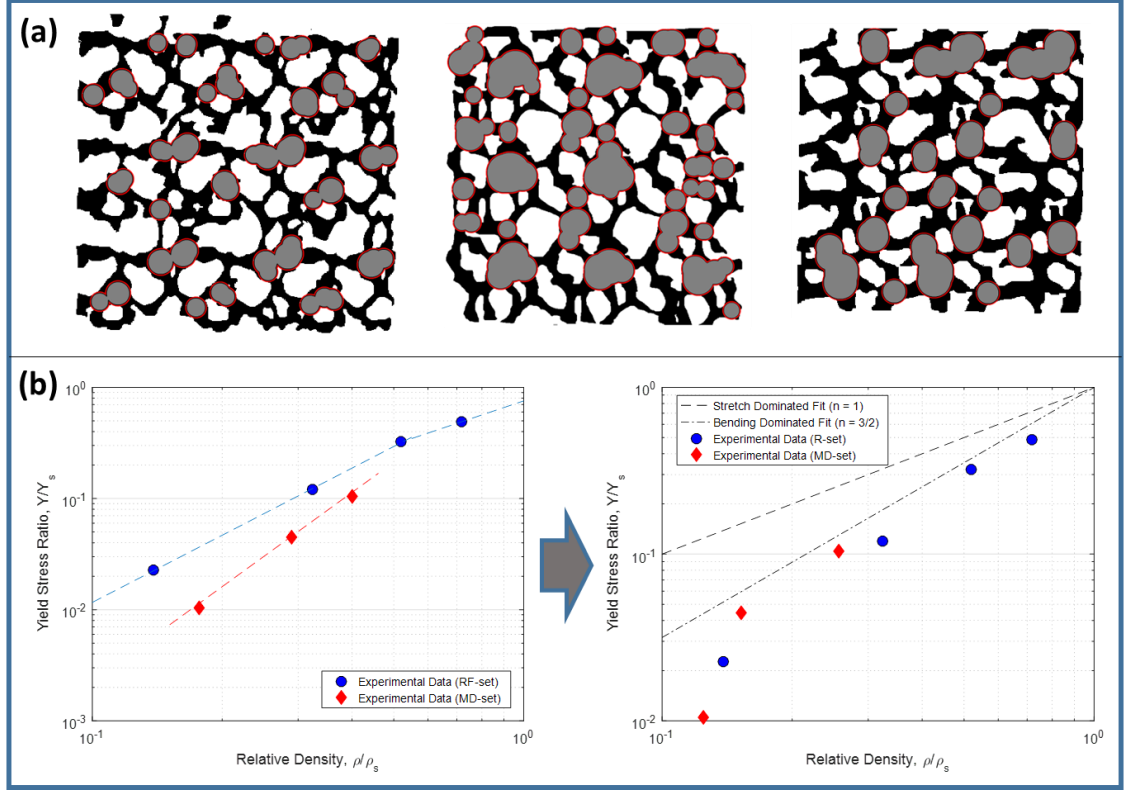
Figure 48: Assessment of alternative correction method showing (a) structures with removed junctions and (b) impact on scaling relationship

In summary, we developed a method to obtain more impartial measurements of ligament and junction aspect ratios for porous solids using image registration algorithms. This process has been shown to work for both experimental and idealized 3D printed structures after plan view images of the samples are properly thresholded. The histograms of the ligament and junction aspect ratios can serve as qualititative comparisons between local structural features. There are however challenges with the approach especially as the relative density increases to the point that ligaments become nearly indistinguishable from the junctions. In our work, this was more apparent for the experimental NP Pt samples when the relative density >60%. For those scenarios, the relative density may be a useful descriptor of the influence of geometry after it is properly adjusted to correct for enlarged

junctions or parts of the structure that do not contribute to the strength (unconnected ligaments etc.)

REFERENCES

1. Kraehnert, R., et al., *Electrochemically dealloyed platinum with hierarchical pore structure as highly active catalytic coating.* Catalysis Science and Technology, 2015. **5**(1): p. 206-216.

2. Ding, Y. and M. Chen, *Nanoporous Metals for Catalytic and Optical Applications.* MRS Bulletin, 2009. **34**(8): p. 569-576.

3. Ibru, T., et al., *Structure and mechanical behavior of dentin-inspired nanoporous copper.* Scripta Materialia, 2020. **176**: p. 99-103.

4. Bringa, E.M., et al., *Are Nanoporous Materials Radiation Resistant?* Nano Letters, 2012. **12**(7): p. 3351-3355.

5. Jin, H.J. and J. Weissmüller, *Bulk nanoporous metal for actuation.* Advanced Engineering Materials, 2010. **12**(8): p. 714-723.

6. Yu, Y., et al., *Li Storage in 3D Nanoporous Au-Supported Nanocrystalline Tin.* Advanced Materials, 2011. **23**(21): p. 2443-2447.

7. Detsi, E., P. Onck, and J.T.M. De Hosson, *Metallic Muscles at Work: High Rate Actuation in Nanoporous Gold/Polyaniline Composites.* ACS Nano, 2013. **7**(5): p. 4299-4306.

8. Şeker, E., W.-C. Shih, and K.J. Stine, *Nanoporous metals by alloy corrosion: Bioanalytical and biomedical applications.* MRS Bulletin, 2018. **43**(1): p. 49-56.

9. Shin, H.C., J. Dong, and M. Liu, *Nanoporous Structures Prepared by an Electrochemical Deposition Process.* Advanced Materials, 2003. **15**(19): p. 1610-1614.

10. Liao, C.L., et al., *Fabrication of nanoporous metal electrode by two-step replication technique.* Journal of Alloys and Compounds, 2007. **441**(1–2): p. L1-L6.

11. Kraehnert, R., et al., *Electrochemically dealloyed platinum with hierarchical pore structure as highly active catalytic coating.* Catalysis Science & Technology, 2015. **5**(1): p. 206-216.

12. Erlebacher, J., et al., *Evolution of nanoporosity in dealloying.* Nature, 2001. **410**(6827): p. 450-453.

13. Senior, N.A. and R.C. Newman, *Synthesis of tough nanoporous metals by controlled electrolytic dealloying.* Nanotechnology, 2006. **17**(9): p. 2311-2316.

14.   Zhang, J. and C.M. Li, *Nanoporous metals: fabrication strategies and advanced electrochemical applications in catalysis, sensing and energy systems.* Chemical Society Reviews, 2012. **41**(21): p. 7016-7031.

15.   Kolluri, K. and M.J. Demkowicz, *Coarsening by network restructuring in model nanoporous gold.* Acta Materialia, 2011. **59**(20): p. 7645-7653.

16.   Pia, G. and F. Delogu, *Coarsening of nanoporous Au: Relationship between structure and mechanical properties.* Acta Materialia, 2015. **99**: p. 29-38.

17.   Chen-Wiegart, Y.-c.K., et al., *Structural evolution of nanoporous gold during thermal coarsening.* Acta Materialia, 2012. **60**(12): p. 4972-4981.

18.   Ashby, M., *The properties of foams and lattices.* Philosophical Transactions of the Royal Society of London A: Mathematical, Physical and Engineering Sciences, 2006. **364**(1838): p. 15-30.

19.   Ashby, M.F. and R.F.M. Medalist, *The mechanical properties of cellular solids.* Metallurgical Transactions A, 1983. **14**(9): p. 1755-1769.

20.   Bei, H., et al., *Influence of Indenter Tip Geometry on Elastic Deformation during Nanoindentation.* Physical Review Letters, 2005. **95**(4): p. 045501.

21.   Pharr, G.M., W.C. Oliver, and F.R. Brotzen, *On the generality of the relationship among contact stiffness, contact area, and elastic modulus during indentation.* Journal of Materials Research, 1992. **7**(3): p. 613-617.

22.   Lu, C.-J. and D.B. Bogy, *The effect of tip radius on nano-indentation hardness tests.* International Journal of Solids and Structures, 1995. **32**(12): p. 1759-1770.

23.   Xue , Z., et al., *The Influence of Indenter Tip Radius on the Micro-Indentation Hardness.* Journal of Engineering Materials and Technology, 2002. **124**(3): p. 371-379.

24.   Oliver, W.C. and G.M. Pharr, *An improved technique for determining hardness and elastic modulus using load and displacement sensing indentation experiments.* Journal of Materials Research, 1992. **7**(6): p. 1564-1583.

25.   Oliver, W.C. and G.M. Pharr, *Measurement of hardness and elastic modulus by instrumented indentation: Advances in understanding and refinements to methodology.* Journal of Materials Research, 2004. **19**(1): p. 3-20.

26.   McElhaney, K., J.J. Vlassak, and W.D. Nix, *Determination of indenter tip geometry and indentation contact area for depth-sensing indentation experiments.* Journal of Materials research, 1998. **13**(5): p. 1300-1306.

27.   Onck, P.R., E.W. Andrews, and L.J. Gibson, *Size effects in ductile cellular solids. Part I: modeling.* International Journal of Mechanical Sciences, 2001. **43**(3): p. 681-699.

28.   Andrews, E.W., et al., *Size effects in ductile cellular solids. Part II: experimental results.* International Journal of Mechanical Sciences, 2001. **43**(3): p. 701-713.

29.   Tabor, D., *The hardness of metals.* 2000: Oxford university press.

30.   Fei, H., et al., *Evaluation of Micro-Pillar Compression Tests for Accurate Determination of Elastic-Plastic Constitutive Relations.* Journal of Applied Mechanics, 2012. **79**(6).

31.   El-Awady, J.A., et al., *Effects of focused ion beam induced damage on the plasticity of micropillars.* Physical Review B, 2009. **80**(10): p. 104104.

32.   Shim, S., et al., *Effects of focused ion beam milling on the compressive behavior of directionally solidified micropillars and the nanoindentation response of an electropolished surface.* Acta Materialia, 2009. **57**(2): p. 503-510.

33.   Liu, R., et al., *Mechanical properties of nanocrystalline nanoporous platinum.* Acta Materialia, 2016. **103**: p. 624-632.

34.   Hu, K., et al., *Nanoporous gold: 3D structural analyses of representative volumes and their implications on scaling relations of mechanical behaviour.* Philosophical Magazine, 2016. **96**(32-34): p. 3322-3335.

35.   Liu, L.-Z., X.-L. Ye, and H.-J. Jin, *Interpreting anomalous low-strength and low-stiffness of nanoporous gold: Quantification of network connectivity.* Acta Materialia, 2016. **118**: p. 77-87.

36.   Liu, R. and A. Antoniou, *A relationship between the geometrical structure of a nanoporous metal foam and its modulus.* Acta Materialia, 2013. **61**(7): p. 2390-2402.

37.   Mangipudi, K.R., E. Epler, and C.A. Volkert, *Topology-dependent scaling laws for the stiffness and strength of nanoporous gold.* Acta Materialia, 2016. **119**: p. 115-122.

38.   Mangipudi, K.R., et al., *A FIB-nanotomography method for accurate 3D reconstruction of open nanoporous structures.* Ultramicroscopy, 2016. **163**: p. 38-47.

39.   Volkert, C.A., et al., *Approaching the theoretical strength in nanoporous Au.* Applied Physics Letters, 2006. **89**(6): p. 061920.

40.   Hodge, A.M., et al., *Characterization and Mechanical Behavior of Nanoporous Gold.* Advanced Engineering Materials, 2006. **8**(9): p. 853-857.

41.   Farkas, D., et al., *Mechanical response of nanoporous gold.* Acta Materialia, 2013. **61**(9): p. 3249-3256.

42.   Sun, X.-Y., et al., *Mechanical properties and scaling laws of nanoporous gold.* Journal of Applied Physics, 2013. **113**(2): p. 023505.

43.   Crowson, D.A., D. Farkas, and S.G. Corcoran, *Geometric relaxation of nanoporous metals: The role of surface relaxation.* Scripta materialia, 2007. **56**(11): p. 919-922.

44.   Zinchenko, O., et al., *Nanoporous gold formation by dealloying: A Metropolis Monte Carlo study.* Computer Physics Communications, 2013. **184**(6): p. 1562-1569.

45.   Huber, N., et al., *Scaling laws of nanoporous metals under uniaxial compression.* Acta materialia, 2014. **67**: p. 252-265.

46.   Plimpton, S., *Fast parallel algorithms for short-range molecular dynamics.* Journal of computational physics, 1995. **117**(1): p. 1-19.

47.   Stukowski, A., *Visualization and analysis of atomistic simulation data with OVITO–the Open Visualization Tool.* Modelling and Simulation in Materials Science and Engineering, 2009. **18**(1): p. 015012.

48.   Makiyama , A.M., S. Vajjhala , and L.J. Gibson, *Analysis of Crack Growth in a 3D Voronoi Structure: A Model for Fatigue in Low Density Trabecular Bone.* Journal of Biomechanical Engineering, 2002. **124**(5): p. 512-520.

49.   Hild, F. and S. Roux, *Digital image correlation*. 2012: Wiley-VCH, Weinheim.

50.   Hild, F. and S. Roux, *Digital image correlation: from displacement measurement to identification of elastic properties–a review.* Strain, 2006. **42**(2): p. 69-80.

51.   Blaber, J., B. Adair, and A. Antoniou, *Ncorr: open-source 2D digital image correlation matlab software.* Experimental Mechanics, 2015. **55**(6): p. 1105-1122.

52.   Yahyazadehfar, M., et al., *On the mechanics of fatigue and fracture in teeth.* Applied mechanics reviews, 2014. **66**(3).

53.   Antoniou, A., et al., *Controlled nanoporous Pt morphologies by varying deposition parameters.* Applied Physics Letters, 2009. **95**(7): p. 073116.

54.   Gibson, I. and M.F. Ashby, *The mechanics of three-dimensional cellular materials.* Proceedings of the Royal Society of London. A. Mathematical and Physical Sciences, 1982. **382**(1782): p. 43-59.

55.   Hakamada, M., et al., *Density dependence of the compressive properties of porous copper over a wide density range.* Acta Materialia, 2007. **55**(7): p. 2291-2299.

56. Gopikrishna, V., *Sturdevant's Art & Science of Operative Dentistry-E-Book: A South Asian Edition*. 2015: Elsevier Health Sciences.

57. Vennat, E., *Étude expérimentale et numérique de l'infiltration de la dentine déminéralisée en surface par des résines composites*. 2009, Châtenay-Malabry, Ecole centrale de Paris.

58. Montoya, C., D. Arola, and E.A. Ossa, *Importance of tubule density to the fracture toughness of dentin.* Archives of Oral Biology, 2016. **67**: p. 9-14.

59. Imbeni, V., et al., *The dentin-enamel junction and the fracture of human teeth.* Nature Materials, 2005. **4**(3): p. 229-232.

60. Bertassoni, L.E., *Dentin on the nanoscale: Hierarchical organization, mechanical behavior and bioinspired engineering.* Dental Materials, 2017. **33**(6): p. 637-649.

61. Toledano, M., et al., *Load cycling enhances bioactivity at the resin-dentin interface.* Dental Materials, 2014. **30**(7): p. e169-e188.

62. Spencer, P., et al., *Adhesive/dentin interface: The weak link in the composite restoration.* Annals of Biomedical Engineering, 2010. **38**(6): p. 1989-2003.

63. Sarrett, D.C., *Clinical challenges and the relevance of materials testing for posterior composite restorations.* Dental Materials, 2005. **21**(1): p. 9-20.

64. Van Dijken, J.W.V. and U. Pallesen, *Clinical performance of a hybrid resin composite with and without an intermediate layer of flowable resin composite: A 7-year evaluation.* Dental Materials, 2011. **27**(2): p. 150-156.

65. Hamouda, I.M., *Current perspectives of nanoparticles in medical and dental biomaterials.* Journal of Biomedical Research, 2012. **26**(3): p. 143-151.

66. Yu, Q., Z. Wu, and H. Chen, *Dual-function antibacterial surfaces for biomedical applications.* Acta Biomaterialia, 2015. **16**(1): p. 1-13.

67. Shrestha, A., et al., *Delivery of Antibacterial Nanoparticles into Dentinal Tubules Using High-intensity Focused Ultrasound.* Journal of Endodontics, 2009. **35**(7): p. 1028-1033.

68. Magloire, H., et al., *Odontoblast: A mechano-sensory cell.* Journal of Experimental Zoology Part B: Molecular and Developmental Evolution, 2009. **312**(5): p. 416-424.

69. Parlett, C.M.A., K. Wilson, and A.F. Lee, *Hierarchical porous materials: Catalytic applications.* Chemical Society Reviews, 2013. **42**(9): p. 3876-3893.

70. Mohan, K., et al., *A Review of Nanoporous Metals in Interconnects.* JOM, 2018. **70**(10): p. 2192-2204.

71. Thorp, J.C., et al., *Formation of nanoporous noble metal thin films by electrochemical dealloying of Pt xSi 1-x.* Applied Physics Letters, 2006. **88**(3): p. 1-3.

72. Hodge, A.M., et al., *Scaling equation for yield strength of nanoporous open-cell foams.* Acta Materialia, 2007. **55**(4): p. 1343-1349.

73. Sun, Y. and T.J. Balk, *A multi-step dealloying method to produce nanoporous gold with no volume change and minimal cracking.* Scripta Materialia, 2008. **58**(9): p. 727-730.

74. Liu, R. and A. Antoniou, *A relation between relative density, alloy composition and sample shrinkage for nanoporous metal foams.* Scripta Materialia, 2012. **67**(12): p. 923-926.

75. Liu, R., et al., *Synthesis and mechanical behavior of nanoporous nanotwinned copper.* Applied Physics Letters, 2013. **103**(24): p. 241907.

76. Aburada, T., J.M. Fitz-Gerald, and J.R. Scully, *Synthesis of nanoporous copper by dealloying of Al-Cu-Mg amorphous alloys in acidic solution: The effect of nickel.* Corrosion Science, 2011. **53**(5): p. 1627-1632.

77. Dan, Z., et al., *Fabrication of nanoporous copper by dealloying amorphous binary Ti-Cu alloys in hydrofluoric acid solutions.* Intermetallics, 2012. **29**: p. 14-20.

78. Wang, Z., et al., *Fabrication and new electrochemical properties of nanoporous Cu by dealloying amorphous Cu-Hf-Al alloys.* Intermetallics, 2015. **56**: p. 48-55.

79. Abramoff, M.D., P.J. Magelhaes, and S.J. Ram, *Image processing with Image.* Biophotonics Int., 2004. **11**(7): p. 36-42.

80. Vennat, E., et al., *Demineralized dentin 3D porosity and pore size distribution using mercury porosimetry.* Dental Materials, 2009. **25**(6): p. 729-735.

81. Zack, G.W., W.E. Rogers, and S.A. Latt, *Automatic measurement of sister chromatid exchange frequency.* Journal of Histochemistry and Cytochemistry, 1977. **25**(7): p. 741-753.

82. Berryman, J.G., *Measurement of spatial correlation functions using image processing techniques.* Journal of Applied Physics, 1985. **57**(7): p. 2374-2384.

83. Blair, S.C., P.A. Berge, and J.G. Berryman, *Using two-point correlation functions to characterize microgeometry and estimate permeabilities of sandstones and porous glass.* Journal of Geophysical Research B: Solid Earth, 1996. **101**(9): p. 20359-20375.

84. Liu, R., et al., *In situ frustum indentation of nanoporous copper thin films.* International Journal of Plasticity, 2017. **98**: p. 139-155.

85. Oliver, W.C., *An improved technique for determining hardness and elastic modulus using load and displacement sensing indentation experiments.* Journal of Materials Research, 1992. **7**(6): p. 1564-1583.

86. de Magalhaes, M.F., et al., *Measurement of thermophysical properties of human dentin: effect of open porosity.* Journal of dentistry, 2008. **36**(8): p. 588-594.

87. Kinney, J.H., et al., *Mineral Distribution and Dimensional Changes in Human Dentin during Demineralization.* Journal of Dental Research, 1995. **74**(5): p. 1179-1184.

88. Deyhle, H., O. Bunk, and B. Müller, *Nanostructure of healthy and caries-affected human teeth.* Nanomedicine: Nanotechnology, Biology, and Medicine, 2011. **7**(6): p. 694-701.

89. Wang, W., *Caractérisation géométrique et mécanique multi-échelle de la dentine humaine.* 2016, Paris Saclay.

90. Bertassoni, L.E., et al., *Biomechanical perspective on the remineralization of dentin.* Caries Research, 2009. **43**(1): p. 70-77.

91. Deshpande, V.S. and N.A. Fleck, *Isotropic constitutive models for metallic foams.* Journal of the Mechanics and Physics of Solids, 2000. **48**(6): p. 1253-1283.

92. Gheorghiu, S. and M.O. Coppens, *Optimal bimodal pore networks for heterogeneous catalysis.* AIChE journal, 2004. **50**(4): p. 812-820.

93. Lührs, L., et al., *Elastic and plastic Poisson's ratios of nanoporous gold.* Scripta Materialia, 2016. **110**: p. 65-69.

94. Hashin, Z., *The Elastic Moduli of Heterogeneous Materials.* Journal of Applied Mechanics, 1962. **29**(1): p. 143-150.

95. Arson, C., et al., *An alternative to periodic homogenization for dentin elastic stiffness.* Journal of Mechanics in Medicine and Biology, 2020. **20**(02): p. 1950081.

96. Snyder, J. and J. Erlebacher. *The active surface area of nanoporous metals during oxygen reduction.* 2011.

97. Zhang, Z., et al., *Nanoporous Gold Ribbons with Bimodal Channel Size Distributions by Chemical Dealloying of Al−Au Alloys.* The Journal of Physical Chemistry C, 2009. **113**(4): p. 1308-1314.

98. Ding, Y. and J. Erlebacher, *Nanoporous metals with controlled multimodal pore size distribution.* Journal of the American Chemical Society, 2003. **125**(26): p. 7772-7773.

99. Hakamada, M. and M. Mabuchi, *Fabrication of nanoporous palladium by dealloying and its thermal coarsening.* Journal of Alloys and Compounds, 2009. **479**(1): p. 326-329.

100. Wang, N., Y. Pan, and S. Wu, *Relationship between dealloying conditions and coarsening behaviors of nanoporous copper fabricated by dealloying Cu-Ce metallic glasses.* Journal of Materials Science & Technology, 2018. **34**(7): p. 1162-1171.

101. Erlebacher, J., *An atomistic description of dealloying porosity evolution, the critical potential, and rate-limiting behavior.* Journal of the Electrochemical Society, 2004. **151**(10): p. C614-C626.

102. Xu, C., et al., *Low temperature CO oxidation over unsupported nanoporous gold.* Journal of the American Chemical Society, 2007. **129**(1): p. 42-43.

103. Torquato, S., *Statistical description of microstructures.* Annual review of materials research, 2002. **32**(1): p. 77-111.

104. Sobiecki, A., A. Jalba, and A. Telea, *Comparison of curve and surface skeletonization methods for voxel shapes.* Pattern Recognition Letters, 2014. **47**: p. 147-156.

105. Haralick, R.M. and L.G. Shapiro, *Computer and robot vision.* Vol. 1. 1992: Addison-wesley Reading.

106. Gupta, R. and R. Kaur, *Skeletonization algorithm for numerical patterns.* International Jornal of Signal Processing, Image Processing and Pattern Recognition, 2008. **1**: p. 63-72.

107. Falcucci, G., et al., *Mapping reactive flow patterns in monolithic nanoporous catalysts.* Microfluidics and Nanofluidics, 2016. **20**(7): p. 105.

108. Erlebacher, J. and I. McCue, *Geometric characterization of nanoporous metals.* Acta materialia, 2012. **60**(17): p. 6164-6174.